HIGH TEMPERATURE COMPOSITE MATERIALS AND MAGNETODIELECTRIC COMPOSITES FOR MICROWAVE APPLICATION

by

Thanh Ba Do

A dissertation submitted in partial fulfillment
of the requirement for the degree of
Doctor of Philosophy
(Materials Science and Engineering)
In the University of Michigan
2010

Doctoral committee:

Professor John W. Halloran, Chair
Professor Richard W. Robertson
Professor Margaret S.Wooldridge
Assistant Professor Anton Van der Ven

"Science, my lad, is made up of mistakes, but they are mistakes which it is useful to make, because they lead little by little to the truth"- *Jules Verne*

To my parents, my brothers and sisters

To Do Ba Quoc Anh, my son

Acknowledgements

First of all, I must express my deepest gratitude to my advisor, Prof. John W. Halloran for the opportunity to work for him. His charismatic advice, support and encouragement fueled this journey. Everything is not easy to me and he has always provided me a belief that mistakes will lead me to the truth and he has always given me a second chance. It was my honor to work in his lab.

Thank you to my committee members - Professor Richard Robertson, Professor Margaret Wooldridge, and Professor Anton Van der Ven for their service.

Friendship, help and share with Zach N. Wing, Sigrun N. Karlsdottir, Chang Jun Bae, Claudia Torres, Vladka Tomeckova, Sindhura Gangireddy, and Susan Gentry are valuable part of my support.

Table of Contents

List of Figures

Part I: The properties and Oxidation Behavior of Boron Nitride

Part II: Dielectromagnetic Composites for Microwave Applications

List of Tables

Part I: Properties and Oxidation Behavior of Boron Nitride

Part II: Magnetodielectric Composites for Microwave Applications

Part I

Properties and Oxidation Behavior of Boron Nitride

Chapter 1

Introduction

Boron nitride (BN) has been well known as having several crystal morphologies.[1-2] The morphologies Wurzite and Zinc Blende have cubic crystal structure and are hard materials with bulk modulus up to 400 GPa. However, in this research, we are interested in its hexagonal morphology because this material has been discovered to have unique properties which are promising for many applications. With the alternative arrangement of boron and nitrogen atoms in its crystal structure, hexagonal BN has a layered structure alike to that of graphite as shown in Fig. 1.1 [1, 3], causing it to have many properties similar to graphite. They all have a high thermal conductivity and a low thermal expansion. It has low strength bonding between BN layers like graphite so that it has been used as a lubricant for many applications, especially at high temperature. While carbon only works for applications

at temperatures lower than $400^{o}C$, BN can be used at temperature up to $900^{o}C$ in oxidizing atmosphere [4-6].

General Electric Corp. (GE) [3, 5-6] produces pyrolytic BN in the form of crucibles, tubes or bottles in which BN leaflets are perfectly aligned with each other and stay at a maximum density. These products are promising for high temperature applications such as working with graphite at $2200^{o}C$, molten metals and alloys, or single crystal growth of compound semiconductors [6].

Hexagonal BN (h-BN) has a low bonding strength of layer structure, together with its low thermal expansion coefficient; it has been used widely as a coating material for many fiber composites. The replacement of BN instead of using graphite [4, 7-8] as the coating layers for SiC [4, 9-10] and Si_3N_4 [11-16] increased the strength of fibrous monolithic composite from 350MPa to 500MPa, and the work of fracture increased by a factor of two [7], from 4000 J/m^2 to 8000 J/m^2. BN platelets align parallel with the longitudinal axis of fibers and helped to change the catastrophic failure mechanism of brittle cell ceramic fibers into ductile failure mechanism in which crack pathways are bifurcated. The maximum value of fracture strength is decreased, but the total work of fracture is increased due to this crack delamination.

BN significantly improves the mechanical properties of fibrous monolithic composites. However, its application is limited due to its easy oxidation in oxidizing working environments to form nitrogen gas and boron oxide, a volatile liquid compound at high temperature. Research of N. Jacobson et al. [16-17] expressed that the oxidation of BN is dependent upon its crystallographic orientation, porosity and

impurity levels. The oxidation rate along the BN edge is more aggressive than that along its basal surface. Practically, BN has usually been used with several sintering aids to facilitate the manufacturing process as well as to improve the mechanical strength of materials [6, 12-16, 18]. The oxidation behavior of BN in the presence of these sintering additives has not been discussed elsewhere.

Therefore, the purpose of this study is to investigate the mechanical properties of BN with the addition of sintering aids Al_2O_3, Y_2O_3 and SiO_2, the oxidation behaviors and oxidation resistance of BN in the presence of these oxides. The preliminary research of R.W. Trice and J.W. Halloran [19] indicated that a highly aligned structure of BN produced better compactness and higher flexural strength than that of its poorly aligned structure. In our research, the extrusion technique will be applied to obtain this highly ordered arrangement of BN platelets. The hot-press technique will be used to sinter and provide the compactness of the ceramics system. The four-point bending test will be applied to measure the flexural strength and elastic modulus. The oxidation test will be conducted at $1200^{o}C$ in flowing dry air.

boron (III) nitride

2.47A°

6.66

2.47A°

6.70A

BN

Graphite

(a)

(b)
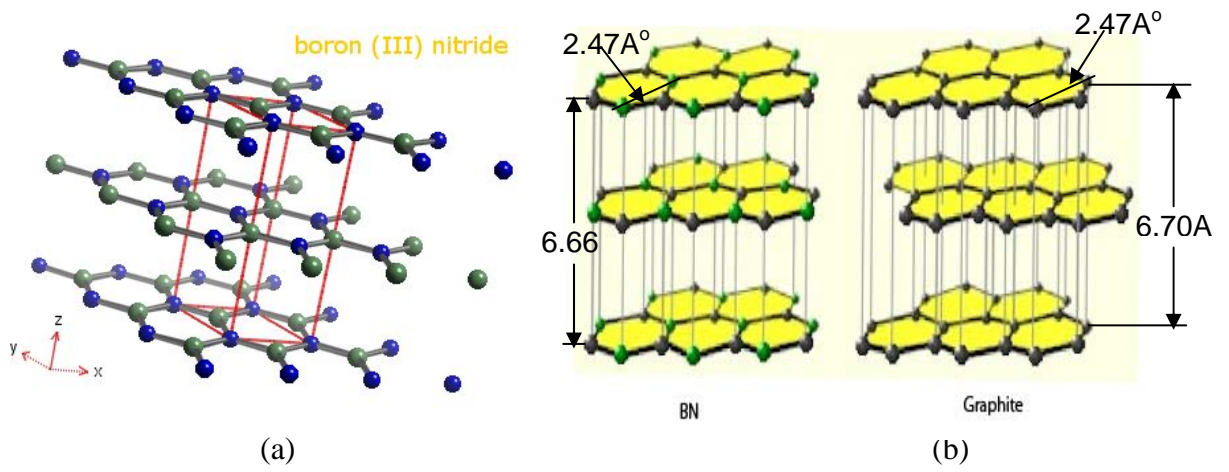
Fig. 1.1: The arrangement of B and N atoms in BN crystal structure (a) and the similarity of BN and graphite structure (b) [1, 3].

References

1.   http://www.webelements.com/boron/boron_nitride.html.   [cited 2005 Nov. 12]; Available.
2.   http://www.ioffe.rssi.ru/sva/nsm/semicond/BN/basic.html.   [cited 2005 Nov.12]; Available.
3.   http://www.alustop.com/cms/index.php.   [cited 2006 Jan. 07]; Available.
4.   S. Baskaran, J.W.Halloran, *Fibrous Monolithic Ceramics: III, Mechanical Properties and Oxidation Behavior of the Silicon Carbide/Boron Nitride System.* Journal of American Ceramics Society, 1994. **77**(5): p. 1249-1255.
5.   http://www.advceramics.com/geac/products/bn_powder/powder_ac6003.html. [cited 2006 May 10]; Available.
6.   http://www.advceramics.com/geac/products/pyrolytic_bn/.   [cited 2006 May 10]; Available.
7.   R.W.Trice, *PhD Thesis*, in *Materials Science and Engineering*. 1998, University of Michigan: Ann Arbor. p. 215.
8.   S.Li, Y.Huang, Y.M.Luo, C.Wang, C.Li, Materials Letters, 2003. **57**: p. 1670-1674.
9.   E.Y.Sun, S.R.Nutt, J.J.Brennan, Journal of American Ceramics Society, 1997. **80**(1): p. 261-266.
10.   L.U.J.T. Ogbuji, D.R.Wheeler, T.R.McCue. 2001, NASA.
11.   S.Y.Lienard, D.Kovar, R.J.Moon, K.J.Owman, J.W.Halloran, Journal of Materials Science, 2000. **35**: p. 3365-3371.
12.   D.Kovar, M.D.Thouless, J.W.Halloran, Journal of American Ceramics Society, 1998. **81**(4): p. 1004-1012.
13.   R.W.Trice, J.W.Halloran, Journal of American Ceramics Society, 1999. **82**(9): p. 2502-2508.
14.   R.W.Trice, J.W.Halloran, Journal of American Ceramics Society, 1999. **82**(11): p. 2943-2947.
15.   D.Kovar, B.King, R.W.Trice, J.W.Halloran, Journal of American Ceramics Society, 1997. **80**(10): p. 2471-2487.
16.   N.Jacobson, S.Farmer, A.Moore, H.Sayir, Journal of American Ceramics Society, 1999. **82**(2): p. 393-398.
17.   N.Jacobson, G.N.Morscher, D.R.Bryant, R.E.Tressler, Journal of American Ceramics Society, 1999. **82**(6): p. 1473-1478.
18.   K.E.Drina, *PhD Thesis*, in *Materials Science and Engineering*. 1997, University of Michigan Ann Arbor.
19.   R.W.Trice, J.W.Halloran, Journal of American Ceramics Society, 1999. **82**(6): p. 2563-2565.

Chapter 2

Experimental Procedures

This chapter details the experimental procedures used to prepare and characterize samples after sintering and oxidation test. It is organized into three main sections. The first section describes the preparation techniques used to produce highly aligned BN billets with the addition of additives. The second section describes the mechanical testing used to characterize these fabricated specimens at 25°C. The final section provides details of the oxidation procedures and the techniques to prepare samples for phase and microstructural analysis.

2.1. Samples processing

2.1.1. Raw materials

The materials used to produce sample billets were hexagonal boron nitride (h-BN) powder (AC 6003) with purity >95% from GE advanced ceramics group, Al_2O_3 (Alfa Aesar, 99.99% pure), Y_2O_3 (99.9% pure, Reaction, Johnson Matthey, Ceramics, Downingtown, PA), amorphous SiO_2 from Degussa Corp/Pigment group. Fig. 2.1 is a

microstructural view of BN powder from GE Corp. [1], showing the crystal size is around 0.5 μm and thickness is between 0.07 and 0.1 μm. BN contains 2 wt% of oxygen and 0.2 wt% of soluble borate and 0.2 wt% of moisture as delivered from the company. The surface area of BN powder was 29 m^2/g. Three different compositions of BN were prepared, with their details given in Table 2.1. All these components were added to a polypropylene jar and mixed for 24 hrs using Si_3N_4 media in ethanol. To help mixing and dispersing these ingredients evenly into each other, a dispersant agent (Span 85, ICI Americas, Wilmington, DE) was used with 2 wt% [2-4]. After milling, the mixtures were dried in an oven at 70°C.

Two polymers PolyEthylene-Ethyl Acrylate 20 (EEA 20) and EEA 1.5 obtained from Advanced Ceramics Reseach (ACR) from Tucson, Arizona, were used as the resin for extruding the ceramic powders. After extrusioin, BN flakes were arranged in a highly aligned order. Heavy Mineral Oil (HMO) and Poly Ethylene Glycol 1000 (PEG-1000) were added into the system during hot mixing as dispersant agents [5].

2.1.2. BN ribbon extrusion

The hot mixing process was conducted in a high shear mixer (Plasti-Corder PL2100 from C.W.Brabender) at 115°C which is hot enough for EEA to melt. The ceramic powder and polymers ratio is 50:50 by volume. The procedure of this preparation step was described elsewhere [5-6] in which ceramics powders were gradually added into a melted mixture of polymers. The dispersant agents were added alternatively to

ceramics powder to ensure the even distribution of the powders mixture. The torque value of the mixture was around 3000 Pa^{-1} at the end of the mixing process.

Pieces of ceramics-polymers were taken out of the mixing machine and pressed with each other in a prism die using a Bradford pressing machine at a temperature of 130°C and a pressure up to 1 MPa. These prisms were used for the extrusion of ribbons 26mm wide and 1mm thick. The extrusion was carried out using the same pressing machine. The pressure was 0.5 MPa. By this process of extrusion, the BN flakes were aligned as they flowed out of the extrusion die through a small slot. Nine small pieces of 26×52 mm that were fit with hot pressing mold were cut and stacked on each other into a metal die. They were all pressed under a pressure of 12 MPa after heated up to 130°C and retained for 15 minutes at this loading. The heating softened thermoplastic polymers, allowing stacked pieces of BN-polymer to attach with each other under the load. A physical bond was formed between the sample's layers to keep them in one block. After being taken out and shaped up, these blocks were ready for the binder burn out step.

2.1.3. Binder burn out (BBO)

The purpose of this step was to remove the polymers and organic compounds from ceramic powders by decomposing and expelling them with the aid of a carrying gas at high temperature [5-7]. This step consisted of binder burn out and post-binder burn out sub-steps whose gas medium and heating schedules were different. In the first sub-step, nitrogen gas was used for the organic compound decomposition reactions at

temperature up to 600°C. These reactions did not occur aggressively in the flowing nitrogen atmosphere. The pellets still retained their shapes after this burning stage. Since polymers and dispersant agents are compounds of C, H and O, the decomposed products were water vapor and volatile low molecular weight organic fragments, and solid carbon residue. This BBO process took 3 days. The subsequent post-binder burn out stage was aimed to remove all remaining carbon from the decomposition of polymers and organic compound. From the calculation of weight change before and after BBO, this carbon amount was from 0.8 to 1.3 wt% [5, 7]. The medium for this stage was the dry flowing air. The heating schedules for these two stages are given in Table 2.1 and 2.2. While the low molecular weight organic fragments and water were released by their evaporation, carbon was retained inside the sample as small black particles. They are only burnt off in the air flow in the post-burnt out stage. In this stage, carbon was released from the sample by the oxidation reaction to produce carbon dioxide gas at temperature of 400°C.

The ceramic powders after this step were free from the organic compounds. The evaporation of organic compounds and polymers changes the height of sample's pellets with poorer attachment between stacks. They must be handled very gently when placed into the hot pressing mold.

2.1.4. Hot pressing

Samples were gently placed into the graphite mold for hot pressing. All graphite parts that contacted the sample were coated with a thin layer of rough particle size h-BN

that was also obtained from the GE Advanced Ceramics group. The hot pressings were conducted in a 50 ton hot press furnace HP50-7010G from Thermal Technology Corp. The sintering was held at a temperature of $1740^{o}C$ and at a pressure of 25 MPa. However, the load was only applied when the temperature was over $1200^{o}C$, as measured at the surface of mold by a pyrometer. The temperature $1740^{o}C$ was held for 2 hours before being cooled down. Samples were released from the mold when the temperature was quenched to below $100^{o}C$. The sintered specimens had dimensions of 26 mm in width, 52 mm in length and 5mm in height. They were subjected to grinding and polishing before mechanical and oxidation tests.

2.2. Preparation of samples for mechanical testing

2.2.1. Grinding and polishing

The samples needed to be machined on all their faces until they meet the fineness requirement for the mechanical and oxidation tests. First, they were evenly ground on the two hot pressing surfaces to remove the embedded supported boron nitride from the hot pressing by using 240 grits SiC paper. The depth of sample removed was 0.5 mm on both sides. The further outer layers removal was carried out with the use of 600 grit SiC paper. The depth of sample removed was 0.3 mm on two sides. The refinement stage after rough grinding was on 800 grit and 1200 grit SiC papers. Other edge surfaces of samples were all processed in the same order of grinding but with different amounts of sample being removed. By the end of this step, the samples were

20 mm wide, 48 mm long and 3.2 mm height. The grinding was conducted on Buehler grinder/polisher Automet 3.

For mechanical test, the samples were cut into small pieces with length 48 mm, height 3 mm and width 4 mm. The large hot pressed samples were cut by Buehler wheel cutter into designed pieces and re-machined until they met fineness requirement. Since BN is a soft material with its graphite structure, the bonding strength between BN flakes was very weak and a roughness of 6 μm finish was the finest level we could attain.

2.2.2. Relative density and porosity measurement

The relative density and porosity of samples after hot pressing were measured using Archimedes' principle [8], in which weights of samples in dry state, water soaked state and immersed in water were measured. The relative density of samples was calculated according to the equation:

$$d = 1 - \rho_{H_2O} \cdot \frac{W_1 - W_2}{W_1 - W_3},$$
(Eq. 2.1)

where W1 is sample's weight of soaked state in air, W2 is the sample's weight at dry state and W3 is sample's weight in water.

The porosity of sample was calculated by the use of equation:

$$\text{Porosity} = \frac{W_1 - W_2}{W_1 - W_3}$$
(Eq. 2.2)

11

2.2.3. Flexural strength measurement

Four-point flexural testing was performed on BN samples with the set-up is schematically indicated in Fig. 2.2. The outer and inner spans were fixed at 40 mm and 20 mm, respectively. Three samples were tested to obtain average values as well as error bars. With this design, the results were not affected by shear stress which happens in three-point bending. All the tests were conducted at a rate of 0.5 mm/min. The experiments were performed on a screw-driven load frame (Instron 4483, Instron Corp.) equipped with a 5 kN load cell. The load frame was driven by the computer through an IEEE interface.

2.2.4. Elastic modulus

It is typical that the elastic modulus of materials will be determined by acoustic resonance method [5-6]. However, since BN is a weak material, the application of this technique would not be successful due to the excessive damping of BN. The elastic modulus of BN was extrapolated from the measurement of its flexure strength.

2.3. Oxidation test and characterizations

The oxidation tests were conducted at a temperature of $1200^{o}C$ in flowing dried air. This dried air was supplied by the Detroit Cryogen Gas Company that contained 10^{-5} torr water vapor at the atmospheric pressure 750 torr. The resistance of BN to oxidation was investigated through its weight loss and its appearance after exposure

at this severe condition for a variety of time from 0.5 hr to 30 hrs. Preliminary results indicated that the application of a conventional testing furnace was not appropriate and that a new apparatus for this purpose need to be invented. Samples after oxidation tests were maintained and processed in such a way that eliminated their exposure to humidity in air. Microscopic changes and the formation of new features on sample surfaces were studied by the optical and backscattered electron microscope. X-ray Diffraction was used to detect phases and Electron Probe Microanalysis (EPMA) was used to quantitatively measure their compositions.

2.3.1. Oxidation procedures and new oxidation testing equipment

Specimens used for this test were prepared similar to those for mechanical tests. They were all ground and polished until there were no scratches on their surfaces. The oxidation test is usually performed in a conventional tube furnace that is illustrated in Fig. 2.3. A flux of oxidizing gas is allowed to flow inside the reaction tube where samples are held. The samples are placed in the hottest region of the reaction tube.

This design has the advantages that samples are easy to handle and multiple samples can be tested at the same time. However, this instrument has a significant disadvantage for BN oxidation test because the samples are always exposed to moist air. Since boron oxide is very sensitive to humidity [9-10], artifacts can be produced with various appearances. The features produced after the oxidation changed with time, so it would be unreliable to determine the real behavior of oxidized samples. The SEM image in Fig. 2.4 shows flakes of boric acid generated from this hydration

reaction on a glass scale on the surface of a BNYS2 sample after 30 hours of oxidation.

The new oxidation experiment apparatus is depicted in Fig. 2.5. It has a silica glass reaction tube connected to glass-tight sample's container. We designed this apparatus in the tied structure so that the atmosphere inside the reaction tube can be easily controlled. The samples are placed on a sample holder attached on a glass rod which is hanged in the center of the reaction tube. Apart from these advantages, the reaction tube is very easily inserted into and to withdraw from the hot region which is valuable to experiments requiring sudden heat supply. In our research, BN was delivered into the hot zone by using the glass rod and removed from there to the cold end of the reaction tube. Oxidized samples were stored inside the glass-tight sample's container and being isolated from the humidity in the air.

2.3.2. Optical microscope procedures

The purpose of this procedure was to observe the appearance of features on the surface of BN samples after oxidation. As will be detailed in the result and discussion section, the oxidation generated glass droplets and a glass layer on the surface of the boron nitride samples. Optical microscopy was very effective to show the appearance of these glass droplets as well as to measure their diameters. The measurements were conducted with the aid of a Nikon optical microscope. The images were taken at 1, 1.5, 3, and 6.3 magnifications.

2.3.3. Scanning Electron Microscope (SEM) and Electron Microprobe MicroAnalysis (EPMA) procedures

The SEM analysis was aimed to detecting the features on the sample surface and their quantitative elemental compositions. This technique has the advantage of not requiring a very complicated sample preparation. The quantitative analysis can be done on a surface that is not very flat. However, this method does not produce very accurate results and is not a reliable method to detect boron. The EPMA technique can make up for the disadvantages of SEM since the accuracy is up to 99%. Boron is in the range of detectable elements with the deflection of about 2%.

Samples were processed by a typical manner as for SEM analysis. The only thing that we needed to take care of was trying to preserve samples in a moisture free environment as best as we can. For this reason, they were handled inside a glove box using extra-dry nitrogen gas as the working medium. When still inside the container, samples were put into the glove box, processed and seized inside dry vials again until analysis. However, we could not avoid exposing samples to the air when coating them or putting into the SEM machine. With this great care of not exposing samples into the moist air, we eliminated a major part of hydration reaction of oxidation products.

 The preparation of samples for EPMA was slightly more challenging. The technique required the measured surface to be flat and very fine polished. For this reason, samples needed to be mounted into epoxies and in turn, the epoxies and samples were ground and polished. As mentioned above, since the oxidation product is sensitive to

water, the conventional media like isopropanol or ethylene glycol were not appropriate because these agents absorb water from the air which may affect the oxidation product from its hydration reaction. Light mineral oil from Alfa Aesar (d=0.827 g/cm^3, viscosity= 29 Pa^{-1}) was used for this purpose. With the nature of low molecular weight saturated hydro carbon, its hydrophobia prevents the dissolution of water and is good for protecting oxidation features of BN. However, cleaning the mineral oil chemical from sample surfaces after polishing was an annoyance with similar problem of using isopropanol and drying it. A preliminary experiment to dry samples by heating showed the evidence of hydration of generated borate during this heating stage. Using vacuum to dry samples after quickly soaking them in a beaker containing isopropanol was better. However, hydration was still unavoidable during processing time and conductive layer coating procedure.
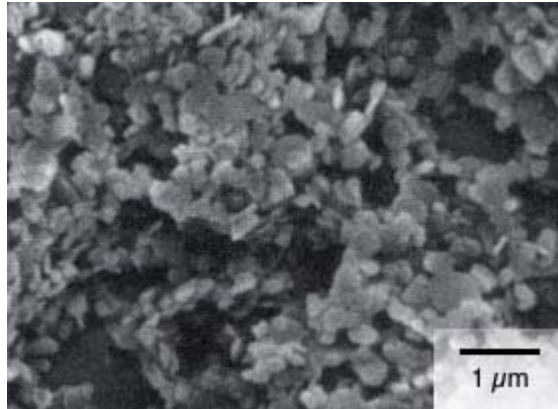
Fig. 2.1: Microstructure of h-BN powder used for the experiment. The crystal size is

~0.5μm.[1]

Table 2.1: The compositions of ceramics powder mixtures

	BN (wt%)	Al_2O_3 (wt%)	Y_2O_3 (wt%)	SiO_2 (wt%)
BNY	92	2	6	0
BNYS2	90	2	6	2
BNYS6	86	2	6	6

Table 2.2: Heating scheme for binder burnt out stage. The environment was nitrogen

gas

Steps	Heating rate (^{o}C/hr)	Target temperature (^{o}C)	Dwelling time (hrs)
1	30	300	6
2	10	350	6
3	10	400	6
4	30	600	2
5	20	25	-

Table 2.3: Heating scheme for post-binder burnt out stage in the flowing dry air atmosphere

Steps	Heating rate ($^{\circ}$C/hr)	Target temperature ($^{\circ}$C)	Dwelling time (hrs)
1	60	400	24
2	60	25	-
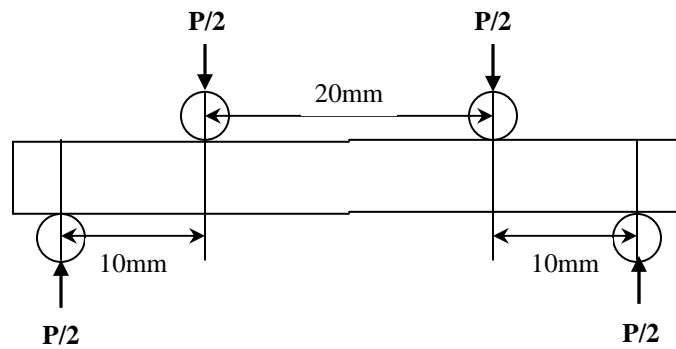
Fig. 2.2: Schematic illustration of four-point flexural test
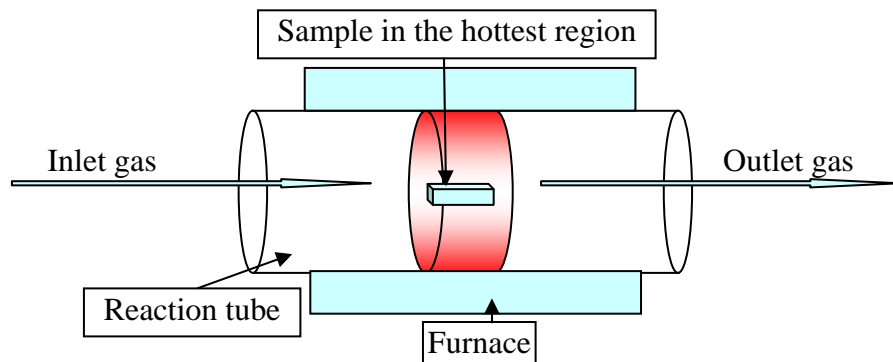
Fig. 2.3: The schematic of conventional oxidation furnace
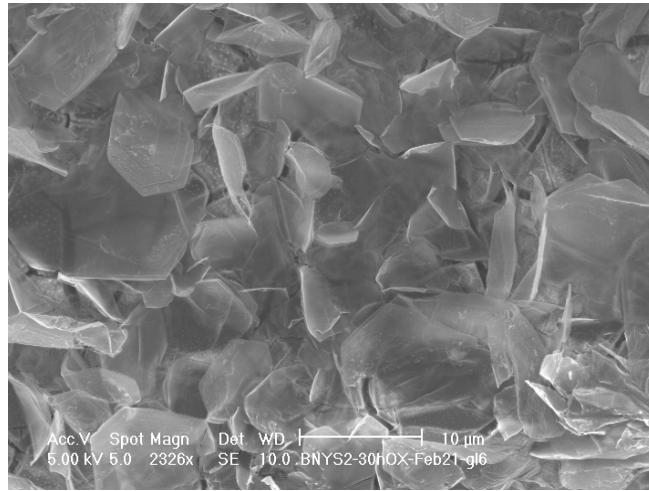
Fig. 2.4: Artifacts generated on the glass scale on BNYS2 sample's surface
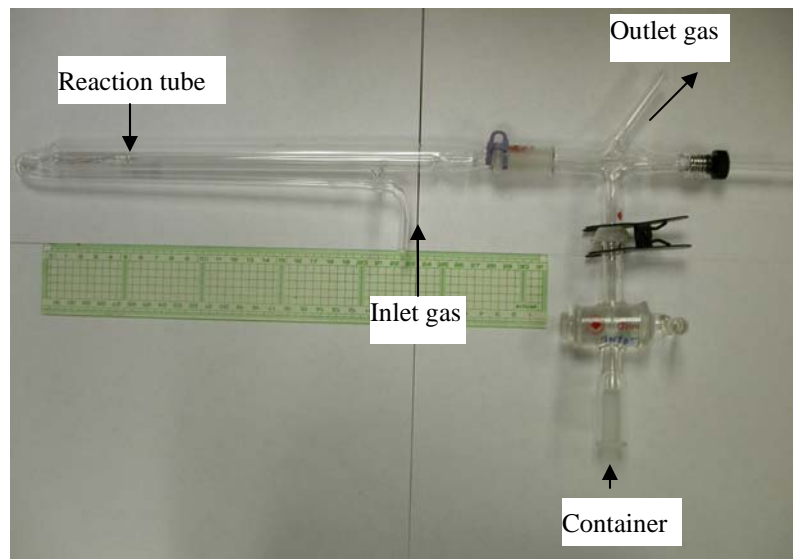
Fig. 2.5: New oxidation test apparatus

References

1. http://www.advceramics.com/geac/products/bn_powder/powder_ac6003.html. [cited 2006 May 10]; Available.
2. P. Dragan, J.W. Halloran, G.E. Hillmas, G.A. Brady, S. Somers, A. Barda, and G.Zywicki, *Process of Preparing Textured Ceramic Composites*, in *Engineering*, U. Patent, Editor. 1997, J.W. Halloran: USA. p. 54.
3. S.Baskaran, S.D.Nunn, D.Popovich, J.W. Halloran, *Fibrous Monolithic Ceramics: II, Fabrication, Microstructure, and Indentation Behavior.* Journal of American Ceramic Society, 1995. **76**(9): p. 2209-2216.
4. Z.N.Wing, *Fabrication and Characterizatioin of Efective Medium Meta-dielectrics*, in *Materials Science and Engineering*. 2005, University of Michigan: Ann Arbor. p. 200.
5. R.W.Trice, *PhD Thesis*, in *Materials Science and Engineering*. 1998, University of Michigan: Ann Arbor. p. 215.
6. R.W.Trice, J.W.Halloran, *Influence of Microstructure and Temperature on the Interfacial Energy of Silicon Nitride/Boron Nitride Fibrous Monolithic Ceramics.* Journal of American Ceramics Society, 1999. **82**(9): p. 2502-2508.
7. kK.E.Hrdina, *Phenomena During Thermal Removal of Binders*, in *Materials Science and Engineering*. 1997, University of Michigan: Ann Arbor. p. 188.
8. D.R.Dinger, *Particle Calculation for Ceramics*, D.R.Dinger, Editor. 2001, Morris Publishing. p. 11, 23-29.
9. N.Jacobson, G.N.Morscher, D.R.Bryant, R.E.Tressler, *High-Temperature Oxidation of Boron Nitride: II, Boron Nitride Layers in Composites.* Journal of American Ceramics Society, 1999. **82**(6): p. 1473-1478.
10. N.Jacobson, S.Farmer, A.Moore, H.Sayir, *High-Temperature Oxidation of Boron Nitride: I, Monolithic Boron Nitride.* Journal of American Ceramics Society, 1999. **82**(2): p. 393-398.

Chapter 3

Results and Discussions

3.1. Microstructures of BN after hot pressing

In this section, we will discuss the alignment of BN platelets, the distribution of oxide phases, and the formation of phases after hot pressing. The appearance of microstructure was investigated by SEM and Backscattered Electron Microscope (BSE). The phase formed after sintering was detected by X-ray Diffraction (XRD) machine from Rigaku Corp, Japan, using Cu cathode, $\lambda = 1.5405 A^o$, scanning speed was 3°/min, scanning step was 0.03^o. The range of diffraction was from 10° to 90° 2θ. The microscope investigations showed a grain growth of BN from the reaction of oxides with residual boron oxide (B_2O_3) in BN. The XRD measurement demonstrated the domination of BN phase.

The most interesting influence of sintering aids on the microstructure of BN is their influences on grain growth of BN and on BN alignment. Images of this phenomenon are given in Fig. 3.1 for BNY ($92BN:2Al_2O_3:6Y_2O_3$) and in Fig. 3.2 for BNYS2 ($90BN:2Al_2O_3:6Y_2O_3:2SiO_2$) and BNYS6 ($84BN:2Al_2O_3:6Y_2O_3:6SiO_2$) samples. The grain growth was more apparent in the BNY samples than observed in BNYS2 and BNYS6 samples. The dark gray regions in Fig. 3.1 (a) are BN and the bright

surrounding areas are oxide phases. BSE pictures in Fig. 3.2 (b) proved this suggestion. Oxides that consist of heavy elements are more reflective under the electron beam than BN consisting light elements.

S.L.Hwang et al. [1], C. Wang et al. [2], L.S. Sigl et al. [3] reported the grain growth of Si_3N_4 and SiC when they added up to 10 wt% mixture of $Al_2O_3+Y_2O_3$. B. Ertug et al. [4] also discussed the grain growth of BN in their research using B_2O_3 as the sintering additive. According to Hwang, Wang and Sigl, the mechanism for this phenomenon is the dissolution and reprecipitation of Si_3N_4 and SiC on undissolved particles. Our microscopic observations indicated that the mechanism of grain growth in our research is not the same as in the research of B. Ertug and colleagues. BN is very poorly dissolved into liquid borate at high temperatures, though its solubility is increased [5-6] in the presence of other oxides like Al_2O_3, Y_2O_3 or SiO_2. Therefore, even if we used 8 wt% of $Al_2O_3+Y_2O_3$, the white border of BN particles would contain only the reaction product of these two oxides with borate. It appeared as a liquid phase at high temperature and pressure sintering condition. This reaction product acts as a bonding agent to connect BN plates with each other, making them increase in size. The coalescence of BN particles results in the appearance of triple points amongst BN particles as observed in Fig. 3.1 (a). Similar to results reported by B.Ertug et al. [4, 7] and M. Hubaecek et al.[8], this glass formation in BNYS2 and BNYS6 increased the density of BN. The addition of 8 wt% of oxides in the BNY samples would not generate enough liquid to bond BN particles, producing a highly dense structure of BN as seen in Fig. 3.1 (a).

The grain growth phenomenon in BNYS2 and BNYS6 samples were not obviously observed since the oxides and BN phases seemed to mix with each other better. BSE images of these two compositions are given in Fig. 3.2 (a) and (b), respectively, showing that the further supplementation of SiO_2 helped to distribute the oxides more uniformly through the BN samples or, in other words, SiO_2 improved the reaction between sintering aids with residual B_2O_3 on BN plates.

If considering BN arranged as clusters and every cluster is separated from others by a white border of oxides, then we can see various clusters with different size as in Fig. 3.2. Crystals of BN particles are not obviously observed in these two images. They linked with each other with the assistance of a melted oxide phase to form a continuous net of BN particles. Some of them were surrounded by a glass pocket as spot (1) in Fig. 3.2 a, b and most of them have a rounded morphology. The dissolution of BN into oxides was more obvious in these two circumstances than that of BNY. Diameter and thickness of grown BN crystals in BNY sample and clusters in BNYS2 and BNYS6 samples were measured and compared with those obtained from bare BN crystals. These data are shown in Table 3.1.

In comparison with the original crystal size of h-BN, the addition of Al_2O_3 and Y_2O_3 increased the crystal size of BN to be 25 to 35 times larger than that of the starting powder while the further addition of SiO_2 increased this value only 3 to 7 times. The thickness of BN grains were looked the same with BN grains of the original powder. The addition of SiO_2 has less effect on the growth of BN flakes that resulted in the formation of a continuous net of better aligned BN flakes. These results were consistent with the relative density values that are also given in Table 3.1. This high

23

density of BN particles resulted in almost complete density in BNYS2 and BNYS6 samples. Meanwhile, due to the excessive grain growth that limited bonding between BN particles, BNY samples turned into a highly porous structure even after being processed under the high temperature and pressure of hot sintering.

The polarized microscope image of BNY (2Al:6Y) sample given in Fig. 3.3 depicts the presence of long features randomly arranged with each other in the form of spherulite clusters. XRD measurement did not show an obvious appearance of any new phase in the BNY samples after the hot pressing stage. Electron Diffraction Spectroscopy analysis with spot's diameters of 200×200 μm and 5×5 μm did not show any abnormal high concentration of oxides, the evidence of the formation of new phases in and at the neighborhood of these spherulite features. Referred to Fig. 3.1a, these features would be assumed as the consequence of the growth of BN platelets in which BN platelets' edges aligned to form higher porosity areas. This assumption is more evidenced from the observation of the back scattered electron microscopy image of this sample in Fig. 3.1b. In this figure, there is an area that looks like a spherulite cluster formed from a higher porosity. These spherical clusters were not found in BNYS2 and BNYS6 samples those had higher density and lower porosity than that of BNY samples as given in Table 3.1. Nevertheless, a better understand of this phenomenon requires a further investigation.

The misalignment of BN platelets implied that the addition of only Al_2O_3 and Y_2O_3 were not effective enough to produce a highly aligned structure at a microscopic level. These features are not found in the BNYS2 and BNYS6 surfaces. However, SEM pictures of the cross sections of these two specimens in Fig. 3.4 (a) and (b),

respectively, show a misalignment in BNYS2 sample by some degree. This cluster of misaligned BN grains was not apparent in BNYS6 sample as seen in Fig. 3.4 (b).

The relationship between BN grain's diameter and thickness and its oxide contents is depicted in Fig. 3.5. While the diameter of BN in the BNY sample is much larger than that of the bare h-BN sample, the diameter of BN in BNYS2 and BNYS6 is several times larger. The presence of SiO_2 had a strong effect to suppress this phenomenon. While the use of Al_2O_3 and Y_2O_3 increased BN grain size, the further addition of SiO_2 increased BN thickness. This may be a consequence of the different amounts of liquid formed from the sintering process.

In summary, we applied SEM, optical microscopy and XRD methods to investigate the influence of additive oxides on the microstructure of BN after the hot pressing process. Al_2O_3 and Y_2O_3 were responsible for the dramatically change of BN grain size, while the additional use of SiO_2 mitigated the grain growth of BN platelets. Amorphous silica reacted with B_2O_3 to form a glassy liquid medium to help evenly distribute sintering additives in the bulk of BN particles. As a result, SiO_2 improved the density of the hot-pressed BN samples by decreasing their porosity. The poor distribution of oxides phase in BN in BNY samples caused the stacking of BN flakes which formed misaligned BN clusters after hot pressing. XRD measurements indicated the presence of a predominant BN phase in these regions. Other phases that were possibly formed were still less than the detectable limit 0.5 vol% of the XRD equipment.

3.2. The mechanical properties of BN

Flexural strength and elastic modulus were two mechanical properties investigated in this research. They were obtained by a four-point bending test in which the loading was applied on the hot pressing surfaces of the samples. Results are given in Table 3.2.

A comparison is made in Table 3.3 with those reported by R.W. Trice and J.W. Halloran [9]. In their research, they applied a same ratio of 1.00 g of SiO_2: 1.34 g of Y_2O_3:0.18g of Al_2O_3 for two circumstances of high and low alignment of BN flakes. The sintering conditions were similar with hot pressing at 1740^oC for about 2 hrs under the pressure of 25 MPa. Results of samples containing 22 wt% of oxides and BNYS2 were comparable. The low alignment of BN platelets was compensated by the high amount of oxides which caused their flexural strength to be higher than those in our research.

The plots of these data in Fig. 3.6 (a) and (b) show the linear relationship between either flexural strength or elastic modulus and the relative density of BN. The higher the density of BN, the higher its flexural strength and modulus are. Though the trend lines in these two graphs indicate a linear relationship, they are not necessary to imply a true behavior of samples of this research. Results given by B. Ertug et al. [7] showed that BN with the addition of borate, hot-pressed at 1900^oC and pressure of 50 MPa for 1 hour, had a flexural strength of 140 MPa. The low mechanical properties of BNY samples can also be a consequence of aggressive grain growth and poor attachment between BN platelets.

Fig. 3.7 depicts the relationship between oxide content (diamond points) and silica content (square points) on the flexural strength (a) and elastic modulus (b) of BN. There was a big gap between the flexural strength of the sample does not contain SiO_2 (BNY) and of the sample contains 2 wt% SiO_2. Meanwhile, the discrepancy among results of samples containing SiO_2 was not extensive. This mechanical property's variation of BN was consistent with the variation of BN density or its porosity. It implies that the presence of SiO_2 is relevant because it improved the microstructure of BN which, in turn, strengthened the sintered BNs.

With all this evidence, the mechanical properties of BN were more related to the density of sintered BN specimens. However, additive oxides and SiO_2 are significant for these properties because they improved the microstructure of BN which, in turn, increased BN's strength and elastic modulus.

3.3. The oxidation behavior of BN with the addition of additives

In this part of the experiment, BN was oxidized at $1200^{o}C$ in a flowing dry air. Samples after oxidation were subjected to optical microscope analysis to investigate the appearance of features on the sample surfaces. SEM was used analyze the microscopy of these features and EPMA was used to quantitatively determine their elemental compositions.

3.3.1. The oxidation behavior of BNY

Fig. 3.8 (a) shows the appearance of light reflective dots on the BNY sample surface, implying that the BN oxidation reaction:

$$4BN + 3O_2 = 2B_2O_3 + 2N_2\uparrow \tag{1}$$
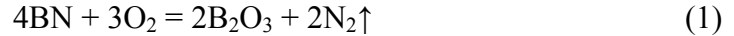
occured, resulting in the appearance of some features that could be products of this oxidation reaction. They looked round optically. The higher magnification observation by SEM showed those light reflective spots are glass droplets as seen in Fig. 3.8 (b).

These glass droplets are quenched liquid borate formed from BN's oxidation as seen in the reaction (1). The formed borate glass did not cover the sample surface but isolated and appeared in irregular shapes. At this very early oxidation stage, due to a very short dwelling time and fast cooling step, the produced borate did not have enough time to evaporate and stayed on the sample surface. The weight measurement of the sample after oxidation indicated a slight weight increase (Table 3.4 and Fig. 3.9). The formation of glass droplets was also reported by C.L. Yeh et al. [10] when they applied the Environmental Scanning Electron Microscope (ESEM) to study the oxidation behavior of BN at 1100^oC. Meanwhile, according to W.R. Witzke [11], liquid borate very poorly wets the boron nitride substrate. The lowest solid-liquid contacting angle he measured was 40° at temperatures as high as 1200^oC. This value increased very fast when the sample was cooled and became larger than 90° at temperatures below 600^oC. By this argument, the glass droplets in this case should appear as half spherical beads. However, as seen in Fig. 3.8 (b), the oxidation

exposed a rough bare BN surface that would prevent the movement of borate glass liquid. The appearance of these glass droplets became spherical when the oxidation time was lengthened as seen in Fig. 3.10a. They scattered all over the surface of the sample with varied diameters.

The diameters of glass drops increased along with the oxidation time. After two hours of oxidation, there were several glass droplets which looked exceptionally larger than the rest of them. The area surrounding these big glass droplets was occupied by tiny glass droplets. Similar behavior was also observed at longer oxidation times as shown in Fig. 3.10. There was a question raised as to how were these big glass droplets appeared. The absence of small glass droplets in the area around the big ones would suggest that they moved and were eaten up by big liquid glass particles. ESEM observation of C.L. Yeah et al. [10] confirmed the movement of borate when their sizes were big enough. SEM observation of BNY at 8 hours oxidation in Fig. 3.11 depicted the coalescent phenomenon of small neighboring glass particles to form a bigger one.

3.3.1.1. The growth of glass droplets and "Breath figure" patterns

We observed that the formation and growth of the glass droplet's diameter is analogue to those of water droplets during their condensation from vapor. Beysen and Knobler conducted a study on the growth mechanism of these water droplets and named it as the "Breath figure pattern" [12-14]. It is interesting to determine whether the reaction-formed liquid droplets would display the breath figure pattern.

According to Beysen and Knobler, when meeting a cold surface, water in a saturated vapor air deposits to form an array of randomly distributed water droplets. The evolution of these droplets can be divided into four stages in which the second and third stages are most significant [15-21]. The first stage is characterized by the formation of water nuclei on the flat surface. These water nuclei develop in size in the stage continuously until their particles cover ~75% of the surface area [15, 21-22]. The third stage occurs when two or more surrounding water droplets coalesce with each other to form a bigger water droplet which leaves vacant spaces around them.

This stage is represented by a sudden increase of drop's diameter in the graph. The formation of these tiny water droplets keeps average diameter value slowly but continuously increased as depicted in Fig. 3.12. New small droplets nucleate and develop on the induced vacant areas. With the continuously appearing small particles, the average size of a water drops would increase constantly [15, 21-22]. The expression of these two stages is given in the Fig.3.12. Data of the biggest and average diameters of glass beads along with the oxidation time is indicated in Table 3.5 and depicted in Fig. 3.13, correspondingly.

Fig. 3.13 (a) shows two sudden jumps at the oxidation times of 2 hours and 12 hours. They present the second stage in the Breath figure pattern, when small glass droplets met and merged with each other. The diameter of merged glass droplets at later oxidation times is larger than that of earlier oxidation times. The continuity of stage two and three results in the appearance of several jumping steps along with the oxidation time. In this circumstance, it was two jumping steps.

Fig. 3.13 (b) shows the evolution of average glass drop size. Data plotted with normal scale were scattered and linear with logarithmic scale which was consistent with the plot illustrated in the paper of Beysen and Knobler [12]. There would be a similarity of appearance between two models though their mechanisms were different from each other. Breath figure theory addresses continuous condensation of water. For our research, liquid B_2O_3 is continuously formed by the oxidation, but also evaporating. The appearance of borate droplets was the result of the dominance of the oxidation rate over the evaporation rate.

While C.L. Yeah et al. [10] heated pellets of BN and B_2O_3 at $1000^{\circ}C$ to observe the fluidity of liquid B_2O_3 on BN surface, our research indicated that liquid B_2O_3 was formed on the BN surface from its oxidation. Liquid B_2O_3 presented as a pattern of isolated droplets on BN as the consequence of the poor wet of liquid B_2O_3 on the BN surface and as the result of the competition between the formation of liquid B_2O_3 and its evaporation at high temperature. Though this mechanism was different from the condensation of water droplets on a flat surface from vapor, the borate glass droplet size evolution was similar to that of water droplets. Both of them can also be described by the Breadth figure pattern as we explained in previous paragraphs. This result would be relevant to explain not only the oxidation behavior of BN, but also the oxidation behavior of other boron-containing materials because the formed liquid B_2O_3 is not present as a layer but an array of scattered droplets [23].

3.3.1.2. Substructures inside borate glass droplets

Liquid B_2O_3 did not dissolve and wetted the BN, but it dissolved sintering aid oxides Al_2O_3, Y_2O_3, and SiO_2. To investigate the nature of these glass droplets, SEM and EPMA analysis methods were used to detect features at the microstructural level. We purposely embedded oxidized specimens into epoxy and machined them until the cross sections of glass droplets appeared. Fig. 3.14 shows the cross section of a glass droplet after 4 hours of oxidation. White circular substructures were observed on the cross section of glass droplets which were caused by the liquid-liquid phase separation. The shape of this glass droplet was consistent with the observation reported by T. Wakasugi et al.[24-25] and W.R. Witzkev [11], indicating that B_2O_3 very poorly wets BN substrate. The contacting angle, as shown in the image, was larger than 90°. There was a small amount of glass liquid staying at the edge of the glass droplets. This portion of glass seemed to keep the whole glass droplet on the specimen surface. It was obvious that the bond between the glass droplet and BN substrate was so weak that some of them still fell off during our observation. There was not any chemical linkage between these two components with the same reason that BN was poorly dissolved in liquid B_2O_3 at high temperature.

White circular substructures were found isolated from their surrounding glass matrix. The preliminary semi-quantitative analysis carried out on an SEM machine (Philips XL 30 FEG SEM) indicated a higher Al and Y content on white circular features in comparison with those in the surrounding glass matrix. However, as mentioned in the experimental section, data provided by EDX in SEM was not highly accurate to help detect quantitatively elemental compositions of formed phases and boron.

Samples at oxidation times of 3, 9, 14 and 30 hours were subjected to EPMA measurement. Fig. 3.14 was the microstructure of cross section of the polished BNY specimen after 4 hours of oxidation. Elemental compositions of glass droplets are given in Table 3.6. Nitrogen was undetectable from this glass phases, neither in glass matrix nor in white circular features. The high Al and Y contents implied that they were dissolved in the generated borate. It was very interesting that these oxides were present at a relative similar ratio, roughly 5 to 7 atomic percentage, regardless of the oxidation time length.

Borate had a higher evaporation rate on the boundary of a glass droplet [26]. Thus, Al_2O_3 and Y_2O_3 would be expected to accumulate during the oxidation, resulting in the formation of a separate phase with a varied composition along the oxidation time. However, this was not true for this circumstance. The average ratio of oxide $Al_2O_3:Y_2O_3:B_2O_3 = 1:1.35:5.54$ was calculated from the data and it was found stable. The location of this composition is depicted in the ternary system $Al_2O_3-Y_2O_3-B_2O_3$ as in Fig. 3.15.

A hypothesis for this phase formation is that when first formed, borate easily dissolved the additive oxides to generate alumina and yttria borate. The evaporation of borate at a longer oxidation time causes the accumulation of alumina and yttria in the borates. The evaporation rate appeared to be faster on the boundary of glass droplets so that circular features formed at these areas first before being circulated to other deeper areas inside glass droplets. The competition between oxidation reaction of BN to form B_2O_3 and the evaporation of this B_2O_3 would end up into a steady state in which its chemical compositions were unchanged.

33

In summary, the oxidation test of BNY samples showed an interesting appearance of glass droplets. Optical microscopy was a simple but helpful technique to investigate the evolution of glass droplets along with the oxidation time. This mechanism is comparable to the theory of Breath figure. There were two stages of diameter development for a single droplet, in which the first stage related to the formation of glass droplets and the second stage related to the coalescence of small droplets to form bigger ones. The presence of substructure inside the glass droplets was caused by the liquid-liquid phase separation. Their higher and more reliable amount of Al_2O_3 and Y_2O_3 isolated them from the low Al and Y liquid borate matrix.

3.3.2. The oxidation of SiO_2-contained samples BNYS2 and BNYS6

The previous section 3.3.1 mentioned the oxidation behavior of samples containing sintering additives Al_2O_3 and Y_2O_3 but not SiO_2. In this section, we provide in detail the influence of these oxides in the presence of SiO_2 on the oxidation behavior of BN. As reported, the addition of SiO_2 critically improved the density and prevented the grain growth of BN compared to those samples did not contain silica. Therefore, the addition of SiO_2 was expected to help improving the oxidation resistance of BN.

3.3.2.1. The glass droplets and glass layer on the oxidized SiO_2-contained samples BNYS2 and BNYS6

Similar to the oxidation procedures conducted on BNY, oxidation tests were also

pursued on BNYS2 and BNYS6 samples. After the oxidation experiment at 1200°C in the flowing dry air at various time scales, samples were stored in humidity-free containers before being processed for the SEM and EPMA tests.

Specimens were handled in an extra dry nitrogen gas environment inside a glove box. The microstructure of a BNYS2 sample after very fast oxidation time of 0.5 hr is shown in Fig. 3.16. Different from what observed on a BNY sample, glass droplets were not seen, but an array of 0.2 μm white particles were observed. EDX analysis showed that these white features contain high Y content. The exposed surface showed a high alignment of BN flakes.

With the assistance of optical microscope, we discovered that the glass droplets also appeared on the BN surface. However, they were hardly observed at early oxidation times while a glass layer on every BN samples containing SiO_2 was apparently seen. The microscopic investigation at the cross section of the glass layer showed the appearance of glass droplets dispersed inside the glass scale. It meant that glass droplets were also formed during the oxidation of BN samples containing amorphous silica. However, the presence of the glass layer hindered their appearance.

Optical images of this glass droplet's diameter evolution are given in Table 3.7, Table 3.8, Fig. 3.17, and Fig. 3.18, correspondingly. The cross section of BN sample containing 2 wt% of SiO_2 after 4 hours of oxidation was given in Fig. 3.19.

Optical images of BNYS2 and BNYS6 in Fig. 3.17 (a) and Fig. 3.18 (a) all show the formation of a glass layer from a very early oxidation time, even before the emergence of glass droplets. Fig. 3.19 further illustrates the presence of the glass

layer on samples containing SiO_2. This was a critical different point from the oxidation behavior of BN samples not containing SiO_2 in which glass droplets appeared before the glass layer was formed.

The evolution of the maximum glass droplets size in BNYS2 and BNYS6 samples behaved analogously with that of BNY samples. They also displayed the breath figure pattern as depicted in Fig. 3.20. The difference between samples containing SiO_2 and not containing SiO_2 is manifested at the length of the plateaus and the height of jumping steps. The plateau in the cases of BNYS2 and BNYS6 samples is longer but their jumping step is shorter than those of BNY samples.

The formation of the glass layer on BNYS2 and BNYS6 surfaces as shown in Fig. 3.17 and Fig. 3.18 made the observation of glass droplets at early oxidation times more difficult though their formations were apparent as depicted in Fig. 3.21. The presence of this glass layer was also a cause to delay the coalescence of glass droplets and lower their maximum sizes. The biggest glass droplets in these two circumstances have smaller sizes than those of BNY samples. The plateau regions were prolonged and the jumping steps were shortened. Furthermore, the presence of this glass layer should also be a reason for a more scattering fluctuation of BNYS2 and BNYS6's glass droplets average diameters as seen in Fig. 3.22.

Data in Table 3.4 and Fig. 3.9 shows that weight loss of BNYS2 and BNYS6 samples were in the range, regardless of their different silica composition. This similarity may imply that the oxidation resistance of BN did not critically change with the addition of SiO_2 though its density is very much improved. Measurements on the weight

change of samples after oxidation also indicated the same tendency for all samples.

3.3.2.2. Composition of oxides on BNYS2 and BNYS6

While the glass droplets looked homogeneoudly through optical microscopy, electron microscopy showed them to have a sub-structure as observed in Fig. 3.23, which is similar to those observed in Fig. 3.14. EPMA measurements were conducted on the cross sections of BNYS2 samples at 9 hrs, 14 hrs and 30 hrs oxidation and for BNYS6 sample at 30 hrs of oxidation. The BNYS2 sample had a weight loss equal to 3.22 wt% at 9 hrs, 5.89 wt% at 14 hrs and 10.02 wt% at 30 hrs. Though the weight loss was considerable, what appeared on this image are the residues after the evaporation of B_2O_3.

We divided the cross section of the glass droplet shown in Fig. 3.23 into internal, external glass regions. We also examined chemical compositions of substructures in the internal and external regions. To better differentiate them, we called the internal glass region as internal glass matrix; the external glass region as external glass matrix; internal glass spheres and external glass spheres as seen in Fig. 3.23. Results obtained from these measurements at these three periods of time are shown in Tables 3.9, 3.10 and 3.11.

Assume that the evaporation of B_2O_3 was dominant on the surface of glass droplets, the spherical sub-structures would dominantly distribute in the external glass matrix. However, as shown in Fig. 3.23, they distributed in the internal glass matrix also. This phenomenon can be explained by the application of the "coffee-drop effect"

37

[21]. It is the fact that the evaporation of B_2O_3 was not isotropic across glass droplet's surface, but a higher rate at their edges. This anisotropic evaporation generated an intrinsic capillary flow to circulate spherical sub-structures into the internal regions of the glass droplet.

The circulation of spherical sub-structures may accompanied by the variation of their chemical compositions. As given in Table 3.9 and Table 3.10, internal glass spheres contain high B and Si contents (32 at% - 35 at%, 2.5 at% - 4.2 at%, correspondingly), while external glass spheres contain low B and Si contents (27 at% and ~1 at%). The variation of B content can be explained from its evaporation, which is consistent with its atomic percentage in the internal and external glass matrices. The evaporation of B not only increased the composition of Al and Y in these glass sub-structures, but also released Si into the glass matrix to increase its content in this region (22 at% - 25 at%).

Hypothetically, it is considered that these glass sub-structures absorbed SiO_2 when they were circulated inward the glass droplets together with some portions of B_2O_3. When they were exposed to the external regions of the glass droplet, these two components were released to bring its compositions to its steady state.

The different compositions of B, N and O between theoretical calculation and measurement in the region of the unoxidized BN may be caused by the higher borate content and lower sensitivity of B with this technique.

It was surprisingly that the Al and Y compositions in the external glass spheres are similar to those of glass substructures in the BNY samples. Compositions of these

38

two elements did not change also along with the oxidation time. The products of the oxidation reaction of BN are the same for all samples regardless of the usage of SiO_2.

Together with above explanation of the circulation of the glass sub-structures, it seemed to us that the oxidation mechanism of BN did not change within three samples BNY, BNYS2, and BNYS6. The most effective additives to improve the oxidation resistance of BN are Al_2O_3 and Y_2O_3 as they absorbed and released B_2O_3 and SiO_2 in their circulation loops. This would be an explanation for the slight difference of weight loss of all samples.

Fig. 3.24 illustrates the composition of all phases produced during oxidation of BNYS2 samples at 9 and 14 hours in which R_2O_3 indicates the total amount of Al_2O_3 and Y_2O_3. It is a clearer expression of the composition transformation along with the oxidation time. The longer the oxidation time was, the richer of R_2O_3 ($Al_2O_3+Y_2O_3$) in most of phases. The excessive evaporation of borate pushed the composition of the glass matrix closer to the SiO_2 corner.

The measurement of elemental compositions on BNYS6 samples at 30 hours of oxidation were conducted on glass droplets and results are given in Table 3.12. These data is another strong demonstration of the assumption about the role of Al_2O_3 and Y_2O_3 on the oxidation behavior of BN.

In summary, optical microscopy, SEM and EPMA methods were applied to investigate the oxidation behavior and quantitatively analyze the element distribution in phases formed from the BN oxidation. Glass droplets were formed on the surface of all samples, regardless of the use of SiO_2. The addition of silica would change the

order of appearance of these features. For samples not containing SiO_2, the glass droplets were seen at early oxidation times. Meanwhile, for samples containing SiO_2, the glass droplets appearance was hided inside the glass layer until they got large enough. The elemental composition varied systematically for all samples and for all oxidation times, implying a unique oxidation mechanism of BN. The addition of Al_2O_3 and Y_2O_3 was more effective to improve the oxidation resistance of BN from their stimulation with B_2O_3 evaporation. The microstructure and the presence of SiO_2 would not have a significant effect on this property of BN.

3.3.3. Weight loss during oxidation

Results of weight loss of BNYS2 and BNYS6 samples are the same, as depicted in Fig. 3.9. The weight change in BNY sample was slightly higher by about 2% at 30 hours of oxidation. The addition of SiO_2 seemed to decreasing the weight loss of BN which would be caused by the formation of the glass layer on BNYS2 and BNYS6 surfaces. This glass layer hindered the evaporation of B_2O_3, and may also the release of generated nitrogen gas. It is more evident from the slightly higher weight loss of BNY samples, where the glass layer did not form from early oxidation stages as seen in Fig. 3.14. Together with average particle size data; this experimental result supported the hypothesis that SiO_2 does not significantly influence the oxidation resistance of BN. However, a thorough understanding of this behavior is still needed and requires further experiments.
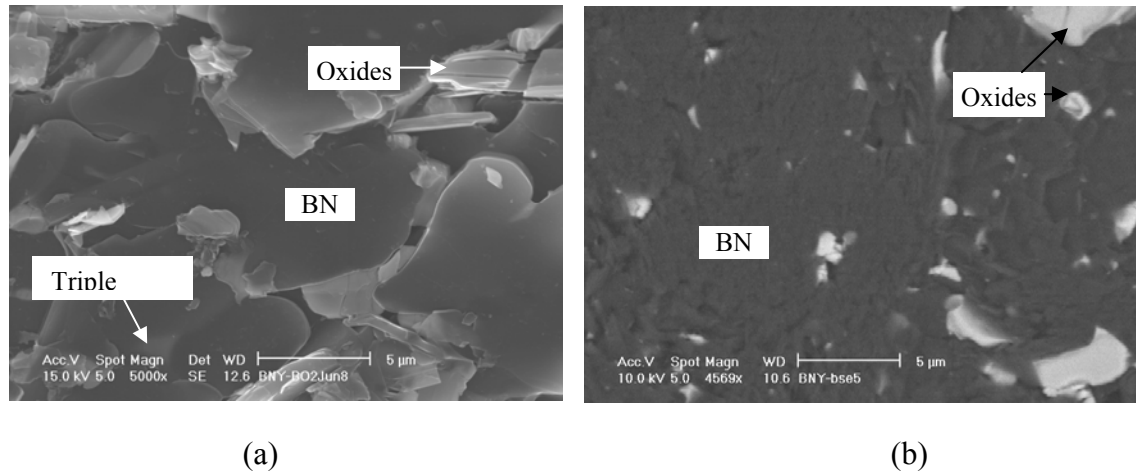
Fig. 3.1: The grain growth of BN platelets (a) and phase distribution in BNY sample (b)
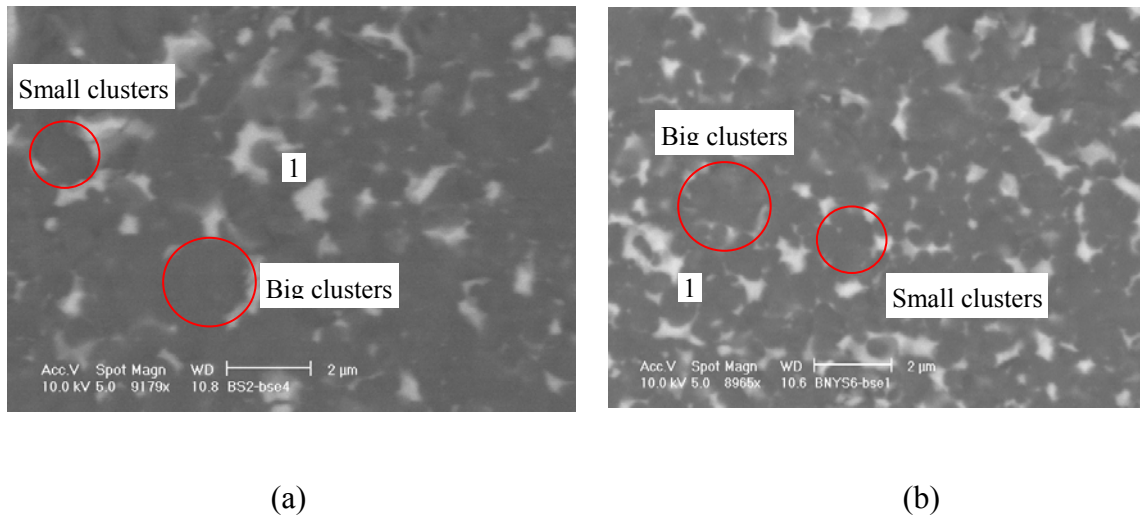
Fig. 3.2: The BSE images of BNYS2 (a) and BNYS6 (b) showing the even distribution of oxide phases thoroughly in samples.

Table 3.1: The crystal size and thickness of BN in the presence of oxides

	BNY	BNYS2	BNYS6
Crystal diameter (μm)	12-17	1.52-3.48	1.52-3.48
Crystal thickness (μm)	0.08-0.13	0.10-0.20	0.10-0.20
Relative density (%)	89.70	98.37	99.24
Porosity (%)	10.93	1.70	0.74
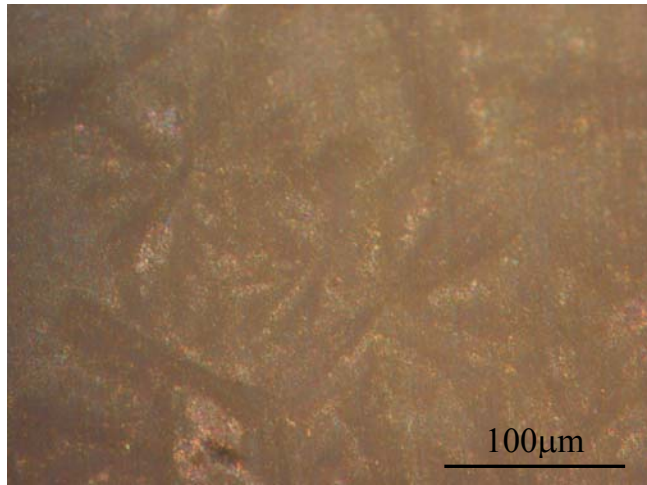
Fig. 3.3: Polarized microscopic image showing long features produced spherulite clusters on BNY surface
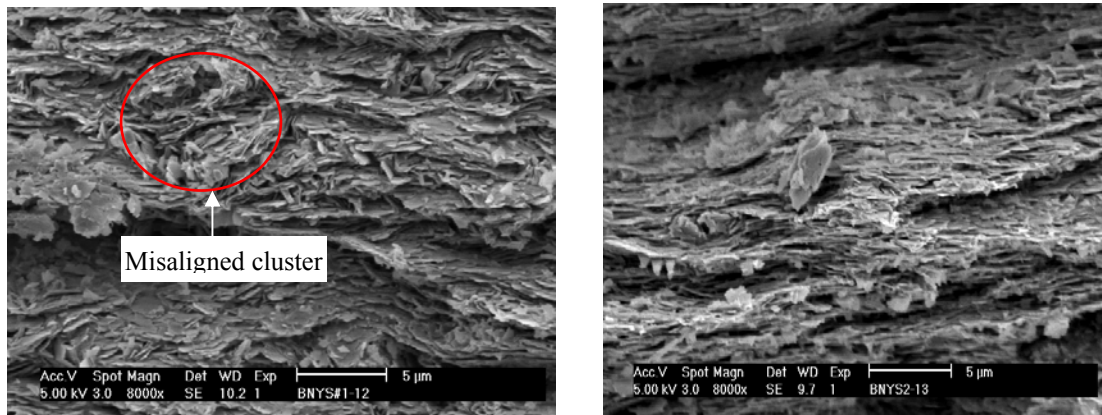
(a)   (b)

Fig. 3.4: Microstructure of the cross section of BNYS2 (a) and BNYS6 (b) samples, showing an internal cluster of misaligned BN particles in BNYS2. This phenomenon was not found in BNYS6 sample.

(a)   (b)
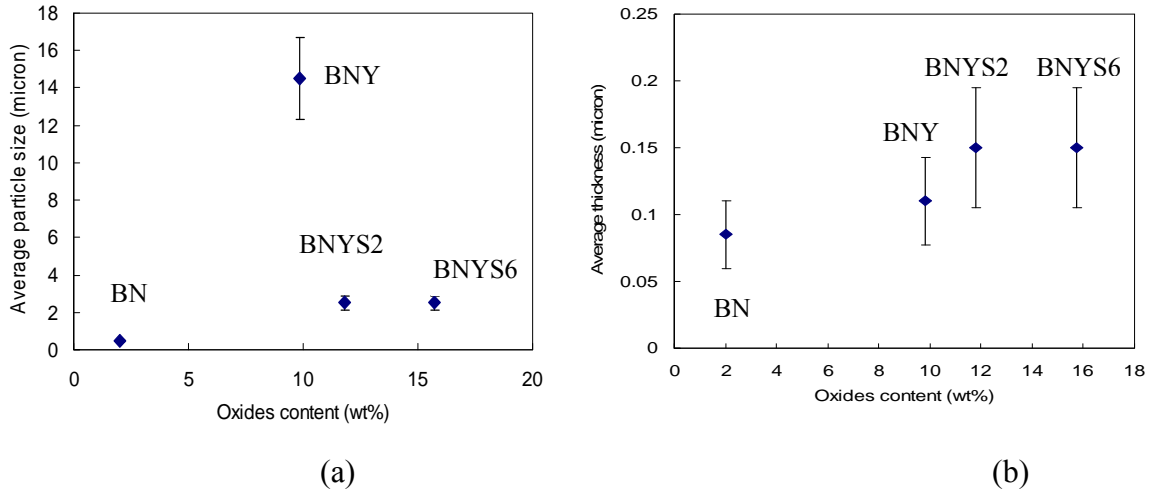
Fig. 3.5: The increase of BN particle size (a) and thickness (b) along with the oxides content.

Table 3.2: Flexural strength and elastic modulus of BN samples obtained from four-points bending test.

Sample	Oxide contents (wt%)	SiO$_2$ content (wt%)	Strength (MPa)	Modulus (GPa)
BNY	9.84	0	40.79	36.55
BNYS2	11.80	2	138.86	157.7
BNYS6	15.72	6	154.33	165.65

Table 3.3: The comparison with results reported by R.W. Trice and J.W. Halloran[9]

Samples	Oxides ratio	Flexural strength (MPa)
BNY	Al$_2$O$_3$: Y$_2$O$_3$:SiO$_2$= 1:3	40.79 $\pm$ 2
BNYS2	Al$_2$O$_3$: Y$_2$O$_3$:SiO$_2$= 1:3:1	138.86 $\pm$ 7
BNYS6	Al$_2$O$_3$: Y$_2$O$_3$:SiO$_2$= 1:3:3	154.33 $\pm$ 9
BN-22HA	Al$_2$O$_3$: Y$_2$O$_3$:SiO$_2$=1:7.44:5.56	117 $\pm$ 14
BN-22LA	Al$_2$O$_3$: Y$_2$O$_3$:SiO$_2$= 1:7.44:5.56	74 $\pm$ 4
BN-31LA	Al$_2$O$_3$: Y$_2$O$_3$:SiO$_2$= 1:7.44:5.56	105 $\pm$ 6

(*). Results from R.W. Trice and J.W. Halloran paper. HA and LA are the abbreviation of High Alignment and Low Alignment, respectively.

Table 3.4: The weight loss of samples along with oxidation time

	0.5h	1h	2h	3h	4h	5h	6h	7h	8h
BNY	-0.03	0.32	0.42	0.96	1.28	1.91	1.16	2.11	3.54
BNYS2	-0.01	0.14	0.25	0.52	1.27	1.52	1.69	1.87	2.12
BNYS6	-0.01	0.19	0.36	0.68	0.88	1.05	1.73	1.84	2.14

	9h	10h	11h	12h	14h	16h	18h	20h	30h
BNY	4.74	5.68	6.26	7.93	9.78	9.92	10.67	10.98	12.65
BNYS2	3.22	3.88	4.46	4.85	5.89	6.59	7.33	8.39	10.02
BNYS6	3.22	3.94	4.76	5.45	5.99	6.76	7.43	8.49	10.41
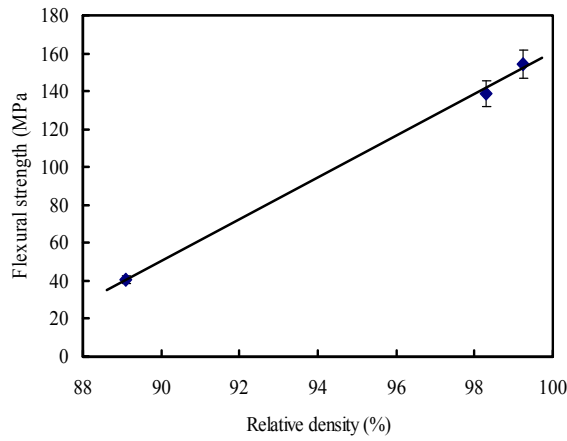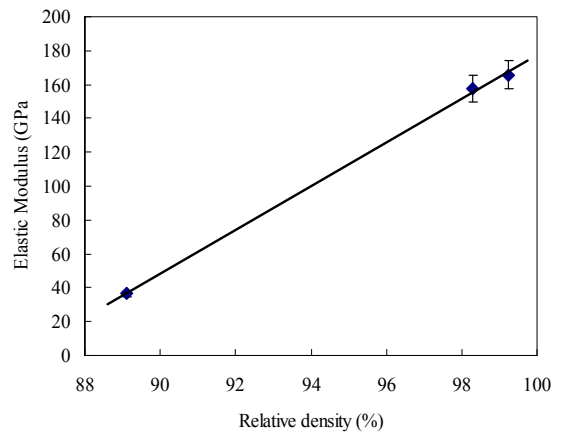
(a)   (b)

Fig. 3.6: The proportional relationship between flexural strength (a), elastic modulus (b) and relative density of BN.
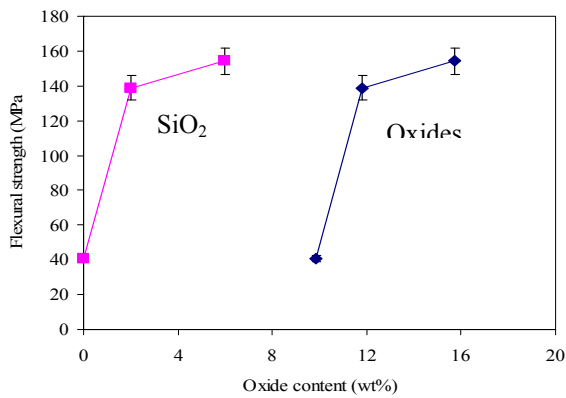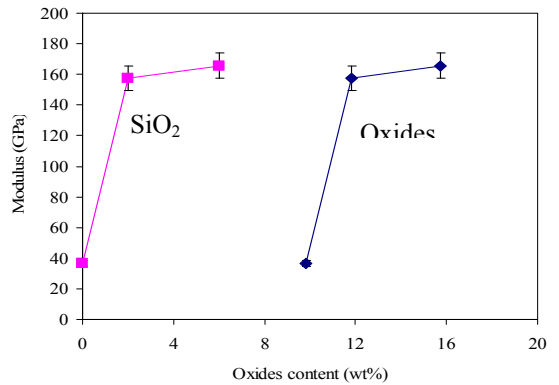
(a)   (b)

Fig. 3.7: The parabolic relationship of flexural strength (a) and elastic modulus (b) with oxide and silica content. The pink square points are of silica content and the blue diamond points are of oxides content.

44
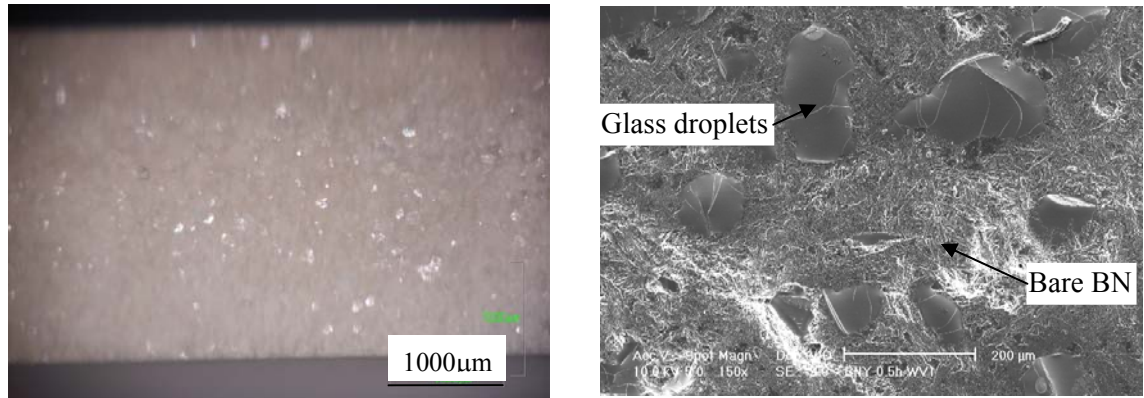
(a)

(b)

Fig. 3.8: Optical microscope (a) and SEM image (b) of BNY after 0.5 hour oxidation showing the appearance of glass beads.
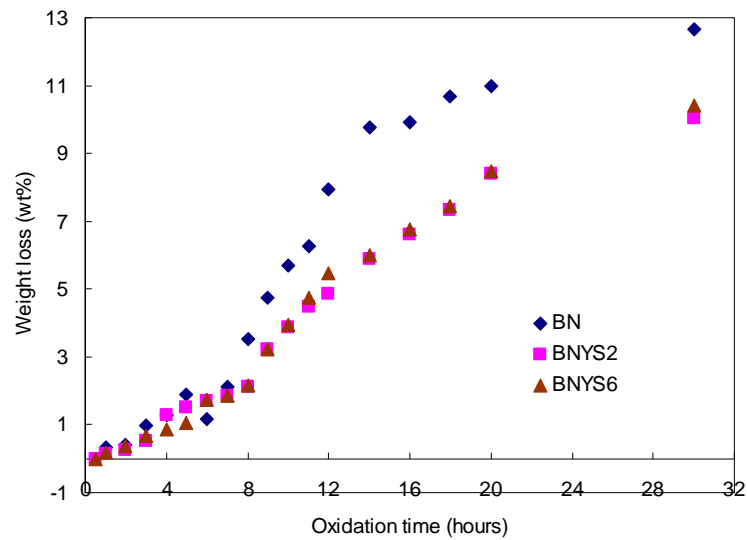
Fig. 3.9: The variation of sample weight with the oxidation time.

(a-1h)

(b-2h)
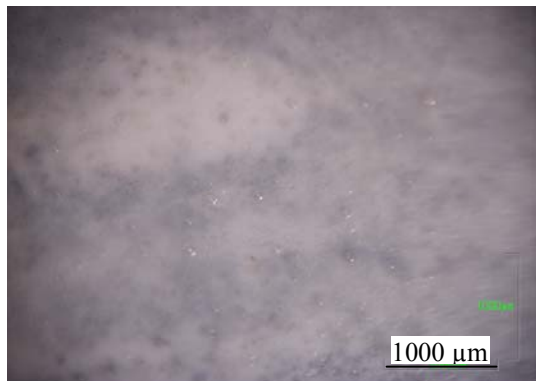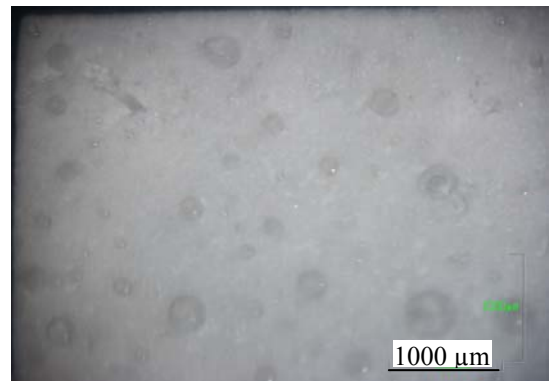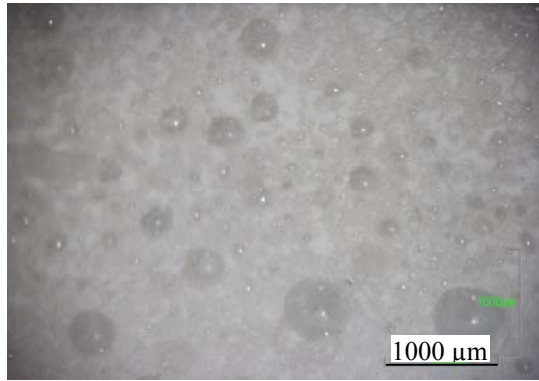
<center>(c-6h)   (d-10h)</center>
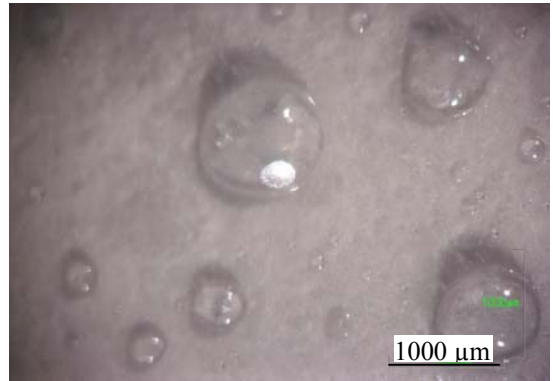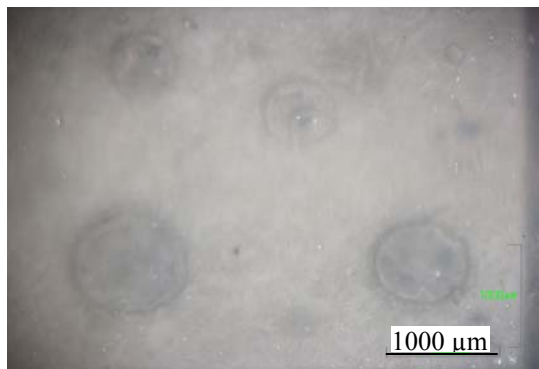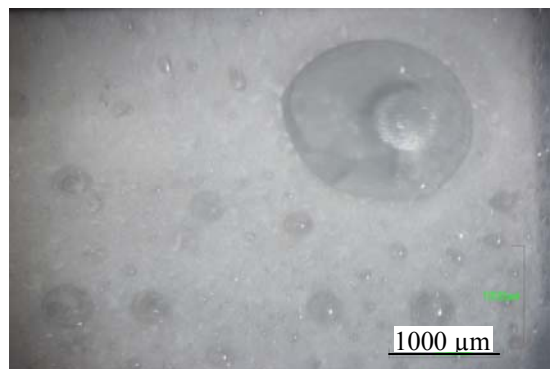
<center>(e-12h)   (f-16h)</center>
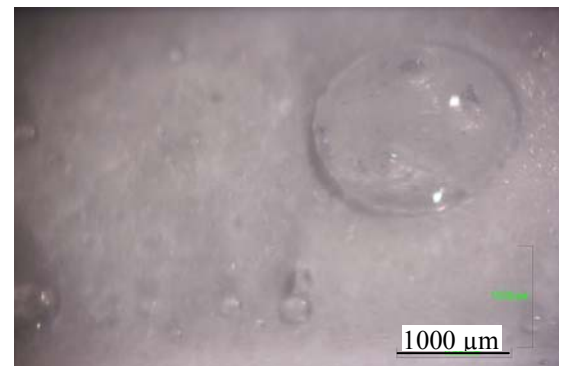
<center>(g-20h)   (h-30h)</center>

Fig. 3.10: The increase of glass droplet's diameters along with the oxidation time.
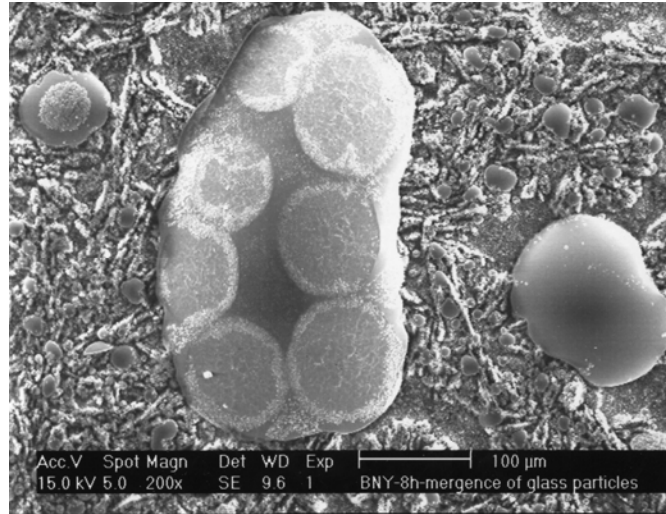
Fig. 3.11: The merging of small glass drops to form a bigger one in BNY sample. The white features might come from the hydration reaction.
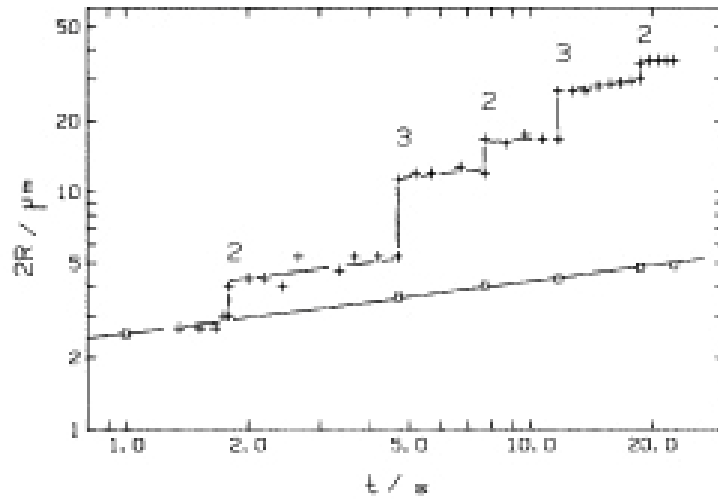
Fig. 3.12: Schematic illustration of the evolution of the two most important steps of breath figure. The growth of a single drop is expressed by the stepped curve and the development of average drops diameter is expressed by the linear line.[12]

Table 3.5: The biggest and average diameters of glass droplets on BNY sample with
the oxidation time

	0.5h	1h	2h	3h	4h	5h	6h	8h	9h
Biggest diameter	109.1	153.8	362.0	317.2	336. 7	342.9	446.1	564.3	905.0
Average Diameter	-	59.5	65.0	94.8	69.7	67.3	74.4	-	72.1

	10h	11h	12h	14h	16h	18h	20h	30h	
Biggest diameter	1036.2	1665.0	1674.2	1457	1377.8	1440.1	1435.3	1478.8	
Average Diameter	72.7	84.8	78.8	97.6	82.1	81.7	87.1	91.5	
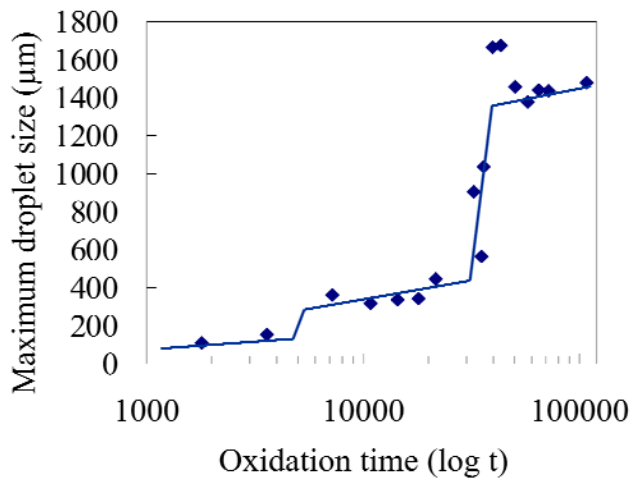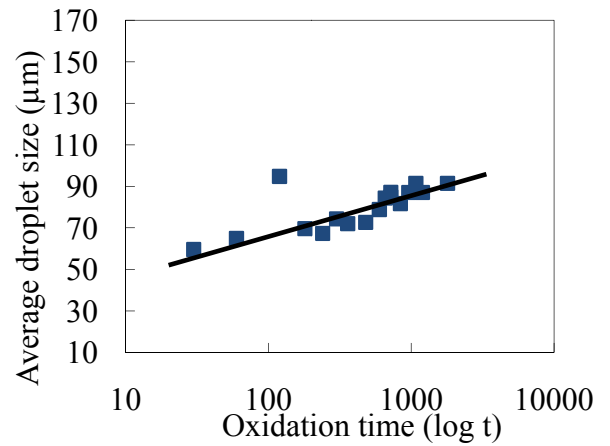
(a)   (b)

Fig. 3.13: The evolution of the biggest glass drop (a) and average glass drop size (b)
with the oxidation time.
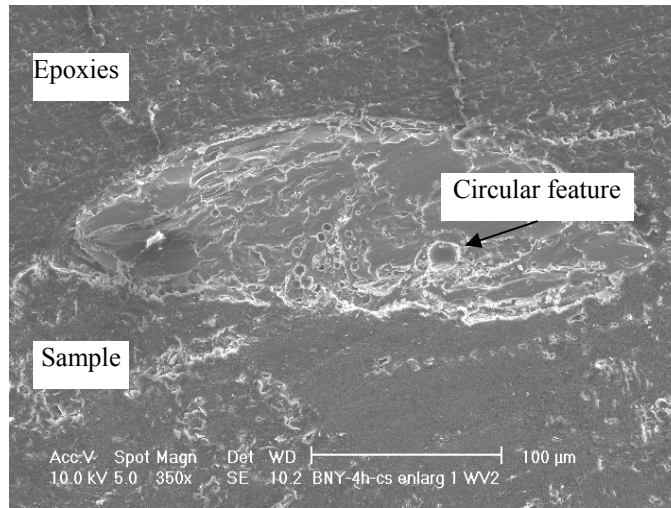
Fig. 3.14: Cross section of a glass bead produced on BNY surface after 4 hours of oxidation.

Table 3.6: Elemental composition of glass beads on BNY after 3, 9, 14 and 30 hours of oxidation

Time (hours)	B (at %)	N (at %)	O (at %)	Al (at %)	Y (at %)
3	29.96	-	58.75	5.10	6.54
9	28.54	-	58.69	5.23	7.54
14	29.34	-	58.39	5.55	7.38
30	29.20	-	59.49	5.23	6.93
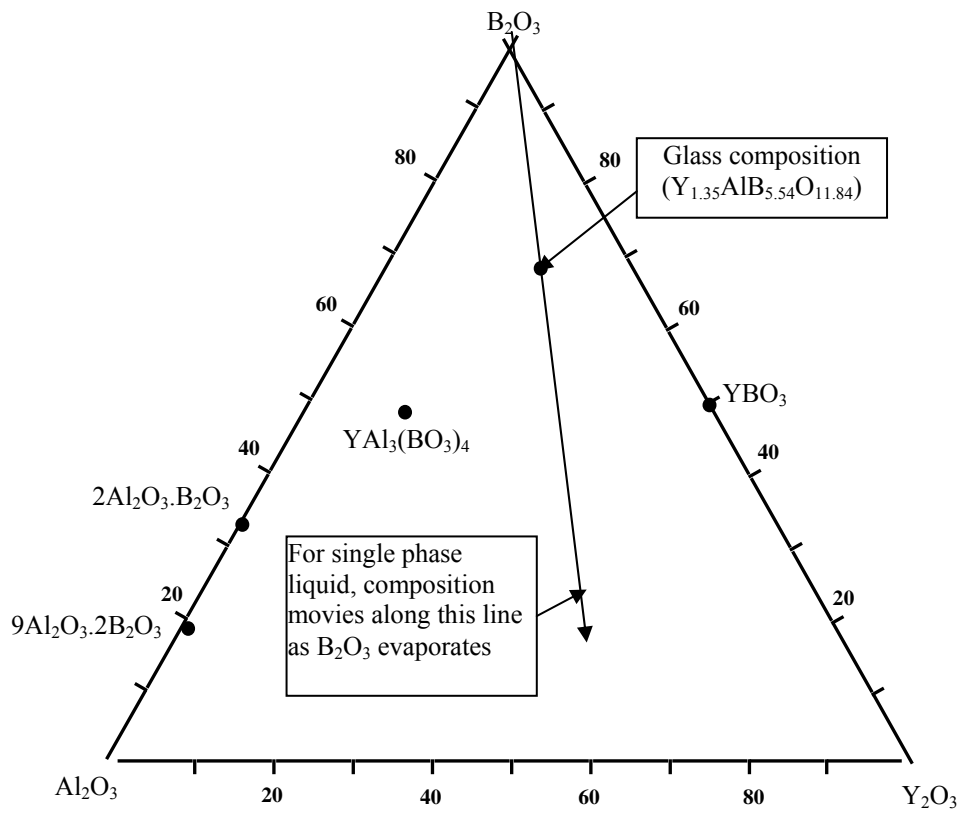
Fig. 3.15: Phase diagram of Al_2O_3-Y_2O_3-B_2O_3 system
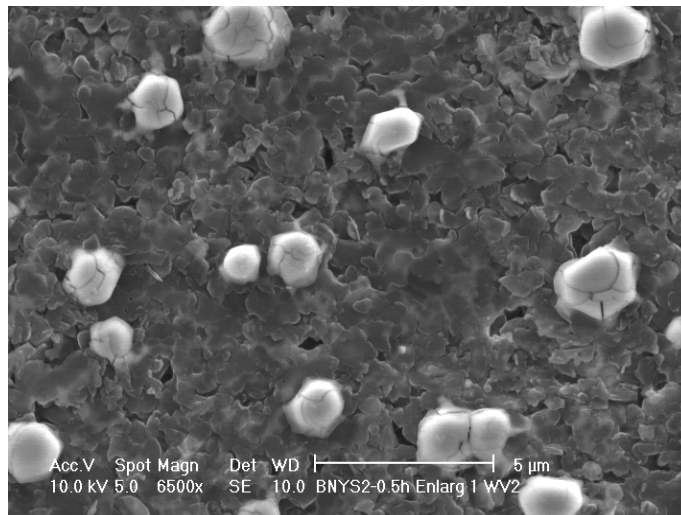
Fig. 3.16: Microstructure of BNYS2 after 0.5 hr oxidation

Table 3.7: The biggest and average diameters of glass beads generated on BNYS2 surface

	1h	2h	3h	4h	5h	6h	8h	9h
Biggest diameter	45.24	278.56	312.34	371.03	367.39	429.88	380.45	380.08
Average Diameter	33.3	65.05	83.6	92.13	70.82	64.12	-	92.31
	10h	11h	12h	14h	16h	18h	20h	30h
Biggest diameter	398.21	425.36	429.88	402.81	751.14	855.21	891.71	843.23
Average Diameter	72.24	84.71	85.21	97.64	82.07	84.72	90.42	101.44

Table 3.8: The biggest and average diameters of glass beads generated on BNYS6 surface

	1h	2h	3h	4h	5h	6h	8h	9h
Biggest diameter	40.29	262.48	280.54	325.82	307.72	366.54	411.49	344.38
Average Diameter	22.07	56.78	87.03	62.11	91.92	71.62	-	66.86
	10h	11h	12h	14h	16h	18h	20h	30h
Biggest diameter	380.11	407.23	425.33	411.75	607.14	696.84	739.04	754.21
Average Diameter	82.55	74.61	69.1	71.15	75.19	74.61	82.51	91.18

1000 μm

1000 μm

(a-1h)   (b-2h)

51

(c-6h)
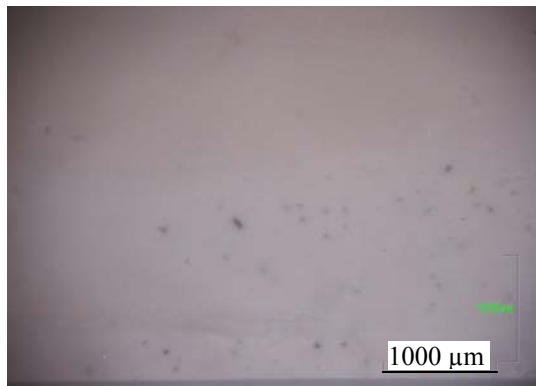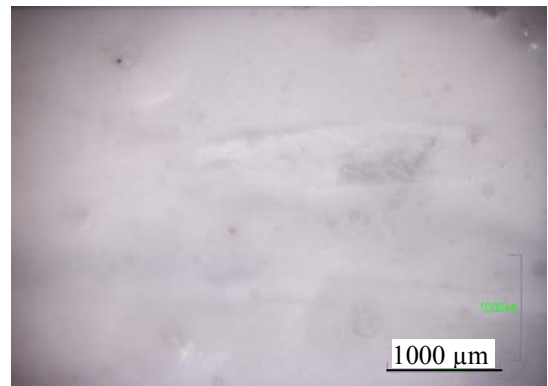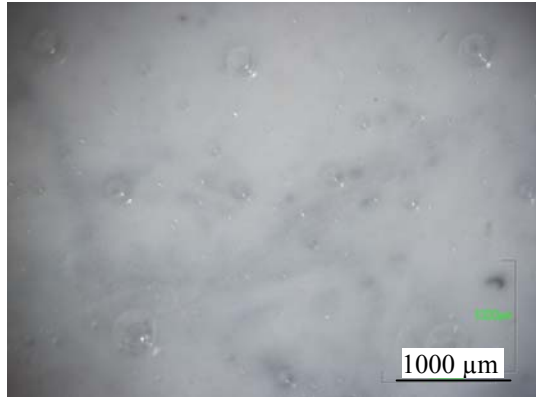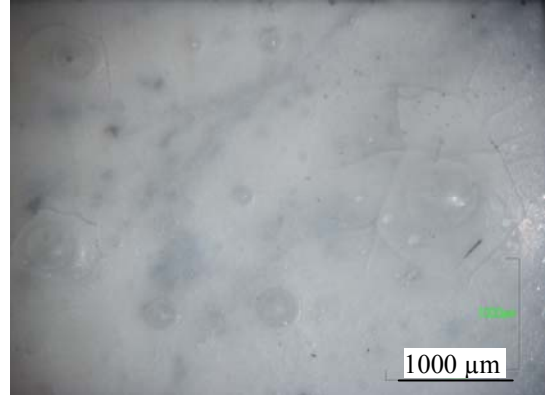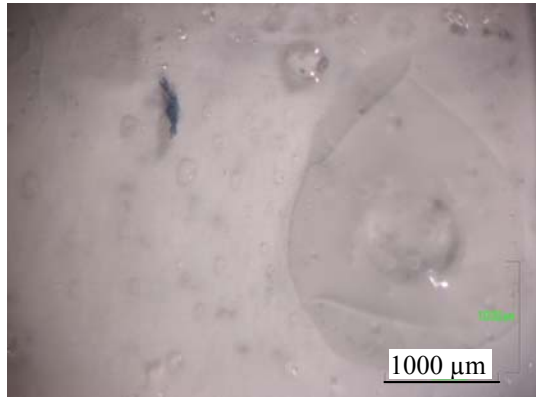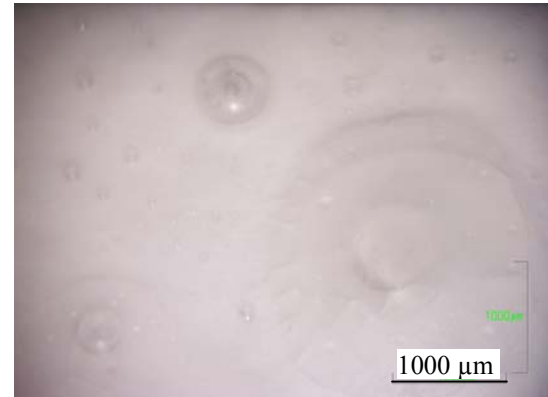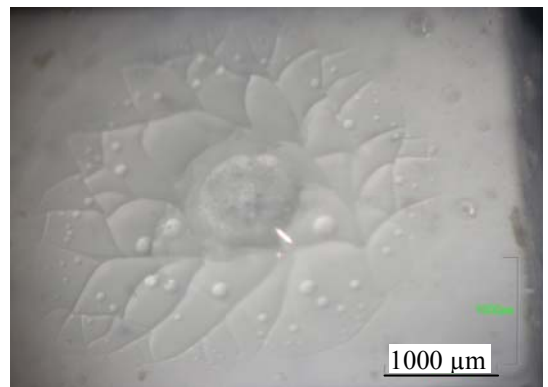
(d-10h)

(e-12h)

(f-16h)

(g-20h)

(h-30h)

Fig. 3.17: The advancement of glass droplet's diameters produced on BNYS2 sample surface with the oxidation time

(a-1h)

(b-2h)

(c-6h)
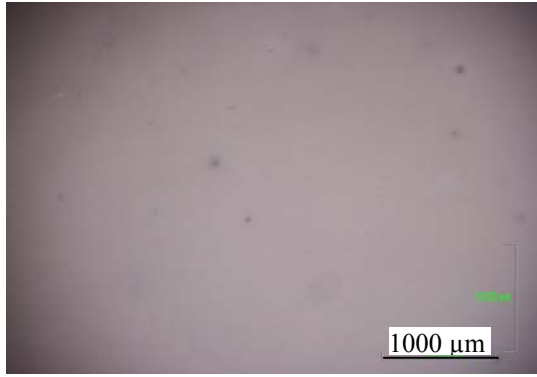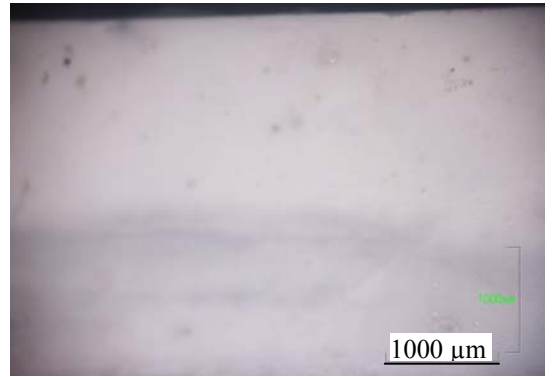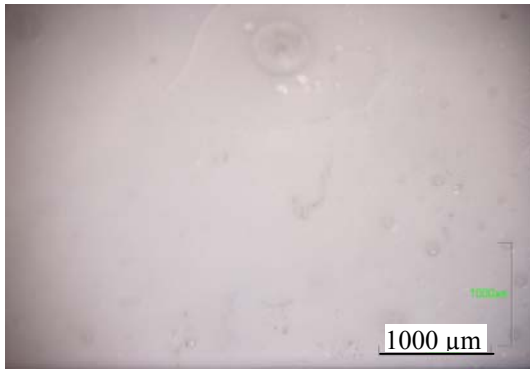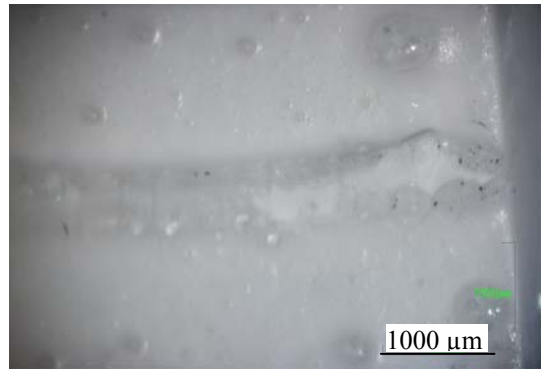
(d-10h)
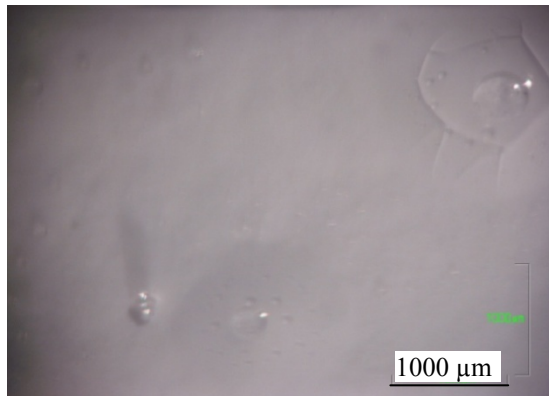
(e – 12h)
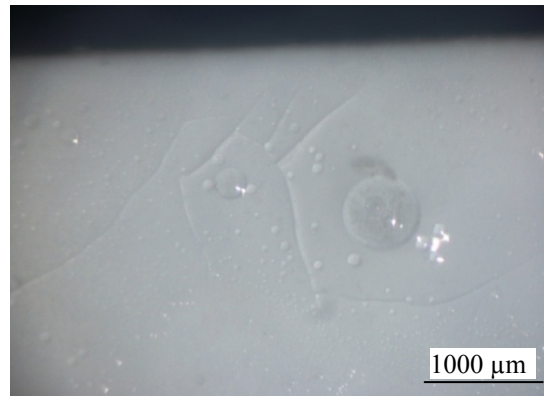
(f – 16h)
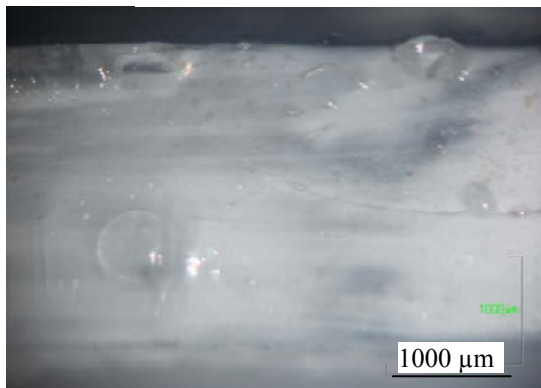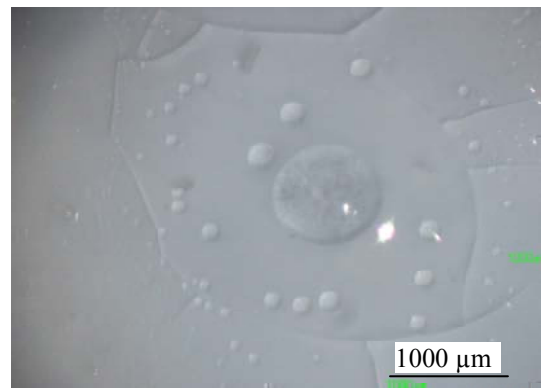
(g- 20h)   (h – 30h)

Fig. 3.18: The advancement of glass droplet's diameters produced on BNYS6 sample surface with the oxidation time
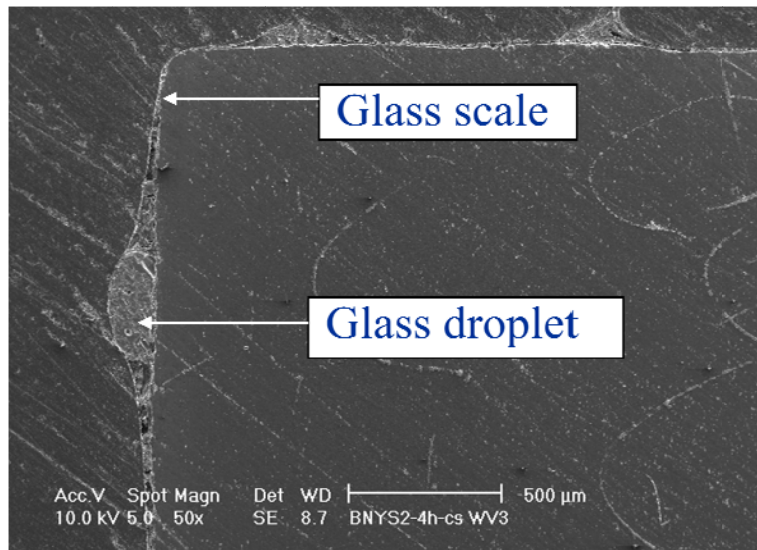
Fig. 3.19: Glass beads and glass scale on the surface of BNYS2 sample after 4 hrs oxidation

54
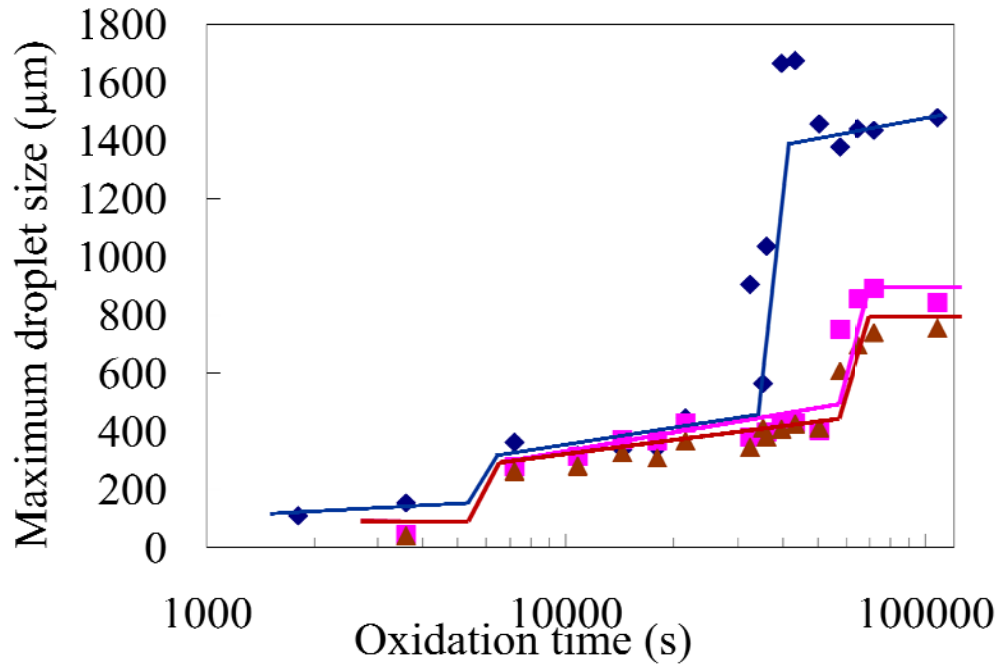
Fig. 3.20: The evolution of the diameter of the biggest glass drop in samples containing SiO_2 with the oxidation time.
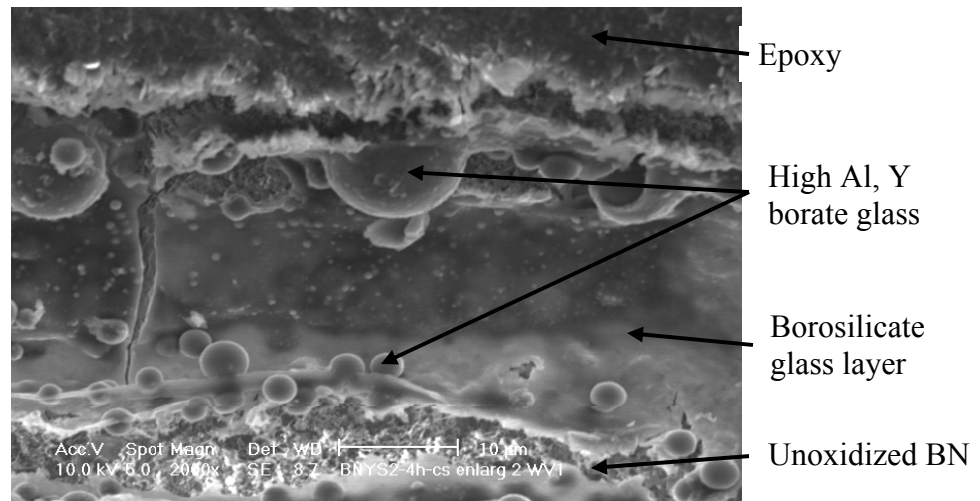
Fig. 3.21: The formation of glass droplets inside the glass layer on oxidized BNYS2 surface
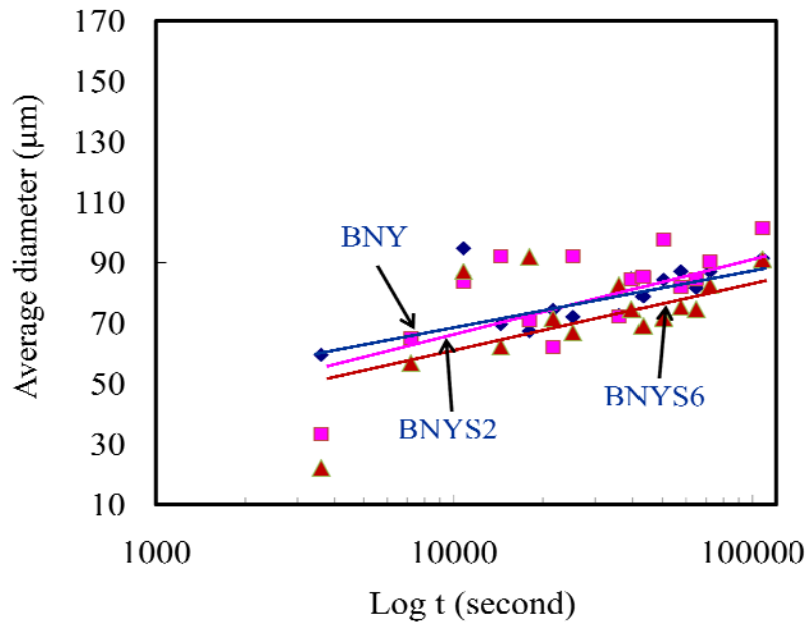
Fig. 3.22: The evolution of the average diameter of biggest glass drop in samples containing SiO_2 with the oxidation time.
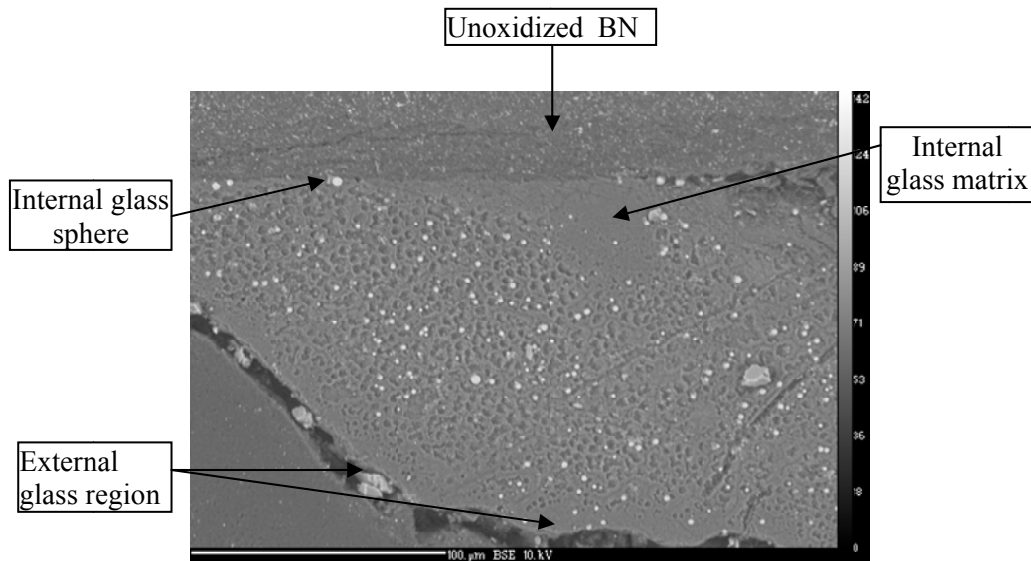
Fig. 3.23: Regions subjected to analyze in BNYS2 sample

Table 3.9: Elemental composition (at%) of phases in BNYS2 sample after 9 hours oxidation

	B (at%)	N (at%)	O (at%)	Al (at%)	Y (at%)	Si (at%)
Theoretical	47.78	47.78	2.76	0.53	0.71	0.45
Unoxidized	52.027	38.641	6.743	0.606	0.702	1.280
Internal glass matrix	32.72	-	67.557	0.141	0.018	2.778
External glass matrix	9.742	-	68.649	0.109	0.001	22.091
Internal glass sphere	31.71	-	65.076	0.274	0.038	4.249
External glass sphere	27.486	-	59.775	5.612	6.553	0.973

Table 3.10: Elemental composition (at %) of phases in BNYS2 sample after 14 hours oxidation

	B (at%)	N (at%)	O (at%)	Al (at%)	Y (at%)	Si (at%)
Theoretical	47.78	47.78	2.76	0.53	0.71	0.45
Unoxidized	52.027	38.641	6.743	0.606	0.702	1.280
Internal glass matrix	33.291	-	64.5	0.111	0.055	2.419
External glass matrix	19.407	-	56.67	0.165	0.008	24.835
Internal glass sphere	35.133	-	63.193	2.206	1.018	2.499
External glass sphere	27.028	-	59.813	5.174	7.361	0.624

Table 3.11: Elemental composition of glass beads in glass scale of BNYS2 sample after 30 hours of oxidation

	B	N	O	Al	Y	Si
Glass sphere (at%)	30.01	-	59.06	4.38	6.40	0.41
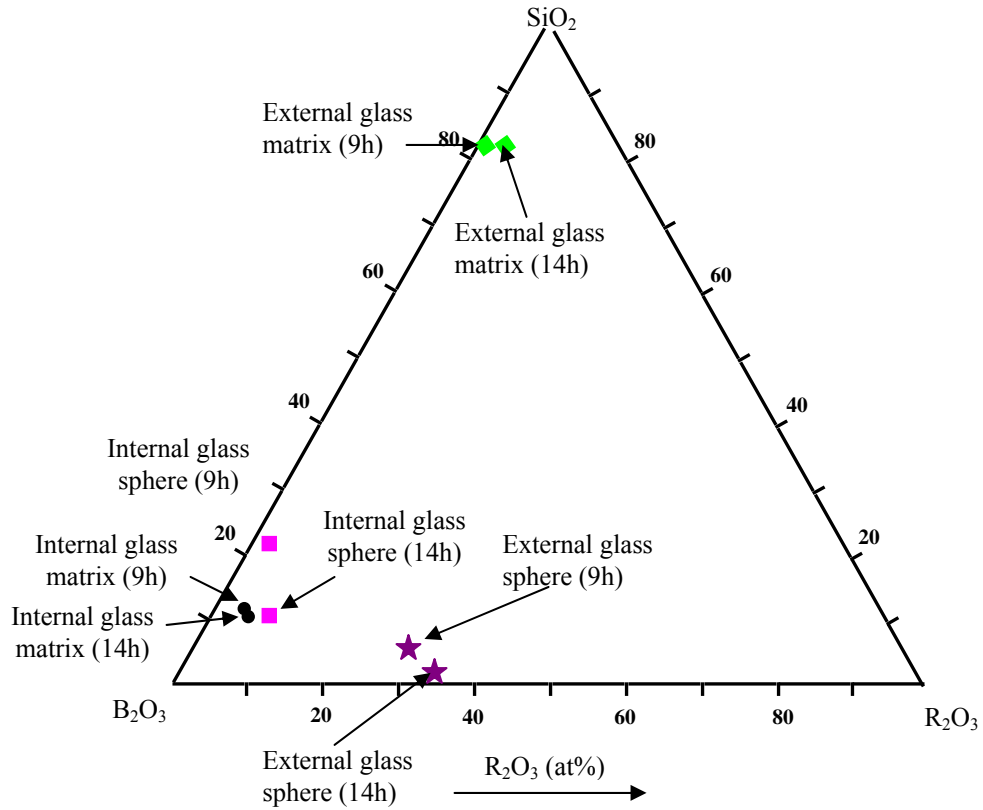
Fig. 3.24: The variation of composition of phases formed after 9 and 14 hours oxidation of BNYS2 sample

Table 3.12: Results of EPMA measurement on BNYS6 sample after 30 hours oxidation

	B (at%)	N (at%)	O (at%)	Al (at%)	Y (at%)	Si (at%)
Theoretical (at%)	46.36	46.36	4.64	0.53	0.71	1.37
Glass matrix (at%)	33.62	-	64.07	0.764	0.053	4.46
Glass sphere (at%)	25.67	-	60.52	5.48	7.50	1.28

References

1. S.L.Hwang, I.W.Chen, *Nucleation and Growth of beta-SiAlON.* Journal of American Ceramics Society, 1994. **77**(7): p. 1719-1728.
2. C.Wang, H.Emoto, M.Mitomo, *Nucleation and Growth of Silicon Oxynitride Grains in a Fine-Grained Silicon Nitride Matrix.* Journal of American Ceramics Society, 1998. **81**(5): p. 1125-1132.
3. L.S.Sigl, H.J.Kleebe, Journal of American Ceramics Society, 1995. **76**(3): p. 773-776.
4. B.Ertug, T.Boyraz, O.Addemir, *An Investigation of the Mechanical Properties and Fracture Characteristic of Hot-pressed Boron Nitride Ceramics.* Materials Science Forum, 2007. **554**: p. 201-205.
5. N.Jacobson, G.N.Morscher, D.R.Bryant, R.E.Tressler, *High-Temperature Oxidation of Boron Nitride: II, Boron Nitride Layers in Composites.* Journal of American Ceramics Society, 1999. **82**(6): p. 1473-1478.
6. N.Jacobson, S.Farmer, A.Moore, H.Sayir, *High-Temperature Oxidation of Boron Nitride: I, Monolithic Boron Nitride.* Journal of American Ceramics Society, 1999. **82**(2): p. 393-398.
7. B.Ertug, T.Boyraz, O.Addemir, *Microstructural aspects of the hot-pressed hexagonal boron nitride ceramics with limited content of boron oxide.* Materials Science Forum, 2007. **554**: p. 197-200.
8. M.Hubacek, M.Ueki, *Pressureless-sintered boron nitride with limited content of boric oxide* Materials Science Research Int'l, 1995. **1**(4): p. 209-212.
9. R.W.Trice, J.W.Halloran, *Influence of Microstructure and Temperature on the Interfacial Energy of Silicon Nitride/Boron Nitride Fibrous Monolithic Ceramics.* Journal of American Ceramics Society, 1999. **82**(9): p. 2502-2508.
10. C.L.Yeh, K.K.Kuo, M.Klimkiewicz, P.W.Brown, *Environmental Scanning Electron Miscroscopey Studies of Diffusioin Mechanism of Boron Particle Combustion.* Scanning, 1997. **19**(2): p. 114-118.
11. W.R.Witzke, *NACA Research Memorandum.* 1958, NACA.
12. D.Beysens, C.M.Knobler, *Growth of Breath Figure* Physical Review Letters, 1986. **57**(12): p. 1433-1437.
13. D.Fritter, C.M.Knobler, D.A.Beysens, *Experiments and Simulation of the Growth of Droplets on a surface (breath figures).* Physical Review A, 1991. **43**(6): p. 2858-2870.
14. J.L.Viovy, D.Beysens, C.M.Knobler, *Scaling Description for the Growth of Condensation Patterns on Surface.* Physical Review A, 1988. **37**(12): p. 4965-4970.
15. A.L.Porta, C.M.Surko, *convective Instability in a Fluid Mixture Heated from Above.* Physical Review Letters, 1998. **80**(17): p. 3759-3762.
16. A.V.Limaye, R.D.Narhe, A.M.Dhote, S.B.Ogale, *Evidence for Convective Effects in Breath Figure Formation on Volatile Fluid Surface.* Physical Review Letters, 1996. **76**(20): p. 3762-3765.
17. M.Haupt, S. Miller, R.Sauer, K.Thonke, A.Mourran, M. Moeller, *Breath Figures: Self-Organizing Masks for the Fabrication of Photonic Crystals and Dichroic Filters.* Journal of Applied Physics, 2004. **96**(6): p. 3065-3069.

18.   M.S.Park, J.K.Kim, *Broad-band Antireflection Coating at Near-Infrared Wavelength by a Breath Figure.* Langmuir, 2005. **21**(24): p. 11404-11408.

19.   M.S.Park, W.Joo, J.K.Kim, *Porous Strutures of Polymer Film Prepared by Spin Coating with Mixed Solvents under Humid Condition.* Langmur, 2006. **22**: p. 4594-4598.

20.   H.Yabu, M.Takebayashi, M.Tanaka, M.Shimomura, *Superhydrophobic and Lipophobic Properties of Self-Organized Honeycomb and Pincushion Structures.* Langmur, 2005. **21**(8): p. 3235-3237.

21.   R.Zheng, Y.O.Popov, T.A.Witten, *Deposit Growth in the Wetting of an Angular Region with Uniform Evaporation.* Physical Review E, 2005. **72**(4): p. 046303 (15 pages).

22.   R.D.Deegan, O.Bakajin, T.F.Dupont, G.Huber, S.R. Nagel, T.A.Witten, *Capillary Flow as the Cause of Ring Stains from Dried Liquid Drops.* Nature, 1997. **389**(23): p. 827-829.

23.   Thanh B. Do, John W. Halloran, *Breadth Figure Patterns in the Oxidation of Boron Nitride.* Journal of American Ceramics Society, 2007. **91**(8): p. 2730-2731.

24.   T.Wakasugi, F.Tsukihashi, N.Sano, *The Solubilitites of BN in B2O3 bearing Melts.* Journal of ANon-Crystalline Solids, 1991. **135**(2-3): p. 139-145.

25.   T.Wakasugi, F.Tsukihashi, N.Sano, *Thermodynamics of Nitrogen in B2O3, B2O3-SiO2, and B2O3-CaO Systems.* Journal of American Ceramics Society, 1991. **74**(7): p. 1650-1653.

26.   http://mrsec.uchicago.edu/Nuggets/Coffee/.

Part II

Dielectromagnetic Composites for Microwave Applications

Chapter 4: Introduction

4.1. Motivation of the research

This research is a continuation of the research conducted by Z.Wing [1] as a part of a joint project between the Department of Materials Science and Engineering, the University of Michigan and the ElectroScience Laboratory, the Ohio State University [2]. The portion that we contributed in this project was the formulation materials for Ultra Wide Bandwidth (UWB) conformal antennas. Wing, in his research was succeeded in forming various types of composites containing high permittivity dielectrics TiO_2/air, TiO_2/CMT (Calcium Magnesium Titanate) and textures of CMT with various dielectric permittivities. His materials assisted in reducing the dimensions of antennas to 40%. This dimension reduction was significant, but still far from required. Further reduction of antenna's dimensions caused decreasing the

performance of antennas. Limits of using dielectrics have been found as the reason of the impedance mismatch and field confinement [3]. These conclusions were comparable with the reports of others [4-7].

The impedance mismatch is a term to express the difference of resistance between the antenna, an electrical device to receive or send electromagnetic signal, and the air. All of electronic devices are working with 50 ohms resistance, while that value of the air is 377 ohms. Due to this reason, the metallic antenna requires a big and complicated appearance to compensate this discrepancy. It has been known that to minimize the size of antenna, a layer of magnetodielectric material should be applied on top of the metal antenna [8]. At the surface of this magnetodielectric material, the impedance can be expressed:

$$Z = i.Z_M.\tanh(\beta.h) \qquad\qquad (Eq.\ 4.1)$$

$$Z_M = (\frac{\mu_o.\mu(\omega)}{\varepsilon_o.\varepsilon(\omega)})^{1/2}$$

$$\beta = \omega(\omega_o.\varepsilon_o.\mu(\omega).\varepsilon)^{1/2}$$

Where Z_M is the wave impedance of the material and β is the propagation constant inside the material, ω is the angle frequency of the alternating field, and h is the thickness of the magnetodielectric material.

Electromagnetic waves, when meeting the surface of material, will lose some of its energy caused by a reflection:

$$R = \frac{Z-Z_o}{Z+Z_o} \qquad\qquad (Eq.4.2)$$

$$Z_o = \sqrt{\frac{\mu_o}{\varepsilon_o}} = 377\ Ohms$$

To cancel the reflection, impedance of the material should be made equal to that of impedance of the air Z_o.

Assuming that $\beta h \ll \pi/2$, then the expression of Z can be approximated as:

$$Z = i.\omega.\mu_o.\mu(\omega).h \qquad\qquad (Eq.4.3)$$

In this equation, the dielectric permittivity is cancelled. It implies that the material having only dielectric property is not able to provide the impedance match with the surrounding medium because it cannot interfere with the value of Z or the reflection coefficient [8-10]. The illustration of this explanation is given in Fig. 4.1.

Therefore, in the second stage of the project [2], magnetodielectric materials have been chosen. Theoretical calculations and simulations conducted by our partners from OSU showed that the dimension of antenna can be reduced by 10 times while still retaining its performance with the application of magnetodielectric materials which have equivalent permittivity and permeability. However, this is a very difficult task because there is not any ferrite powder which has high permeability at microwave frequencies. Research of Mosallaei and Sarabandi [3] applied axially ordered $Co_2Ba_3Fe_{24}O_{41}$ (Co_2Z) sintered plates those had both permittivity and permeability equal 16. They reported a very promising result in minimizing microwave absorber devices by applying plates of that sintered ferrite.

The use of rigid sintered ceramic plates was not appropriate to meet the requirements of flexibility, castability and/or moldability of the materials used in our project. There only one opportunity to meet all of the demands was to combine ceramic powders with a thermoplastic or an elastomer.

As Co_2Z ($Co_2Ba_3Fe_{24}O_{41}$) has high permeability at the microwave frequencies, it was used as a magnetodielectric powder. However, both of its permittivity and permeability magnitudes are decreased when it is in the powder form. Its permittivity magnitude was 12 and its permeability magnitude was 8.

4.2. Ceramics-polymer composites

The combination of a ceramics with a polymer has been of much interest because it provides a flexibility to control physical, dielectric, and magnetic properties of formulated composites. Advantages of this combination are lower costs, more facile processing, and low temperature production. Ceramics-polymer composites also contain properties that may not be present in their individual components [11-14].

Depending upon the distribution and the connectivity of filler particles inside the polymer/elastomer/epoxy matrix, composites can be categorized as 0-3, 1-3, and 2-3 types. In 0-3 composite, fillers are in the particulate form and they are uniformly distributed in the polymer matrix in the way so that they do not contact with each other [12, 15-16]. Similarly, the 1-3 or 2-3 composites contain the contact of filler ingredients along one direction (fiber) or two directions (laminar).

The application of 0-3 composite is more widely spread because the availability of powder ingredients. Almost all materials can be produced in powder form. Apart from it, the synthesis process is very much easier than those of 1-3 composites. However, the 1-3 or fiber composites consist of many characteristics such as mechanical strength those are very much better than those of particular composites due to the continuity of their components. Terminology 1-3 composites has also been used to describe anisotropic particular composites in which, particulates are in contact with each other and aligned uniaxially along one specific direction [15, 17-18].

In this research, we tried to formulate both 0-3 and 1-3 composites of Co_2Z with polymers. The 1-3 texture in this sense was not real fibers, but lines of magnetodielectric particles connected with each other along one direction. The tailoring 1-3 texture was an attempt to control the magnetodielectric properties of formed composites along a desired direction.

4.3. Outline of the part 2 of the thesis

Chapter 5 of the part 2 of this thesis will present an overview the magnetodielectric properties of magnetic materials: ferrites and garnets and relating them to material applications as well as material crystalline structure. This chapter will also describe in detail properties of ($Co_2Ba_3Fe_{24}O_{41}$) Co_2Z hexagonal ferrite and its synthesis techniques.

Chapter 6 presents the work on formulating and measuring data of flexible isotropic Co_2Z-PE composites with a variety of Co_2Z compositions, ranging from 10 to 45

vol%. Details of permittivity and permeability measurements will be described in this chapter.

The work in chapter 7 consists of two parts in which, the first mentions about formulation of anisotropic Co_2Z-Silicone elastomer composites via the application of the dieletrophoresis method. The second part mentions about the formulation of flexible Co_2Z-LDPE/HDPE materials with the application of coextrusion technique.

Theoretical calculations of the distribution of permittivity and permeability of magnetodielectrics - PE composites based on a classical Jayasandere-Smith model will be described in Chapter 8.
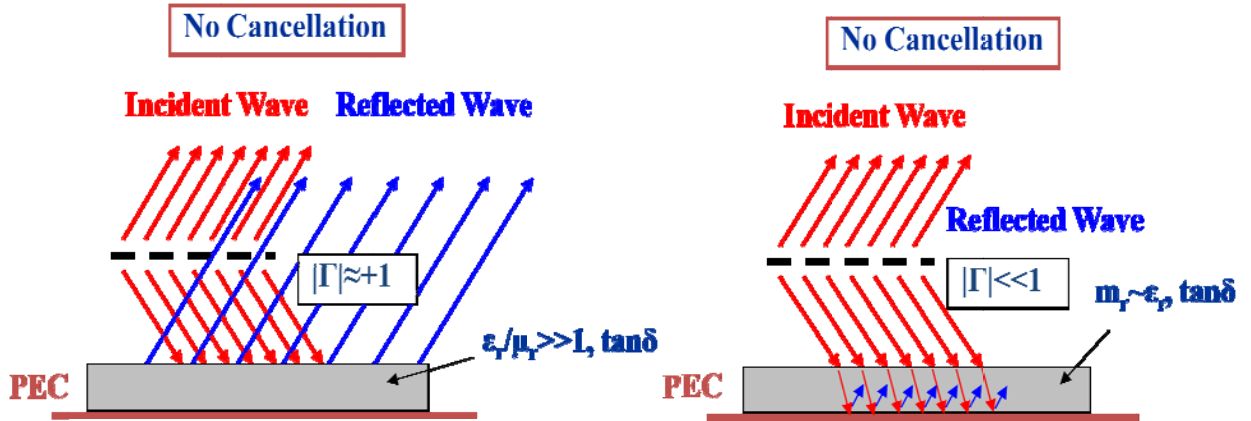
Fig. 4.1: Illustration of the advantage of applying magnetodielectric material to generate an impedance match to minimize the dimension of the antenna

References

1. Z.N.Wing, *Fabrication and Characterizatioin of Efective Medium Meta-dielectrics*, in *Materials Science and Engineering*. 2005, University of Michigan: Ann Arbor. p. 200.
2. F.Erkmen, C.Chen, S.Koulouridis, B.Kramer, I.Tzanidis, J.L.Volakis, J.W.Halloran, *UWB Conformal Antennas*. 2007.
3. H.Mosallasaei, K.Sarabandi., *Magneto-Dielectrics in Electromagnetics: Concept and Applications*. IEEE Transactions on Antennas and Propagation, 2004. **52**(6): p. 1558-1567.
4. V.R.K.Murthym, K.C.James Raju, B.Viswanathan, *Characterisitics of Materials for Microwave Devices*. Bulletin of Materials Sciene, 1992. **15**(3): p. 213-217.
5. M.J.Park, S.S.Kim, *Control of Complex Permeability and Permittivity by air Cavity in Ferrite-Rubber Compsite Sheets and Their ide-Band Absorbing Characteristics*. IEEE Transactions on Magnetics, 1999. **35**(5): p. 3181-3183.
6. D.Cruiskshank, *1-2 GHz Dielectrics and Ferrites: Overview and Perspectives*. Journal of European Ceramic Society, 2003. **23**: p. 2721-2726.
7. M.Matters-Kammerer, U.Mackens, K.Reimann, R.Pietig, D.Hennings, B.Schreinemacher, R.Mauczok, S.Gruhlke, C.Martiny, *Material Properties and RF Applications of High k and Ferrite LTCC Ceramics*. Microelectronics Reliability, 2006. **46**: p. 134-143.
8. H.M.Musal Jr., D.C.Smith, *Universal Design Chart for Specular Absorbers*. IEEE Transactions on Magnetics, 1990. **26**(5): p. 1462-1464.
9. Etienne Du tremolet de Lacheisserie, Damien Gignoux, Michel Schlenker, ed. *Magnetism: Magnetic Materials and Applications*. 2005, Springer Science and Business Media, Inc. p.33-63, 89-124, 181-189.
10. T.Inui, K.Konishi, K.Oda, *Fabrication of Broad-Band RF-Absorbers Composed of Planar Hexagonal Ferrites*. IEEE Transactions on Magnetics, 1999. **35**(5): p. 3148-3151.
11. N.G.Devaraju, E.S.Kim, B.I.Lee, *The synthesis and dielectric study of BaTiO3/Polyimide nanocomposite films*. Microelectronic Engineering, 2005. **82**: p. 71-83.
12. M.Olszowy, Cz.Paulacsyk, E.Markiewicz, J.Kulek, *Dielectric and pyroelectric Properties of BaTiO3-PVC composites*. Physica Status Solid A, 2005. **202**(9): p. 1848-1853.
13. S.D.Cho, S.Y.Lee, J.G.Hyun, K.W.Paik, *Comparison of Theoretical Predictions and Experimental Values of the Dielectric Constant of Epoxy/BaTiO3 Composite Embedded Capacitor films*. Journal of Materials Science: Materials in Electronics, 2005. **16**: p. 77-84.
14. P.S.Anjama, S.George, S.Thomas, G.Subodh, M.T.Sebatian, P.Mohanan, *Effect of Filer on the Microwave Dielectric Properties of PTFE/Ceramic Composites*, in *International Conference on Advanced Materials and Composites (ICAMC-2007)*. 2007: Trivandrum. p. 807-811.

15. L.F. Chen, Y.P. Hong, X.J.Chen, Q.L. Wu, Q. J. Huan, X.T. Luo, *Preparation and properties of polymer matrix piezoelectric composites containing aligned BaTiO3 whiskers.* Journal of Materials Science, 2004. **39**: p. 2997-3001.

16. M.Hase, M.Egashira, N.Shinya, *Development of Novel Method to Create Three-Dimensional Arrangements of Particles Using Dielectrophoresis in Artificially Nonuniform Electric Field.* Journal of Intelligent Material Systems and Structures, 1999. **10**: p. 508-515.

17. C.A.Randall, D.V.Miller, J.H.Adair, A.S.Bhalla, *Processing of Electroceramic-Polymer Composites using the Electrorheological Effect.* Journal of Materials Research, 1992. **8**(4): p. 899-904.

18. S.A.Wilson, G.M.Maistros, R.W.Whatmore, *Structure Modification of 0-3 Piezoelectric Ceramic/Polymer Composites through Dielectrophoresis.* Journal of Physics D: Applied Physics, 2005. **38**: p. 175-182.

Chapter 5

Magnetodielectric Materials

Magnetodielectric materials consist of several families such as (i) spinel, (ii) garnet, and (iii) hexagonal ferrites. These materials have a lot of advantages in resonators, microwave absorber devices, magnetooptical, and memory applications, etc. [1] based on their magnetic and dielectric properties. However, their properties will decline at high frequency ranges, majority beyond 10 MHz. Hexagonal ferrites containing a very complicated crystalline structure are magnetodielectric materials which are able to work in this microwave frequency range.

This chapter will explain some aspects of crystalline structures, the synthesis process and their effect on the properties of magnetic materials.

5.1. Spinel

Spinel is a common name for a crystalline structure of a number of compounds, which have different atom arrangements such as AB_2O_4, A_2BO_4, and $ABCO_4$, where A, B, and C represent cations. The cations appearing in these compounds must obey the condition that their total charge must be eight to balance the charge of oxygen.

Amongst those, AB_2O_4 is the most common formula because it is able to combine many elements to form different ferrites with a typical magnetic property. AB_2O_4 has a stable crystal structure in which A and B cations can flexibly occupy either tetrahedral or octahedral sites. Depending on the prior location of them, spinel is named as normal (all of A cations located in tetrahedral sites, all of B cations located in octahedral sites) or inverse spinel (half of B cations located in tetrahedral sites and all of A cations located in octahedral sites). This phenomenon occurs mostly on spinel ferrites whose Fe^{3+} cations do not have the crystal field stabilization energy [2-4]. The schematic illustration of the distribution of A and B in a normal spinel is given in Fig. 5.1. The magnetic properties of a spinel depend mostly on the distribution of d electrons of the trivalent cation, which in this case is Fe^{3+}. At a high-spin state, six d electrons of Fe distribute in a way so that the number of spin electron is maximum.

Two ferrites with the abbreviations of Ni-Zn and Mn-Zn are among the spinels which have found many applications in the radio frequency range (less than 100 MHz). The abbreviations stand for $Ni_xZn_{1-x}Fe_2O_4$ and $Mn_xZn_{1-x}Fe_2O_4$, correspondingly. The permeability of Ni-Zn is lower than that of Mn-Zn, but Ni-Zn can work in the whole range of frequencies up to 100 MHz. Mn-Zn ferrites can only be used in a moderate and low frequency range less than 10 MHz. The permeability of both Ni-Zn and Mn-Zn is also sensitive to the composition, especially to the oxygen stoichiometry.

5.2. Garnet

Garnet is the name of a group of natural minerals those have a common chemical composition $A_3B_2Si_3O_{12}$, in which A^{2+} is either Ca^{2+}, Mg^{2+}, Mn^{2+}, or Fe^{2+} and B^{3+} ion

can be Al^{3+}, Fe^{3+}, or Cr^{3+}. The natural garnet minerals do not have a magnetic property. If A^{2+} is replaced by Y^{3+} and B^{3+}, Si^{2+} are substituted by Fe^{3+}, the compound is called by another name as Yttrium Iron Garnet (YIG). This compound consists of the magnetism and it is categorized as ferromagnetism. Yttrium can be substituted by a variety of other rare-earth elements such as Lu, Yb, Ho, Tb, and Sm [3-4]. Garnet has a complicated crystal structure. Its unit cell contains eight formula units to show three kinds of cation sites: dodecahedral, octahedral and tetrahedral and these cation sites are usually distorted (Fig. 5.2 a-c).

The initial permeability of garnets ranges from the tens to hundreds. However, most of garnets can only retain their permeability magnitude to the frequency of few tens MHz.

5.3. Hexagonal ferrites

Hexagonal ferrite was first synthesized in 1952 [5], but it only gained the interest from researchers by the year of 1970s [6] due to the demand of materials which work at microwave and millimeter frequency ranges. It has a very complicated crystalline structure which is built from stacking of hexagonal and rhombohedral symmetries.

Typical hexagonal ferrite crystalline structures are M, S, X, Y, Z, and W [2-3, 7]. These letters usually stay after the symbol of the first cation in their formulas such as BaM ($BaFe_{12}O_{19}$), Co_2Y ($Co_2BaFe_{12}O_{22}$) or Co_2Z ($Co_2Ba_3Fe_{24}O_{41}$). The common phase diagram of these compounds is shown in Fig. 5.3. All of these compounds have been extensively investigated to improve their magnetic permeability magnitude [7-

8]. Though their magnetic property can be retained in the microwave frequency range, even in the range of a few GHz, their permeabilities are usually small. For example, the permeabilities of BaM and Co_2Y are around 4. This value is about a half of their dielectric permittivities which prevents their wider use in microwave absorber devices. Recently, Trans-Tech has succeeded in increasing the permeability of Co_2Z to a magnitude of 16 [9], equivalent to its permittivity in an ordered uniaxial alignment of hexagonal particles. In the powder form, this permeability deteriorates to obtain a lower magnitude of 8, which is smaller than its corresponding permittivity of 12.

5.4. Co_2Z

5.4.1. Crystalline structure of Co_2Z

This is a magnetic ceramic with hexagonal complex crystalline structure. It is the superposition of three types of blocks Spinel (S), ferromagnetic hexagonal (R), and antiferromagnetic hexagonal (T) in the order R.S.T.S.R*.S*.T*.S*. The Spinel S block is a two-layer building unit $(Fe_6O_8)^{2+}$ that does not include Ba^{2+} ions, the hexagonal R block is a block consisting three layers of $(BaFe_6O_{11})^{2-}$, and the T blocks are those consisting of a four layer unit of $Ba_2Fe_8O_{14}$ [7, 10-12]. Starred blocks are those of the same type with their original forms, but rotated 180° around the c-axis. Fig. 5.4 is an illustration of the arrangement of cations in the Co_2Z crystalline structure.

Further research on the Co$_2$Z crystalline structure has shown that Co$_2$Z consists of many inequivalent crystallographic sites (Wyckoff notations) which included 12k$_{vi}$, 2d$_v$, 4f$_{vi}$, 4e$_{vi}$, 4f$_{iv}$, 12k*$_{vi}$, 2a$_{vi}$, 4e$_{vi}$, and 4f*$_{vi}$ [10-12]. The characteristics of these sites are described in the Table 5.1, in which the orientation of spin is given in accordance to appropriate sites. This distribution explains the nature of the magnetic properties of Co$_2$Z.

5.4.2. Magnetic permeability of Co$_2$Z

As stated in the above section, the magnetic properties of most magnetic materials come from the presence of highly magnetic elements like Co and Fe. The presence of Co and Fe in the Co$_2$Z formula indicates its magnetization. However, given this complicated crystalline structure, ferromagnetic properties of Co$_2$Z are easily affected by the imposed environment, especially at elevated temperatures. As described in [13], Co$_2$Z contains three types of magnetic structures that differs by the orientation of their moments with respect to the hexagonal axis. At room temperature, the magnetic property is generated from the Cone of Easy Magnetization (CEM), at temperature range from 230 to 515 K, it is the Plane of Easy Magnetization (PEM) and the least symmetric magnetization appears when Co$_2$Z is exposed to temperatures higher than 515 K. The spins magnetic moment orient along the axis of easy magnetization (AEM).

In comparison to other ferrites in the same class, Co$_2$Z contains the highest magnetic permeability. Its initial permeability can reach 20 [14-15], depending on the synthesis

method, while that value of other compounds in the same class is less than 10. At frequencies higher than 10 MHz, Co_2Z's permeability is stable at 15 up to the frequency 1 GHz. Several researchers stated that this ceramics can be used at frequencies of 2 GHz [8, 16]. Meanwhile, the permeability of other structures remains high up to 300 MHz to 400 MHz.

Considering the chemical compositions, BaM ($BaFe_{12}O_{19}$) is the combination of RS blocks and Co_2Y ($Ba_2Co_2Fe_{12}O_{22}$) has structure of TS blocks. Co_2Z has superpositional structure of BaM and Co_2Y in order of RSTS and their reversion. Based on this understanding, many studies have tried to follow this route for the production of pure and high magnetic permeability Co_2Z [6, 13, 17-18].

5.4.3. Production of Co_2Z

The synthesis of Co_2Z is complicated and usually difficult. With its most complex crystalline structure, Co_2Z requires a long sintering time at high temperature [15]. It has been acknowledged that Co_2Z cannot be synthesized at temperatures equal and below 1100^oC. At 1250^oC, it is only partially formed. At temperature of 1350^oC, synthesized Co_2Z still contains a recognizable amount of impurities, either intermediate compounds BaM and Co_2Y or the ingredient oxides. The phase diagram of Co_2Z is given in Fig. 5.5. S. Kracunovska and J. Topfer [19] found that from 1000^oC to 1100^oC, BaM was a majority phase. Co_2Y is dominantly formed in the temperature range from 1100^oC to 1230^oC. Co_2Z is first formed at 1250^oC and is stable in the interval between 1300 and 1350^oC. The reaction consists of several

consecutive steps in which the compound formed in one reaction is the reactant of the following one. Each reaction involves a different reaction mechanism. Since reactions happen in the solid state, high temperatures and times are required to manifest the transportation of ions through layers of product. According to the calculation of Kingery D.W. [20], the conventional solid state reaction is never fully completed. It means that a certain amount of reactants are left as impurities. This is the reason why Co_2Z synthesized by the conventional solid state sintering method always contains an amount of oxides and intermediate compounds [8, 11, 15-16, 19, 21-22]. The high vaporization rate of cobalt oxide and especially barium oxide at high temperature also contributes to this challenge [16]. The phase diagram of Co_2Z is in Fig. 5.5.

There have been some efforts to eliminate this deficiency by applying different techniques. J. Jeong et al. [8] applied a two step method in which reactants were primarily heated at temperatures in the range of 900^oC and 1350^oC and the second step was conducted in the temperature range from 1250^oC to 1350^oC. Reactants of every step were ground and mixed by a planetary mixer. Authors showed a successful formation of single Co_2Z phase when reactants were first treated at 900 and 1100^oC and followed by the sintering at 1350^oC. Other batches of different primary and secondary heat treatments were mixtures of either two or three phases. They argued that intermediate compounds found at 900 and 1100^oC were facile to ground so that their surface areas are substantially higher than those pretreated at higher temperatures. This property, in turn, facilitated the transportation of ions for the formation of Co_2Z. Dong.H and Young H [16] tried to approach the even dispersion of cations from beginning by a sol-gel technique in which salts of Ba, Co and Fe were

hydrolyzed in a mixed medium of ethylene glycol, citric acid and water. Formed mixtures were colloidal and were then dehydrated by a heat treatment. When calcined, organic compounds either decomposed or evaporated to leave a solid of oxides. The high reactivity of cations at nano scaled distribution resulted in the complete reaction to form a single Co_2Z phase.

Researchers have tried to decrease the synthesis temperature to below 1300^oC, and some of them succeeded. D.W.Hahn and Y.H.Hahn [16] added Bi_2O_3 and CuO into the mixtures of oxides that were prepared by the sol-gel method. Components were used in the form of metalorganic salts. When hydrolyzed, their hydroxides formed, in which cations are evenly distributed into each other. Bi_2O_3 and CuO acted as sintering aids to form the liquid medium for the reaction; the break of old atomic-atomic bonds were easier as well as the formation of new bonds. Co_2Z was found to be completely formed at temperature of 1250^oC, which is 100^oC lower than that of the conventional method (1350^oC). This was a big step in eliminating the evaporation of cations. In comparison with the mechanism of the solid state reaction, the reaction to produce Co_2Z in a liquid medium follows a different direction, by which the contribution of intermediates was less significant. However, there has not been any report that explains it in detail.

S. Kracumovska and J. Topfer [19] did not success in reducing the sintering temperature by applying a co-precipitation method. The hydroxides of Ba, Co and Fe were made from their acetate solution by the gradually addition of citric acid. They found that the optimal synthesis temperature for Co_2Z is at 1330^oC. The elevation of

this value above 1350°C cause the melting of produced Co$_2$Z and this liquid did not return to its crystalline Co$_2$Z solid.

However, these techniques faced a challenge of low permeability of synthesized Co$_2$Z. As discussed above, the permeability of Co$_2$Z is very dependent upon the orientation of single crystals. The above described methods resulted in a randomly oriented crystallographic structure Co$_2$Z, together with the dilution from the presence of sintering aids, so that its permeability was lower than that of the optimal value of 16.

None of the research reporting high permeability of Co$_2$Z has been widely applied to manufacturing this ferrite at industrial scales. Trans-Tech Skyworks, Inc. is the only company that succeeded in renovating the synthesis method, in which reactants were intermediates BaM and Co$_2$Y for the synthesis of Co$_2$Z. The dielectric permittivity and magnetic permeability together with their losses of Co$_2$Z from Trans-Tech are depicted in Fig. 6.1 and Fig. 6.2 of Chapter 6. These data were obtained from measurements of randomly distributed Co$_2$Z powder. The magnetic permeability of uniaxial Co$_2$Z was measured as of 16, similar to those reported by other researchers above. This ferrite has the best quality currently on the market. Therefore, we applied it for our research in producing ferrite-polymer composites for microwave applications.
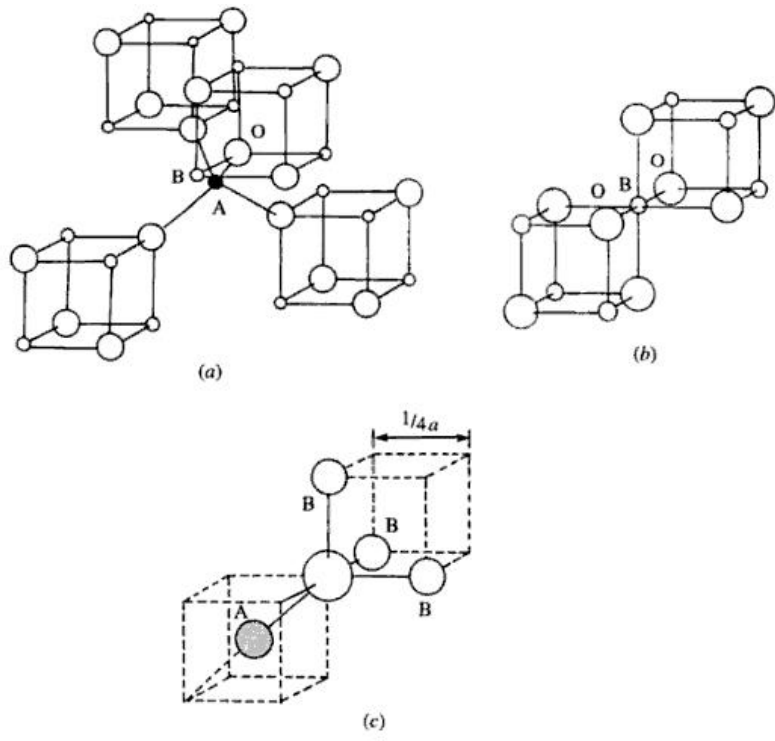
Fig. 5.1: Distribution of A and B cations in tetrahedral and octahedral sites [3]
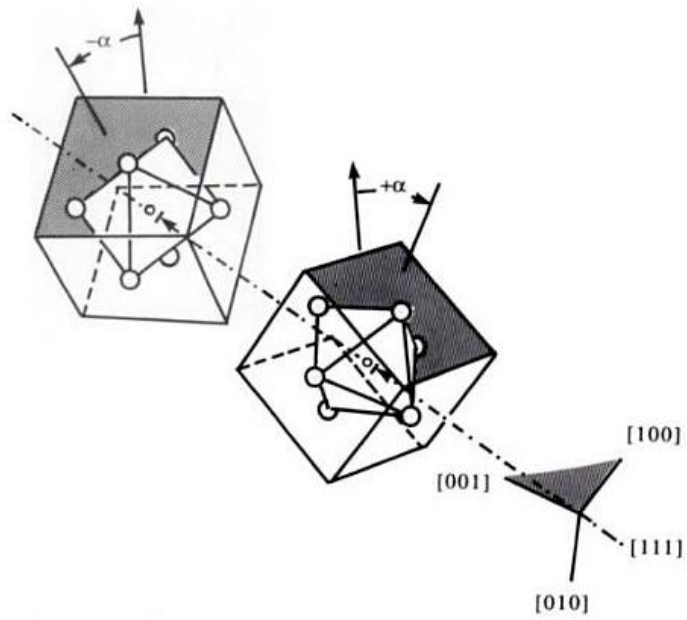
Fig. 5.2a: Distortion of octahedral sites to [111] direction in garnet crystal structure[3]
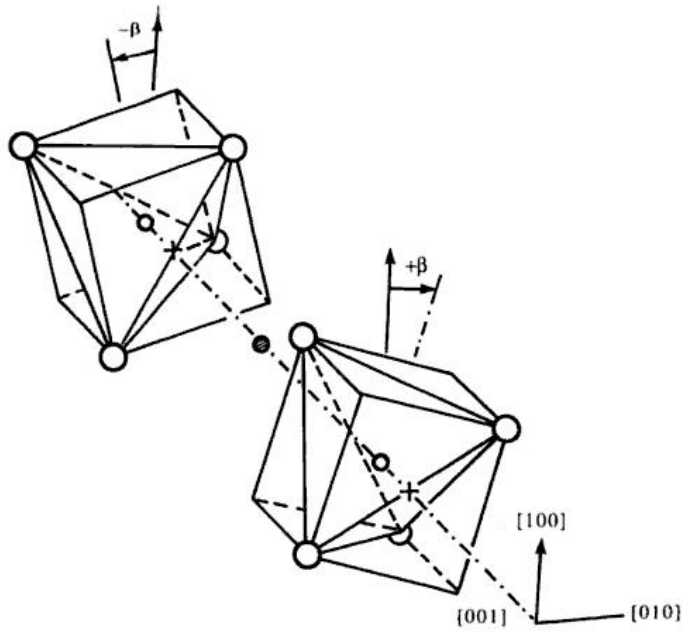
Fig. 5.2b: Distortion of tetrahedral sites along <110> direction in garnet crystal structure [3]
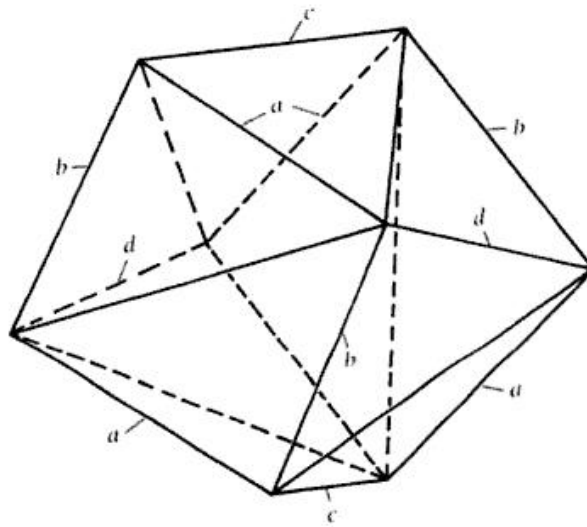
Fig. 5.2c: Dodecahedral sites of garnet crystal structure [3]
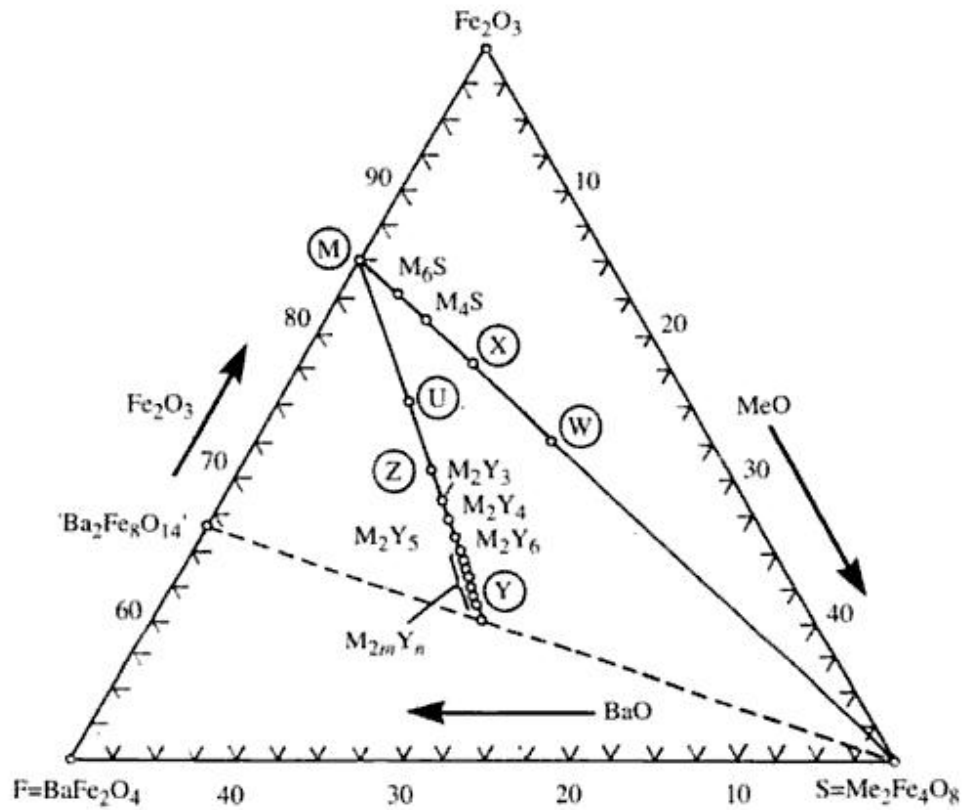
Fig. 5.3: Common phase diagram of hexagonal ferrites M, S, X, Y, Z, W [3]

Table 5.1: The distribution of inequivalent crystallographic sites (Wyckoff notation) [18, 23]

Site	Coordination	Block	Number of ions	Spin	Component
$12k_{vi}$	Octa	R-S	6	↑	
$2d_v$	Fivefold	R	1	↑	I
$4f_{vi}$	Octa	R	2	↓	
$4e_{vi}$	Octa	T	2	↓	
$4e_{iv}$	Tetra	S	2	↓	II+IV
$4f_{iv}$	Tetra	S	2	↓	
$4f*_{iv}$	Tetra	T	2	↓	
$4f*_{vi}$	Octa	S	2	↑	
$12k_{vi}$	Octa	T-S	6	↑	III
$2a_{vi}$	Octa	T	1	↑	
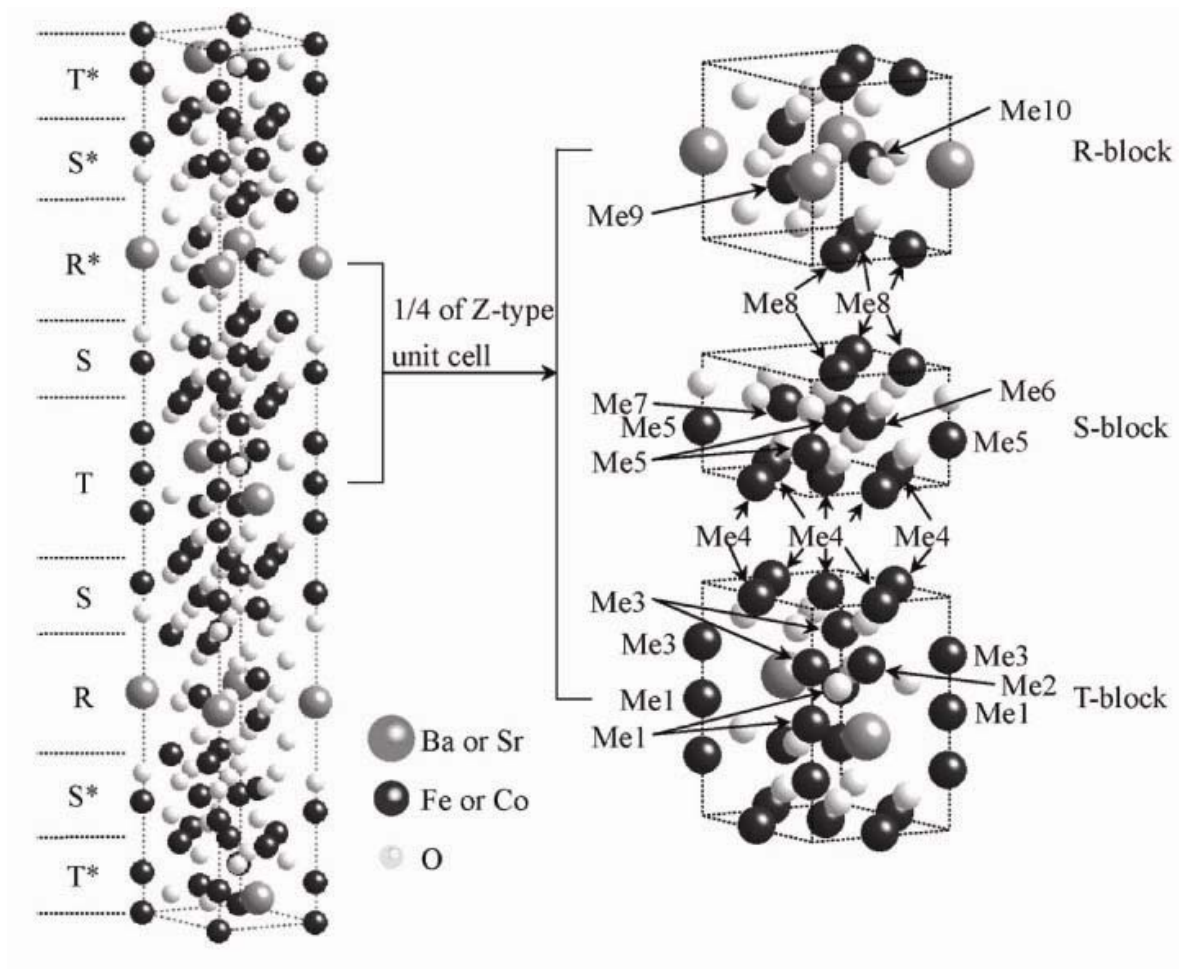
Fig. 5.4: Schematic illustration of crystal structure of Z-type ferrite [11-12]
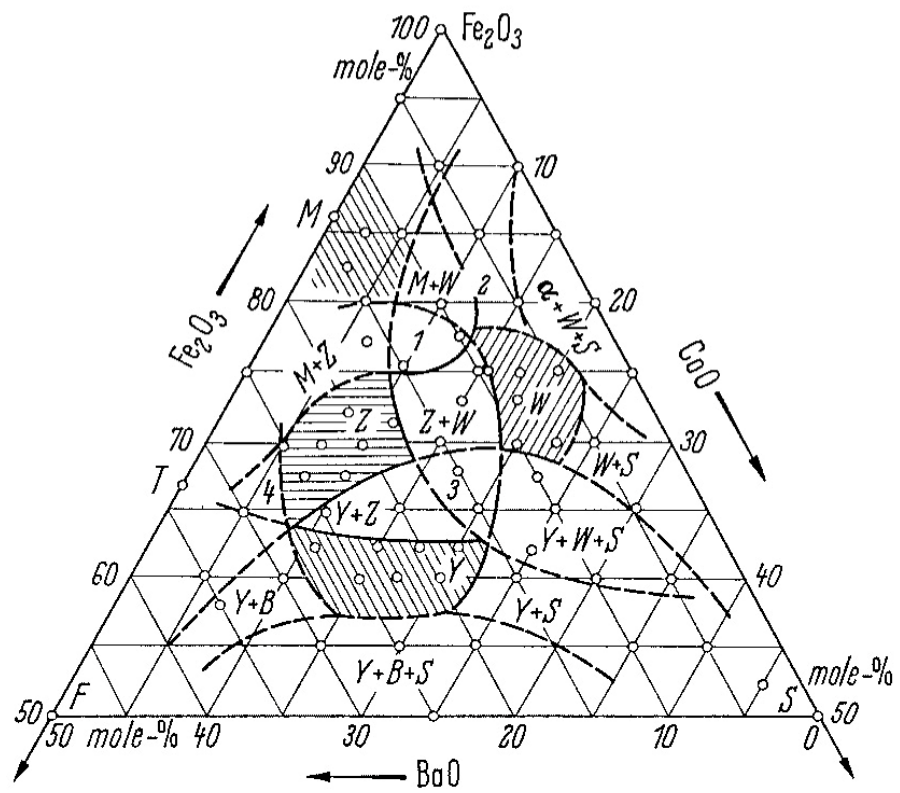
Fig. 5.5: Phase diagram of Co$_2$Z (Ba$_3$Co$_2$Fe$_{24}$O$_{41}$) [24]

References

1.   Weiguo Qu, XiaoHui Wang, Longtu Li, *Preparation and Performance of NiCuZn-Co2Z Composite Ferrite Material.* Journal of Magnetism and Magnetic Materials, 2003. **257**: p. 284-289.
2.   Goldman, Alex, ed. *Handbook of Modern Ferromagnetic Materials*. 1999, Kluwer Academic Publishers.
3.   Valenzuela, Raul, ed. *Magnetic Ceramics*. Chemistry of Solid State Materials. Vol. 4. 1994, Cambridge University Press. p. 13-20, 24-33.
4.   Etienne Du tremolet de Lacheisserie, Damien Gignoux, Michel Schlenker, ed. *Magnetism: Magnetic Materials and Applications*. 2005, Springer Science and Business Media, Inc. p.33-63, 89-124, 181-189.
5.   Xiaohui Wang, Tianling Ren, Longtu Li, Xhilun Gui, Shuiyan Su, Zhenxing Yue, Ji Zhou, *Synthesis of Cu-modified Co2Z Hexaferrite with Planar Structure by a Citrate Precursor Method.* Journal of Magnetism and Magnetic Materials, 2001. **234**: p. 255-260.
6.   E.M.C.Huuser-Gerits, G.D.Rieck, *Changes in Microstructure of Oriented Ba3Co2Fe24O41 Material During Sintering. II.* Journal of Applied Crystallography, 1976. **9**: p. 18-28.
7.   Hongguo Zhang, Longtu Li, Ji Zhou, Zhenxing Yue, Zhenwei Ma, Zhilun Gui, *Microstructure Characterization and Properties of Chemically Synthesized Co2Z hexaferrite.* Journal of European Ceramic Society, 2001. **21**: p. 149-153.
8.   J.Jeong, K.W.Cho, D.W.Hahn, B.C.Moon, Y.H.Han, *Synthesis of Co2Z Ba-Ferrites.* Materials Letters, 2005. **59**: p. 3959-3962.
9.   H.Mosallasaei, K.Sarabandi., *Magneto-Dielectrics in Electromagnetics: Concept and Applications.* IEEE Transactions on Antennas and Propagation, 2004. **52**(6): p. 1558-1567.
10.   Yukio Takada, Takashi Nakagawa, Yasunari Fukuta, Masatoshi Tokunaga, Takao A. Yamamoto, Takeshi Tachibana, Shinji Kawano, Naoki Igawa, Yoshinobu Ishi, *Temperature Dependence of Magnetic Moment Orientation in Co2Z-Type Hexaferrite Estimated by High-Temperature Neutron Diffraction.* Japanese Journal of Applied Physics, 2005. **44**(5A): p. 3151-3156.
11.   Yukio Takada, Takashi Nakagawa, Yasunari Fukuta, Masatoshi Tokunaga, Takao A. Yamamoto, Takeshi Tachibana, Shinji Kawano, Naoki Igawa, Yoshinobu Ishi, *Crystal and Magnetic Structures and Their Temperature Dependence of Co2Z-type Hexaferrite (Ba,Sr)3Co2Fe24O41 by High-Temperature Neutron Diffraction.* Journal of Applied Physics, 2006. **100**: p. 043904.
12.   Takeshi Tachibana, Takashi Nakagawa, Yukio Takada, Takeshi Shimada, Takeo A. Yamamoto, K. Izumi, S.Kawano, *X-ray and Neutron Diffraction Studies on Iron-Substituted Z-tyep Hexagonal Barium Ferrite: Ba3Co2-xFe24+xO41 (x = 0-0.6).* Journal of Magnetism and Magnetic Materials, 2003. **262**: p. 248-257.
13.   G.A.Jones, M.Toy, J.G.Booth, C.E.Turner, *Domain Structure Studies of the Single Crystal Magnetic Oxide Ba3Co2Fe24O41 (Co2Z).* Journal of Magnetism and Magnetic Materials, 1994. **131**: p. 29-36.
14.   J.Kulikowski, J.Masiulanis, *Some Peruliarities of the Process of Co2Z Ferroxplana Formation.* Journal of Magnetism and Magnetic Materials, 1980. **19**: p. 109-111.
15.   J.Temuujin, M.Aoyama, M.Senna, T.Masuko, C.Ando, H.Kishi, V.Sepelak, K.D.Becker, *Preparation and Properties of Ferromagnetic Z-type Hexaferrite from*

Wet Milled Mixtures of Intermediates. Journal of Magnetism and Magnetic Materials, 2007. **311**: p. 724-731.

16. D.W.Hahn, Y.H.Han, *Co2Z Type Hexagonal Ferrites Prepared by Sol-gel Method.* Materials Chemistry and Physics, 2006. **95**: p. 248-251.

17. Takeshi Tachibana, Takashi Nakagawa, Yukio Takada, Takeshi Shimada, Takeo A. Yamamoto, *Influence of Ion Substitution on the Magnetic Structure and Permeability of Z-type Hexagonal Ba-Ferrites: Ba3Co2-xFe24+x-yCryO41.* Journal of Magnetism and Magnetic Materials, 2004. **284**: p. 369-375.

18. R.O.Savage, A.Tauber, *Growth and Properties of Single Crystals of Hexagonal Ferrites.* Journal of American Ceramics Society, 1964. **74**(1): p. 13-19.

19. S.Kracunovska, J.Topfer, *On the Thermal Stability of Co2Z Hexagonal Ferrites for Low-temperature Ceramic Cofiring Technologies.* Journal of Magnetism and Magnetic Materials, 2008. **320**: p. 1370-1376.

20. D.W.Kingery, ed. *Introduction to Ceramics.* 1970, John Wiley&Sons. 1-100.

21. Hongguo Zhang, Longtu Li, Ji Zhou, Zhenxing Yue, Pinggui Wu, Zhilun Gui, *Synthesis of Co2Z Hexagonal Ferrite with Planar Structure by gel Self-Propagating Method.* Materials Letters, 2000. **43**: p. 62-65.

22. Y.Mizuno, S.Taruka, K.Kitajima, *Low-temperature Sintering of Z-type Hexagonal Ferrite by Addition of Fluorine Containing Glass Powder.* Journal of Materials Science, 2005. **40**: p. 165-170.

23. I.Orlov, L.Palatinus, A.Arakcheeva, G.Chapuis, *Hexagonal ferrites: a unified model of the (TS)nT series in superspace.* Acta Crystallographica Section B, 2007. **B63**: p. 703-712.

24. H.P.J.Wijin, ed. *Group III Condensed Matter.* Landolt-Bornstein - Group III Condensed Matter, ed. A.M.H. K.H.Hellwege. Vol. 4b. 2006, Springer-Verlag. Chapter 7, 614-616.

Chapter 6

Isotropic Ceramics - Polymer Composites

6.1. Introduction

As mentioned in the Introduction section of Chapter 4, a simple dielectric is not an optimal candidate to minimize antenna's dimensions. The presence of only dielectric property of this type of materials does not provide the similarity of refractive index of material to its surrounding medium. Specialists in Electrical Engineering overcome this challenge by varying the thickness of material applied on top of the antenna [1]. However, this method is still not an optimal solution as it accumulates more materials to compensate this refraction index mismatch, which in turn reduces the performance of the antenna. We will not focus in interpreting this method in detail because it is beyond the scope of this research.

From this point of view, materials to have both dielectric permittivity and magnetic permeability would be more beneficial to overcome or at least mitigate the difference of refractive index between material and its surrounding medium. Ferrite is a material which meets this requirement and its refractive index is given in the form of n=$\sqrt{\mu/\varepsilon}$. If its permittivity and permeability are equivalent to each other, then its refractive index becomes equal or comparable to that of air. There will not any incompatibility

between the device and its surrounding medium so that the incident electromagnetic wave is fully absorbed and retained inside the materials. The performance of the antenna can be retained with the reduction of its size into a minimum dimension [2].

This theory of using equivalent permittivity and permeability has been verified with applications at low frequency ranges less than 5 MHz, where ferrites with high permeability and low permittivity are available. This phenomenon will also be illustrated in later chapters of this dissertation. However, it is challenging for applications at microwave frequencies from 300 MHz and beyond, because most conventional ferrites such as spinel and garnet lose their permeability in this frequency range. As a result, there has not been much research on formulation of materials to achieve the compatibility of refractive index of material and its surrounding medium for microwave frequencies. Given the increasing demand for a small, portable and high performance antenna at microwave working utilities, as well as the appearance of special type of ferrite $Ba_3Co_2Fe_{24}O_{41}$ (Co_2Z), interest on formulating material to have equal permittivity and permeability at microwave frequencies has risen.

In this chapter, we will describe our research to formulate the material for an antenna which works in the high frequency range, which is at least 300 MHz. It is not available a single material to have comparable permeability and permittivity. Furthermore, materials used in the antenna usually are required to possess other properties such as flexibility or plasticity. As a result, the final material is a composite formulated by a ceramic powder and a polymer. In our research, Co_2Z powder was combined with several polymers to formulate equivalent permittivity and

permeability materials whose magnitude being expected to be controlled by varying ferrite compositions.

As described in Chapter 5, Section 5.3-5.4, Co_2Z is one of the complex ferrites, in the same group with $Ba_2Co_2Fe_{12}O_{22}$ (Co_2Y) and $BaFe_{12}O_{19}$ (BaM). All of these retain their high magnetic property at very high frequencies. Data provided by Trans-Tech showed that this material can work up to a frequency of 1 GHz as seen in Fig. 5.1 and Fig. 5.2. Note that those values are of highly ordered materials. Other researches stated that Co_2Z retains its property up to a frequency of 1.5 GHz [3-6]. However, magnetic permeability of this material was only in order of 3 to 4, which was a consequence from synthesis technique. Therefore, Co_2Z from Trans-Tech was applied for this research. Parameters of this ferrite were given in Table 6.1 and its crystalline phases were indicated in XRD pattern in Fig. 6.3. Since the synthesis of Co_2Z is a multiple step solid solution sintering process, it always includes some portions of impurities, which are either initial oxides or intermediate compounds.

Given the requirement of our partner at Department of Electrical Engineering, Ohio State University (OSU), to produce either a flexible moldable or castable material, there are two classes of matrix materials that can meet this demand. The first is polyethylene (PE), a thermoplastic material that will solidify after being melted, but not degrade if heated below its decomposition temperature. This constituent is appropriate to form a flexible castable material. The second material is a silicone based elastomer, which is a liquid that solidifies as a result of a hardening process. Depending upon the nature of initial raw materials, the byproduct of this polymerization is water, small organic compounds like acetic acid, or nothing [7].

Silicone elastomer solidifies to form a flexible shape which fits the needs of producing irregularly shaped devices. Both PE and silicone elastomer contain small dielectric permittivity and magnetic permeability and low dissipation factor.

In this chapter, we will describe the formulation and properties of Co_2Z-PE isotropic composite with Co_2Z fraction up to 45 vol%. Details of the Co_2Z-silicone composite will be described in Chapter 7 because it relates to a different experimental technique.

6.2. Experiments

6.2.1. Ceramics preparation

Co_2Z provided from the Trans-Tech Inc. had very large particle size distribution as being seen in Table 6.2. Its average particle size diameter obtained from our measurement was 27 μm and the diameter at 90 vol% was 45 μm. At this large particle size, the dielectric permittivity and magnetic permeability were retained [8] to its initial magnitudes. However, they were not beneficial to our research's aim of producing an evenly distributed polymer matrix composite. Co_2Z's particles are in irregular shape and porous. The presence of voids can be observed from its microstructural images in Fig. 6.4a and 6.4b. When mixed with polymers in the liquid state, the high molecular weight, steric hindrance and high viscosity of polymers will prevent polymers from penetrating into the voids and completely expelling adsorbed air bubbles on the walls of the voids. The presence of air with permittivity and permeability equal to 1 will decrease the overall values of formulated materials. Zach

Wing [9] used the combination of air and dielectrics in his effort to reduce the dielectric permittivity of materials for applications at microwave frequencies.

Co_2Z was ball milled in a polyethylene jar, using iso-propanol as the milling medium and alumina media for about 7 days. The average particle size at 50 vol% reduced to 3.4 μm and at 90 vol% to 6 μm as being given in Table 6.3 and depicted in Fig. 6.5. The microstructural observation showed well separated particles (Fig. 6.6) without void captured inside them. Co_2Z particles were still in irregular shapes.

6.2.2. Mixing procedure

Low Density PolyEthylene (LDPE) (sigma-alpha, Melt Index = 25g/10 min) was used as the matrix material in which Co_2Z was distributed. The properties of this LDPE are given in Table 6.4. The dielectric permittivity of LDPE is 2.8 with a dissipation factor is 10^{-3}; magnetic permeability equals to 1. The melting point of LDPE provided by the manufacturer was 121^oC.

Co_2Z-LDPE mixtures were prepared with 10 to 45 vol% Co_2Z powder. Co_2Z powder was dispersed into the PE matrix using a Brabender Plasti-Corder PL2100 at 130^oC, and rotating speed 50 rpm. Two thirds of the PE was added into the operating heated chamber of the hot mixer to produce a dispersion medium. Small amounts of Co_2Z were gradually added into the melted PE with careful observation for the variation of torque value, shearing stress produced on surface of blades. Heavy mineral oil was added into mixtures continually as a lubricant with the aim to facilitate the dispersion of powder in PE [10]. The remaining PE was added into the mixer when two third

volume of powder was used. The mixer was kept running for at least 15 minutes after all the Co_2Z powder was added. The mixing step completed when the torque had stabilized. The mixture of Co_2Z-LDPE was pushed out of the mixing chamber by reversing the blade's rotation and cut into small pieces while still hot before being used for the shape formation.

Samples for dielectric permittivity and magnetic permeability measurements were made by warm molding. A specific die with diameter of 20 mm, plunger and support heights was made to shape samples. The error of the measurement was less than 10%. Samples were heated up to 130^oC inside the die by the use of a controllable hot plate. During melting, they were pressed under a mechanical pressure of 390 MPa for 10 minutes, using a mechanical hydraulic press. The schematic illustration of this experimental procedure is depicted in Fig. 6.7. The molded samples had brown color as the result of the combination of red black color of Co_2Z powder and colorless PE as being seen in Fig. 6.8. The measurement data at 300 MHz of all samples containing Co_2Z from 10 vol% to 45 vol% were collected to investigate the influence of sample's compositions on its permittivity and permeability. Those data were compared with theoretical calculations using theoretical models.

6.2.3. Theoretical calculations

The Co_2Z-LDPE composites were considered as particulate composites, in which the Co_2Z particles were evenly distributed in the PE polymer matrix. Theoretical calculations of dielectric permittivity and magnetic permeability applied the same

principle. The variation of permittivity and permeability along with ceramic concentration has been assumed to follow the simple rule of mixture (Eq. 6.1), in which ceramics particles are considered isotropic and non interactive with each other.

Parallel :
$$\varepsilon_{eff} = \frac{\varepsilon_1'.\vartheta_1 + \varepsilon_2'\vartheta_2}{\vartheta_1 + \vartheta_2}$$
(Eq. 6.1)

Perpendicular:
$$\frac{1}{\varepsilon_{eff}} = \frac{\vartheta_1}{\varepsilon_1} + \frac{\vartheta_2}{\varepsilon_2}$$

Where ε_{eff}, ε'_1, ε'_2 are dielectric permittivity of composite, inclusion, and medium correspondingly; υ_1 and υ_2 are volume percent of inclusion and medium.

The more accepted version of this simple rule was derived by Clausius and Mossotti[11]:

$$\frac{\varepsilon_{eff}}{\varepsilon_2} = 1 + 3\vartheta.X_d$$
(Eq. 6.2)

Where ϑ is the inclusions volume and $X_d = \frac{(\varepsilon_1 - \varepsilon_2)}{(\varepsilon_1 + 2\varepsilon_2)}$

This method was found not very consistent with majority of experimental data of various material systems because particle shape is usually much more complex, not simply round with a smooth surface. Furthermore, the assumption of non interaction among particles is true only in very dilute specimens [11], in the range of few volume percent which would lead to a large difference between theoretical and measured values [12] if it is applied for a medium or high concentration solution.

Rayleigh developed another equation for diluted dispersions in which the inclusions volume is small, from 1 to 3 vol%. This satisfies the condition of non-interactiing between dielectric particles.

$$\frac{(\varepsilon_{eff}-\varepsilon_2)}{(\varepsilon_{eff}+2.\varepsilon_2)} = \frac{\vartheta(\varepsilon_1-\varepsilon_2)}{(\varepsilon_1+2.\varepsilon_2)} \qquad \text{(Eq. 6.3)}$$

Bruggeman applied this approach to develop a new model for higher inclusions volume loading and published the so called one-third power equation as followed:

$$\left(\frac{\varepsilon_2}{\varepsilon_{eff}}\right)^{1/3} . \frac{(\varepsilon_1-\varepsilon_{eff})}{(\varepsilon_1-\varepsilon_2)} = (1-\vartheta) \qquad \text{(Eq. 6.4)}$$

At high concentration, Botcher derived a formula in the form:

$$\frac{(\varepsilon_{eff}-\varepsilon_2)}{\varepsilon_{eff}} = \frac{3\vartheta(\varepsilon_1-\varepsilon_2)}{(\varepsilon_1+2.\varepsilon_{eff})} \qquad \text{(Eq. 6.5)}$$

Fricke included shape parameter into his calculations. He considered all particles have spheroidal geometry for that, the formula deducted has a complete form either of dielectric permittivity, inclusions volume percent or the shape-factor x'. However, for most of the case, the shapes of dielectric particle are more or less rounded with spherical geometry, so the formula of Fricke has not been widely applied.

Looyenga considered the case of system in which the dielectric permittivity of components is not very different from each other. His equation was written on the basis of Rayleigh's equation as:

$$\varepsilon_{eff} = \{\varepsilon_2^{1/3} + \vartheta(\varepsilon_1^{1/3} - \varepsilon_2^{1/3})\}^3 \qquad \text{(Eq. 6.6)}$$

The Brugemann model was found to fit with a number of material systems in which air-ceramics composites in the research of Zach Wing [9] was one example. He made high dielectric permittivity ceramics TiO_2 and air composites by burning off carbon black after producing TiO_2-C mixtures. The dielectric permittivity of Titania (TiO_2) is higher than 100 while that of air is 1. This model was also found valid for high and low permittivity components containing composites in which MnZn-silicone systems in research of D.Y. Kim et al [13] are one example. Magnetic permeability of MnZn ferrite was 300 while that of silicone was 2.8.

L.F.Chen et al. [14] emphasized that Rayleigh's equation (Eq. 6.3) was in good agreement with isotropic $BaTiO_3$-PVDF composites but it provided values two times lower than that from experiment when $BaTiO_3$ was in whisker form.

In 1993, Jayasundere and Smith [12] further developed Kerner's equation:

$$\varepsilon_c = \frac{\varepsilon_1.\vartheta_1 + \varepsilon_2.\vartheta_2 \left(E_{2z}/E_{1Z} \right)}{\vartheta_1 + \vartheta_2 \left(E_{2z}/E_{1z} \right)} \qquad \text{(Eq. 6.7)}$$

Where ε_c, ε_1, ε_2 are the dielectric permittivities of composite, matrix and inclusions, correspondingly. E_{1z} and E_{2z} are the average electric fields in the matrix and inclusion along z direction. They applied a finite element model for two spheres having the same radius, according to the relationship between polarization P, dipole moment m and surface energy σ to derive the final expression of ε_c to ε_1 and ε_2.

$$\varepsilon = \frac{\varepsilon_1.\vartheta_1 + \varepsilon_2.\vartheta_2 \left[3\frac{\varepsilon_1}{(\varepsilon_2+2\varepsilon_1)} \right]\left[1+3\vartheta_2 \left(\frac{\varepsilon_2-\varepsilon_1}{\varepsilon_2+2\varepsilon_1} \right) \right]}{\vartheta_1 + \vartheta_2 \left(\frac{3\varepsilon_1}{\varepsilon_2+2\varepsilon_1} \right)\left[1+3\vartheta_2 \left(\frac{\varepsilon_2-\varepsilon_1}{\varepsilon_2+2\varepsilon_1} \right) \right]} \qquad \text{(Eq. 6.8)}$$

Carpi F. and Rossi D. D. [15] and Anjana P.S. et al. [16] applied and compared a series of simulation methods for their composites systems, in which Jayasandre-Smith equation was introduced. In their research, they investigated Titania-rubber systems in which the dielectric permittivity of rubber was 12, close to that of composite was 8. Their diluted materials systems contain TiO_2 compositions from 5.1 to 9.7 vol%. The calculation from Jayasandre-Smith model gave closest prediction to the measurement value. Anjana et al. studied on $ZnAl_2O_4$-TiO_2/PTFE [17] materials whose components' dielectric permittivity was 12 and that of PTFE was 2.1. The inclusions were used in the range from 10 to 60 volume percent. Prediction using Jayasandre-Smith equation showed results that were very consistent with those measured as being seen in Fig. 6.11. Jayasundere-Smith model was used to calculate the theoretical values of dielectric and magnetic constants of composites produced.

6.3. Results and discussions

From the experimental procedure, the isotropic samples of Co_2Z-LDPE were formed and used to evaluate the dielectric permittivity, magnetic permeability and their derived loss tangents. In this part, we will describe results and their consistencies with theoretical calculations.

6.3.1. Measurement data

The permittivity and permeability of samples were measured by the impedance contacting method, using Agilent E4991A equipment that is able to operate in the range from 1 MHz to 3 GHz. For the dielectric permittivity measurements, samples

were put into the sample chamber of test fixture 16453A. This fixture consists of two electrode surfaces which the lower one has smaller surface which was used as one parameter for the calculation. The upper electrode was supported by a spring to produce pressure on top electrode. This design was very efficient in minimizing the air gap between the surfaces of electrodes and sample. The principle of this method is to measure the capacitance of the material from which to derive values of real relative permittivity and its imaginary value.

The dielectric material is considered as a capacitor that under alternating electric field, acts as a circuit with a capacitor and a resistor arranged in parallel. The complex admittance of circuit is expressed as:

$$Y^* = G + j\omega C_p = j\omega \left(\frac{C_p}{C_0} - j \frac{G}{\omega C_0} \right) C_0 \qquad \text{(Eq. 6.9)}$$

Where C_p is the capacitance of capacitor, C_o is the capacitance of free space and G is the reciprocal of resistance of resistor ($1/R_p$). The complex relative permittivity (ε_r^*) and its real (ε_r') and imaginary (ε_r'') components of a dielectric material are derived as:

$$\varepsilon_r^* = \left(\frac{C_p}{C_0} - j \frac{G}{\omega C_0} \right) \qquad \text{(Eq.6.10)}$$

$$\varepsilon_r' = \frac{C_p}{C_0} = \frac{t.C_p}{S.\varepsilon_0} \qquad \text{(Eq.6.11)}$$

$$\varepsilon_r'' = \frac{G}{\omega C_0} = \frac{t}{\omega.\varepsilon_0.S.R_p} \qquad \text{(Eq.6.12)}$$

Applying pressure significantly reduces the measurement errors by maintaining contact between ramp surface and specimen's surface. We duplicated our measurements several times to make sure that the error of the measurement was in the

acceptable range. Fig. 6.9 depicts permittivity of specimen containing 45 vol% Co_2Z varying along with measuring frequency. The resonance happened at frequency beyond 1 GHz region was due to the magnetic loss of Co_2Z.

Similarly to the permittivity measurement, the permeability measurement was conducted by using permeability test fixture Agilent 1645A. In this case, the material was considered as a circuit containing one resistor and an inductor. The complex impedance of the circuit is expressed as follows:

$$Z^* = R_s + j\omega L_s = j\omega(\frac{R_s}{j\omega} + L_s) \qquad \text{(Eq. 6.13)}$$

$$\mu^* = \frac{Z_m^* - Z_{sm}^*}{j.\omega\mu_0} \frac{2\pi}{h.ln\frac{c}{b}} + 1 \qquad \text{(Eq. 6.14)}$$

Where μ^*: relative permeability

Z_m^*: measured impedance with toroidal core

Z_{sm}^*: measured impedance without toroidal core

μ_0: permeability of free space

h: height of material under test

c, b: outer and inner diameters of material under test

Values of Z_m^* and Z_{sm}^* are included in this calculation to compensate for the loss from the remaining impedance after the material is exposed to the magnetic field.

For the permeability measurement, the sample's dimensions are significant. Experimental data was also given in Table 6.5 and depicted in Fig. 6.12.

6.3.2. Discussion

Our primary investigation showed that most of models described in 6.2.3 do not correctly represent our measured data. Fig. 6.10 which shows the calculated values using Bruggeman equation in comparison with our measured ones is one example. In this case, it is reasonable because Bruggeman built his equation for dielectrics composite systems in which the magnitudes of both dielectric permittivity and magnetic permeability of components [11] far from each other or from that of formulated composites. Meanwhile, the permittivity of Co_2Z and LDPE was 12 and 2.8; correspondingly, those were very close to that of the composite, especially at low volume composition samples such as 10 or 20 vol%.

Models of Rayleigh, Botcher, and Looyenga also assumed a big difference between permittivity of fillers and matrix which is not applicable to our material system. Furthermore, other factors of high Co_2Z volume fractions together with its irregular shape would violate their simulation conditions in which inclusions should have spherical shape and inert to each other.

As shown in Fig. 6.11, the dielectric permittivity of produced composites was almost stable in the frequency range lower than 400 MHz and slightly increased to their resonance frequency of 1 GHz. Under the request of our project partner, Ohio State University, we investigated properties of materials at the frequency of 300 MHz. Comparisons of magnitude of relative permittivity and permeability as a function of composition was depicted on Fig. 6.13 and Fig. 6.14. Dielectric permittivity was always larger than magnetic permeability. Since the original values of Co_2Z (ε'=12,

μ'=8) are not very different, its mixing with PE strongly affected the overall magnitude of formulated composites. The low permeability of PE (equals to 1) also contributed into bringing the magnitude of permeability of the composite further lower than its value of permittivity.

The difference of permittivity and permeability of the Co_2Z-LDPE composites established a boundary as depicted on Fig. 6.14. The shape of this ε'-μ' curve showed that by using isotropic Co_2Z-PE, permittivity increased faster than permeability along the filler volume percentage. The shortest gap between these two parameters is within 20 vol% of Co_2Z. The curve established an unreachable region, which unfortunately was the region we want to approach.

Though the target of obtaining equivalent dielectric permittivity and magnetic permeability was not met by formulating an isotropic material, its test result on real antenna showed an encouraging outcome. Blocks of the isotropic Co_2Z-LDPE with dimensions of 3×3×1 inches were made for the test conducted at OSU. Their image is given in Fig. 6.8. The test result was depicted in Fig. 6.15 together with that of a bare metallic spiral antenna, and that of the simulation. Consistent with theoretical assumptions, the presence of both dielectric and magnetic properties of Co_2Z had a positive contribution into the performance of antenna at smaller dimensions. It has been well known that the dimension of an antenna should be proportional to reversal of the frequency of the incident electromagnetic wave to obtain the maximum performance. For conventional antenna, in order for an antenna to work at a low frequency, its dimension needs to be big and vice versa. In this case, the application of our material kept the antenna achieved the same gain at a low frequency range

without the need to increase the antenna's dimension. Nevertheless, there was still a big gap between our material and the ideal condition.

The simple mixing methodology can only form an isotropic system whose properties are the combination of those of its components. It is obvious that these properties are isotropic to each direction so that permittivity was always higher than permeability. A textured material is needed to tailor its properties in a way that its magnetic property can surge over the magnitude of its dielectric property. Therefore, we thought of another methodology in which electromagnetic properties of materials will polarize in some ways to give a magnetic permeability equal to dielectric permittivity.

6.4. Summary

In this chapter, we introduced the significance of electromagnetic materials for microwave applications and focused on the formation of isotropic composites in which Co_2Z hexagonal ferrite was evenly distributed in LDPE medium. The target of this work was to investigate the ability of making an equivalent dielectric permittivity and magnetic permeability and flexible material for microwave applications. In term of being able to melt at elevated temperature, PE offered a flexible production method so that the formed materials were castable into complex shapes. However, it's low and uneven dielectric permittivity ($\varepsilon' = 2.8$) and magnetic permeability ($\mu' = 1$) results in low and unequal magnitudes of the magnetodielectric parameters for the formulated composites.

The demand of equal electromagnetic properties was not achievable from the simple mixing. A novel methodology was needed to divide those properties so that they match with each other.
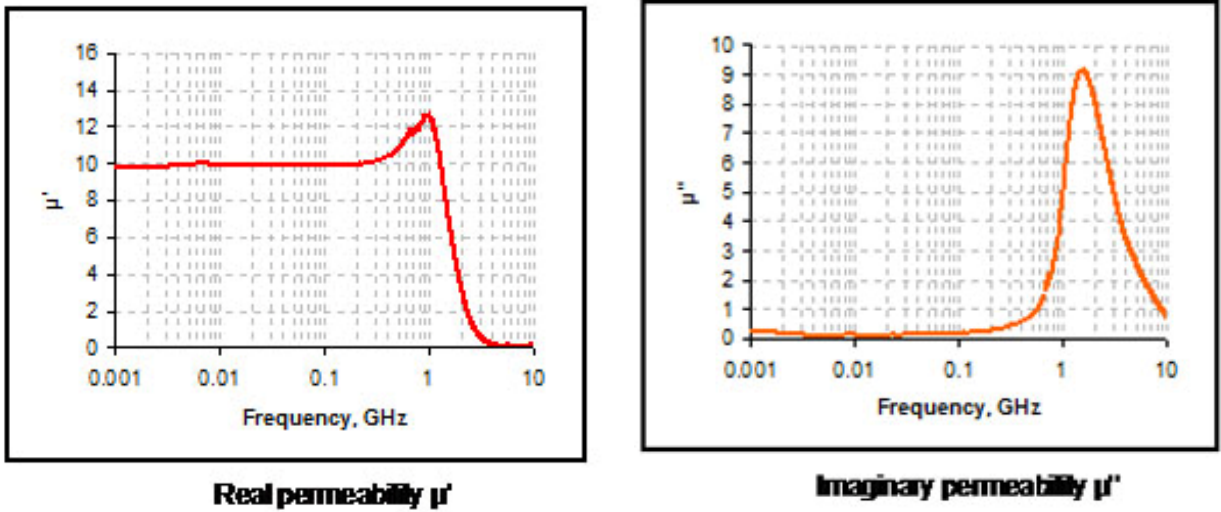
Fig. 6.1: Magnetic constants (permeability) of Co_2Z ($Ba_3Co_2Fe_{24}O_{41}$), provided by Trans-Tech Inc.
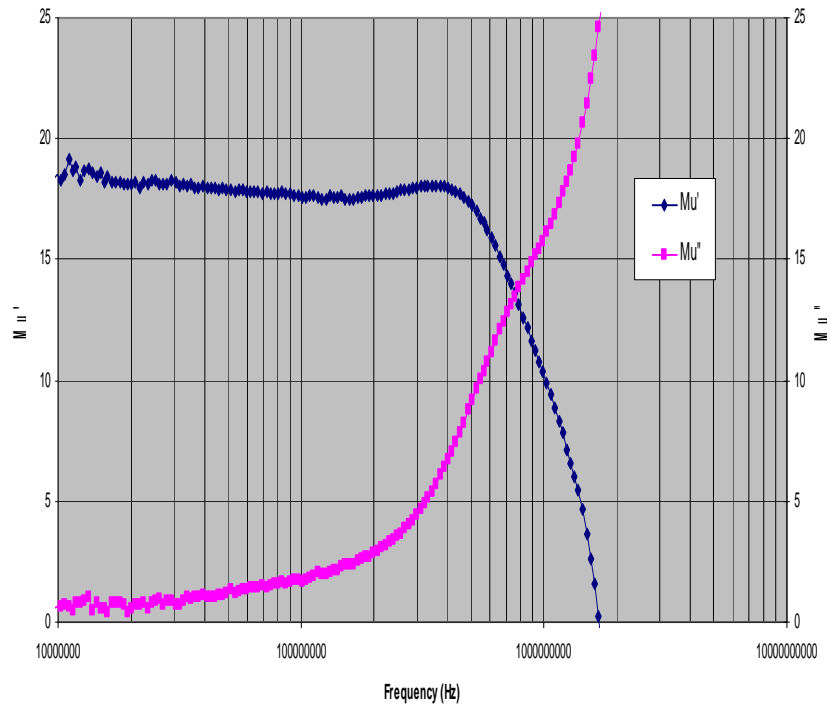
Fig. 6.2: The magnetic permeability and loss component of aligned Co_2Z bulk, provided by Trans-Tech Inc.
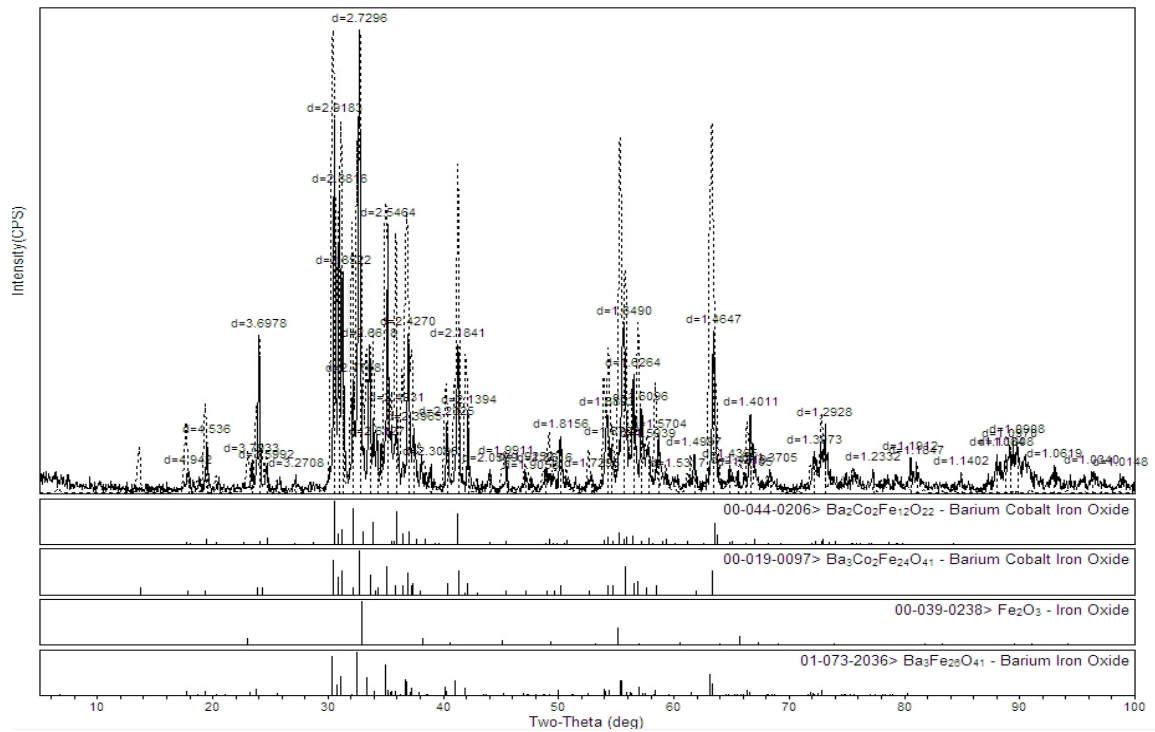
Fig. 6.3: XRD pattern of Co$_2$Z (Ba$_3$Co$_2$Fe$_{24}$O$_{41}$) given by Trans-Tech Inc.

Table 6.1: Parameters of Co$_2$Z (Ba$_3$Co$_2$Fe$_{24}$O$_{41}$) given by Trans-Tech

	Melting point	Density	Purity	Dielectric constant (1 GHz)	Loss tangent (1 GHz)	Magnetic constant (1 GHz)	Loss tangent (1 GHz)
Co$_2$Z	>1500°C	5.35 g/cm^3	99%	12	10^{-3}	10	10^{-3}

Table 6.2: Sieve analysis of Co$_2$Z (Ba$_3$Co$_2$Fe$_{24}$O$_{41}$) given by Trans-Tech

Fraction	+ 100	100-140	140-170	170-200	200-325	>325
Weight %	0.08	33.07	14.72	21.81	28.82	1.51

Table 6.3: Particle size distribution of Co_2Z after 168 hours grinding

PS	0 μm	1.1 μm	1.8 μm	2.5 μm	3.2 μm	3.9 μm	4.6 μm	5.3 μm	6.0 μm
Percentage (%)	0.0	14.3	7.2	9.8	15.5	14.0	10.9	11.2	9.7
Accumulative percentage (%)	0.0	14.3	21.5	31.3	46.8	60.8	71.7	82.9	92.6
PS		6.7 μm	7.4 μm	8.1 μm	8.8 μm				
Percentage (%)		3.9	3.5	0.0	0.0				
Accumulative percentage (%)		92.6	96.5	100.0	100.0				

Table 6.4: Properties of Low Density PolyEthylene (LDPE) given by Sigma-Aldrich [*]

	Melting point	Density	Dielectric constant (1 GHz)	Loss tangent (1 GHz)	Melting index
LDPE	121°C	0.98 g/cm^3	2.8	10^{-3}	25 g/10min

[*] Company was not able to provide information of molecular weight
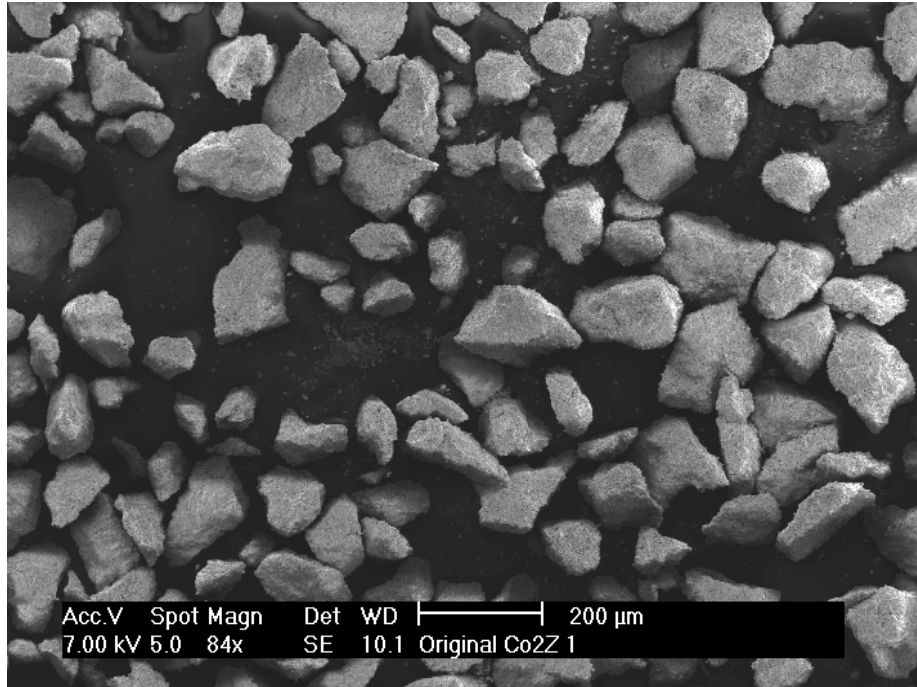
Fig. 6.4a: The large, rough, and irregular shape of Co_2Z particles
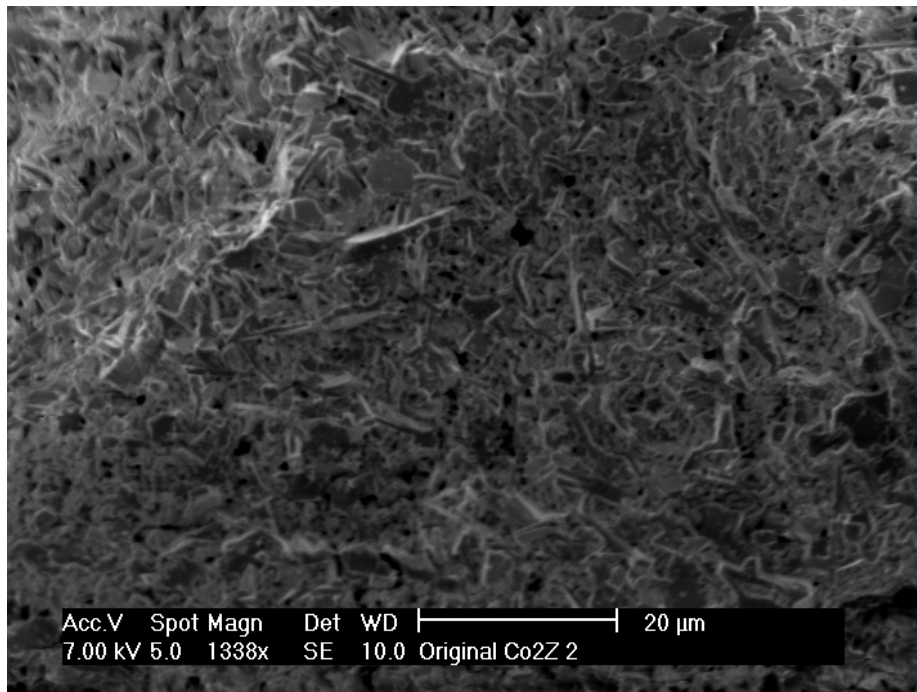
Fig. 6.4b: The presence of voids inside Co_2Z particles
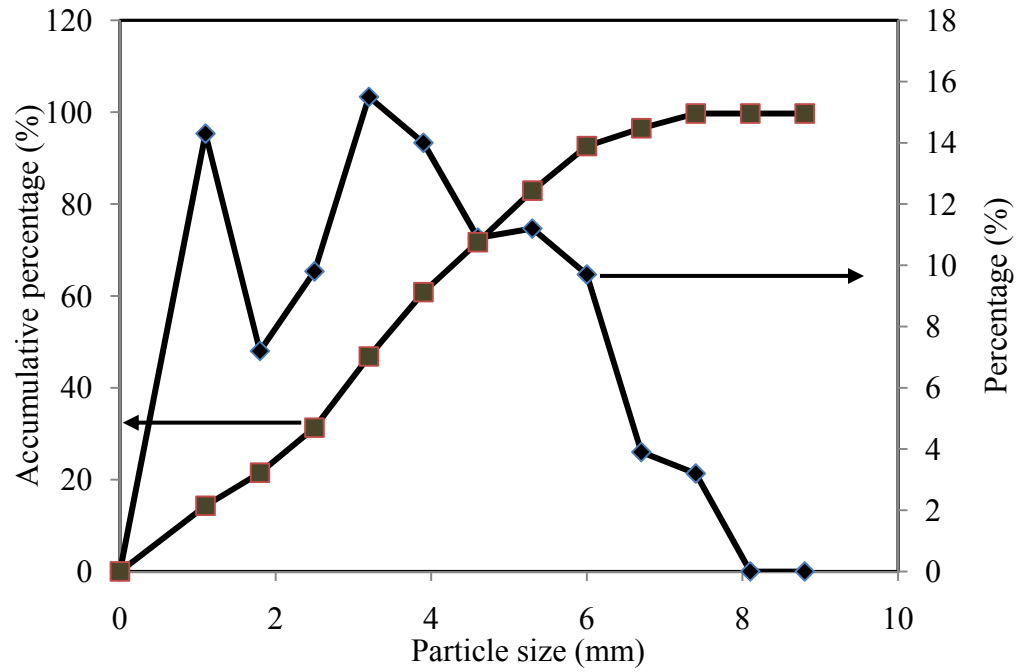
Fig. 6.5: Particle distribution of Co_2Z after 168 hours milling in Isopropanol medium, using alumina media.
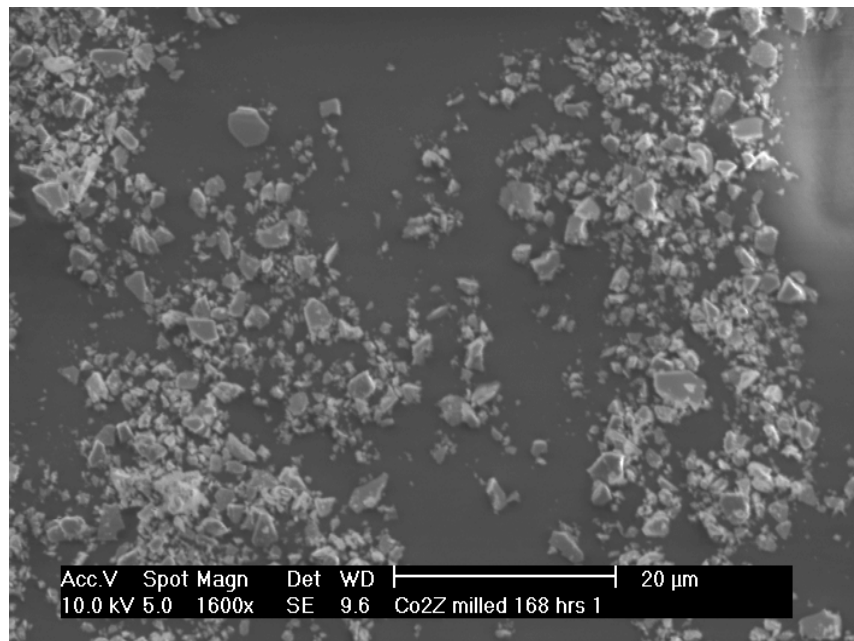
Fig. 6.6: Microstructure of Co_2Z after 168 hours of milling in Isopropanol medium, using alumina media
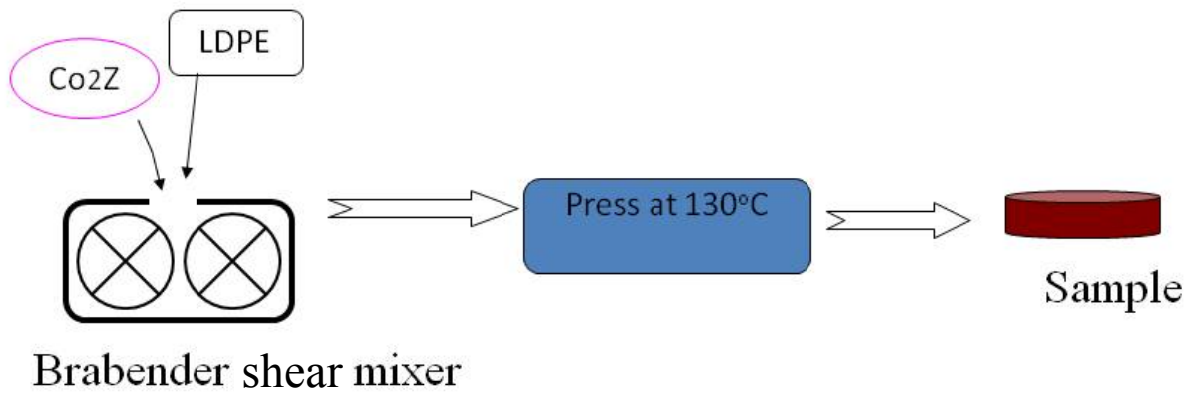
Fig. 6.7: Experimental procedure
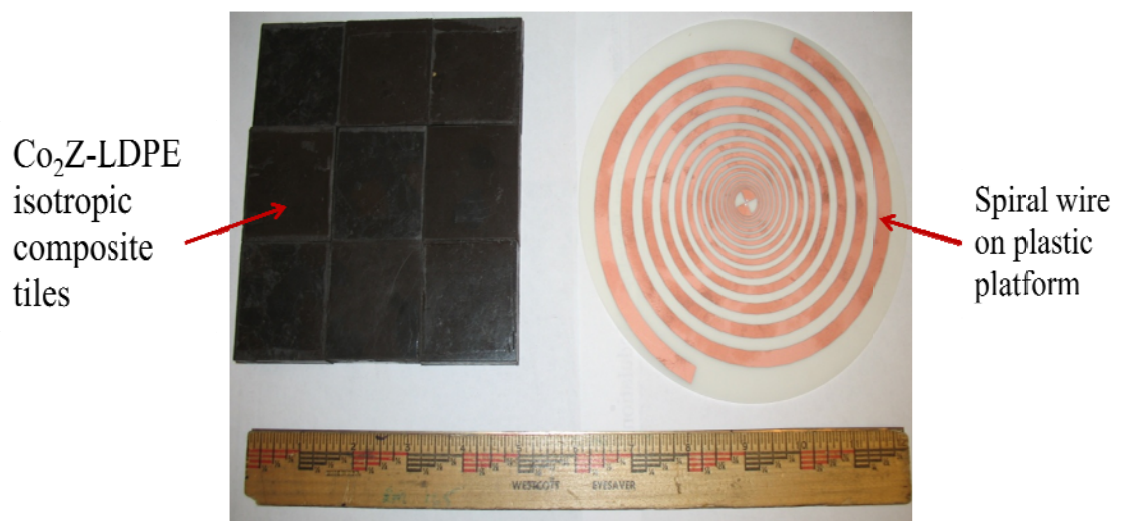
Fig. 6.8: Pieces of Co_2Z-LDPE composites and spiral wire played as an antenna
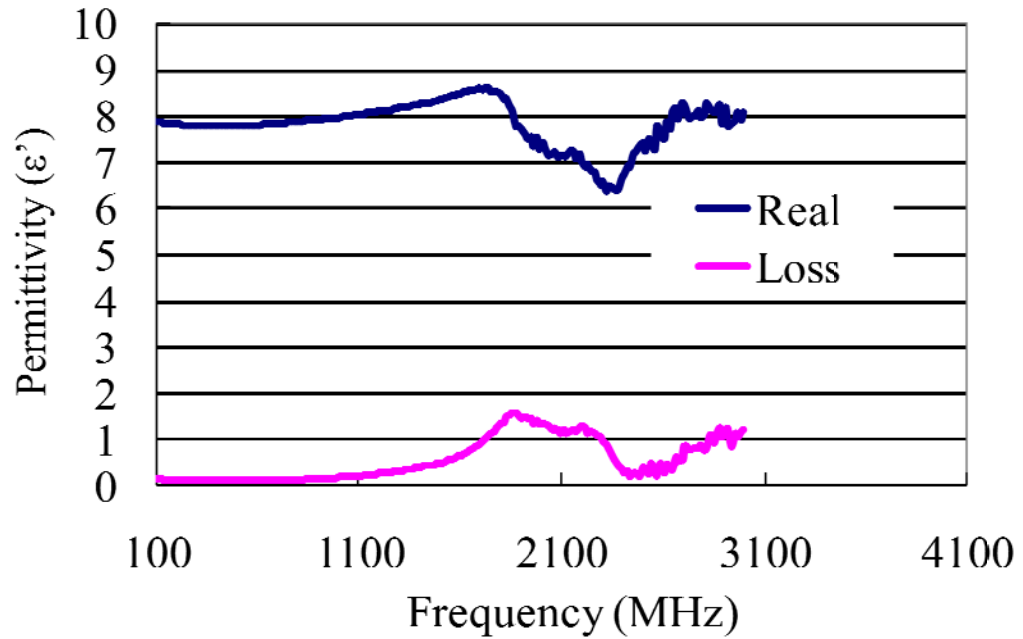
Fig. 6.9: The permittivity of isotropic 45 Vol% Co_2Z-LDPE composites in the range from 100 MHz to 3 GHz. The dispersion after 1 GHz was from magnetic resonance

Table 6.5: Measurement results of permittivity and permeability of Co_2Z-LDPE with a variation of Co_2Z composition

Co_2Z (vol%)	10	20	30	40	45
Permittivity (ε')	3.29 ± 0.3	3.63 ± 0.4	5.09 ± 0.5	6.51 ± 0.6	7.78 ± 0.7
Permeability (μ')	1.47 ± 0.1	1.79 ± 0.2	2.24 ± 0.2	2.95 ± 0.3	3.32 ± 0.3
Brugemann (ε')	3.51	4.31	6.22	7.72	8.311
Brugemann (μ')	1.48	2.06	2.76	3.55	3.98
Jaya-Smith (ε')	3.17	3.98	5.00	6.21	6.97
Jaya-Smith (μ')	1.27	1.67	2.11	2.88	3.26
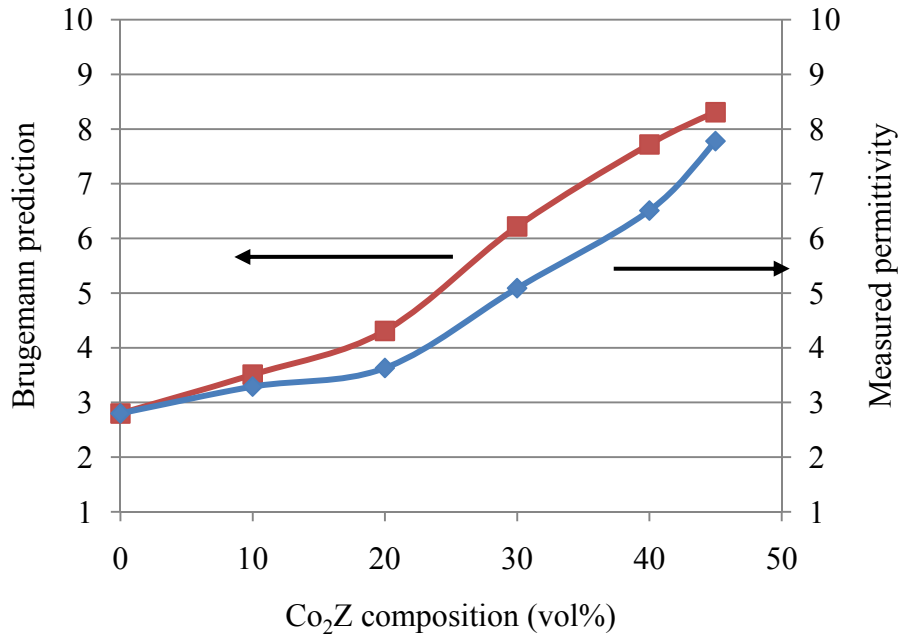
Fig. 6.10: The difference between experimental measurement and Bruggeman prediction
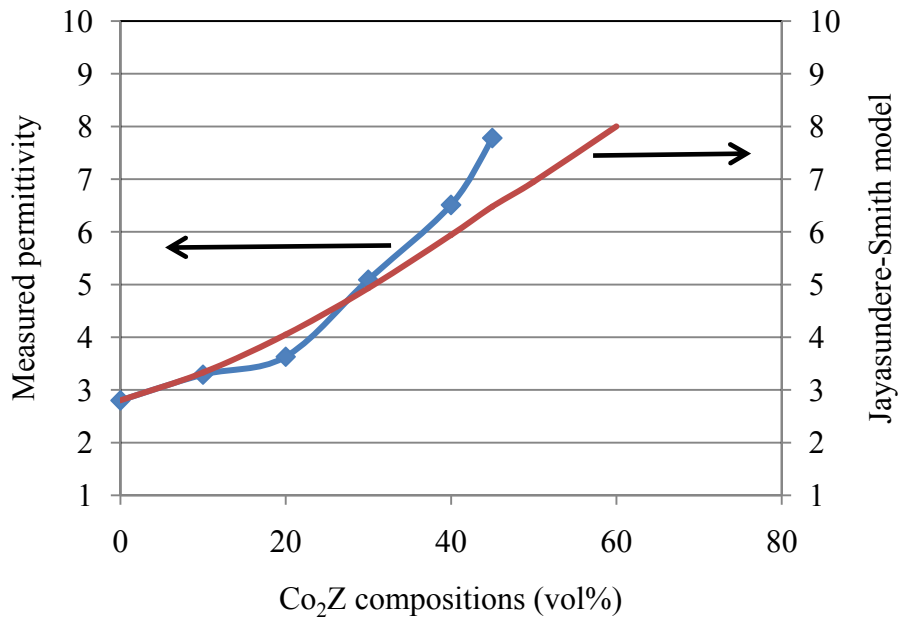
Fig. 6.11: Measured values of permittivity (ε') in comparison with the theoretical Jayasundere - Smith prediction
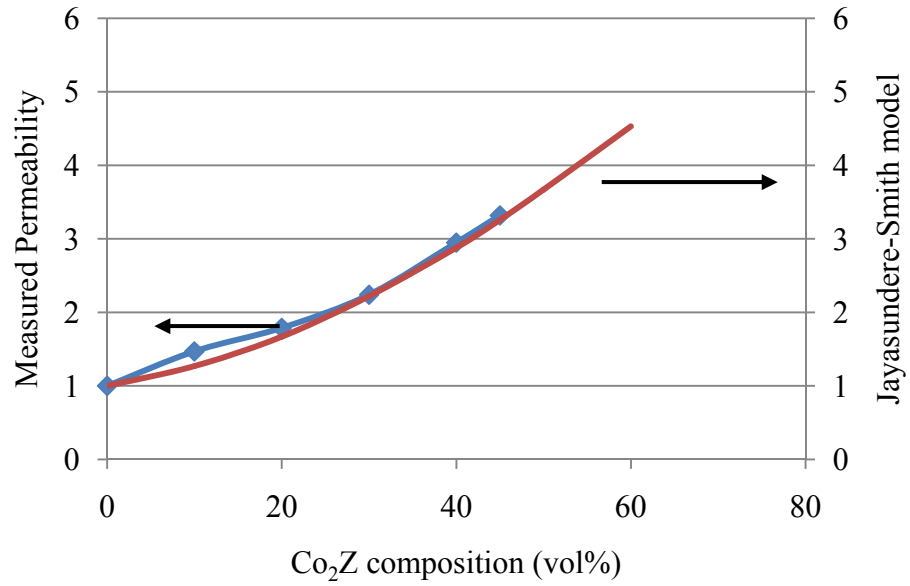
Fig. 6.12: Measured values of permeability (μ') in comparison with the theoretical
Jayasandre - Smith prediction
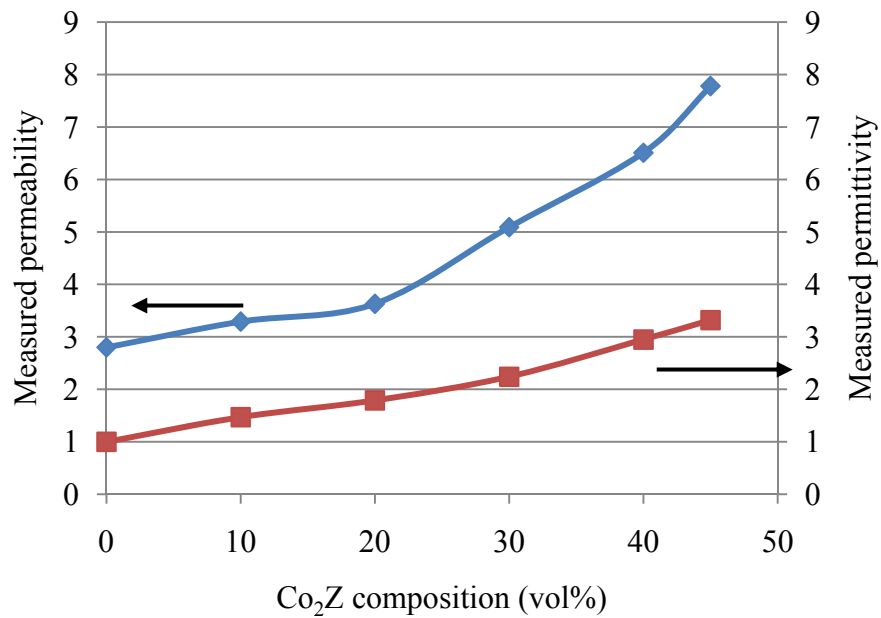
Fig. 6.13: Permittivity and permeability of Co_2Z-LDPE composites with Co_2Z
percentage ranged from 0 to 45 Vol%
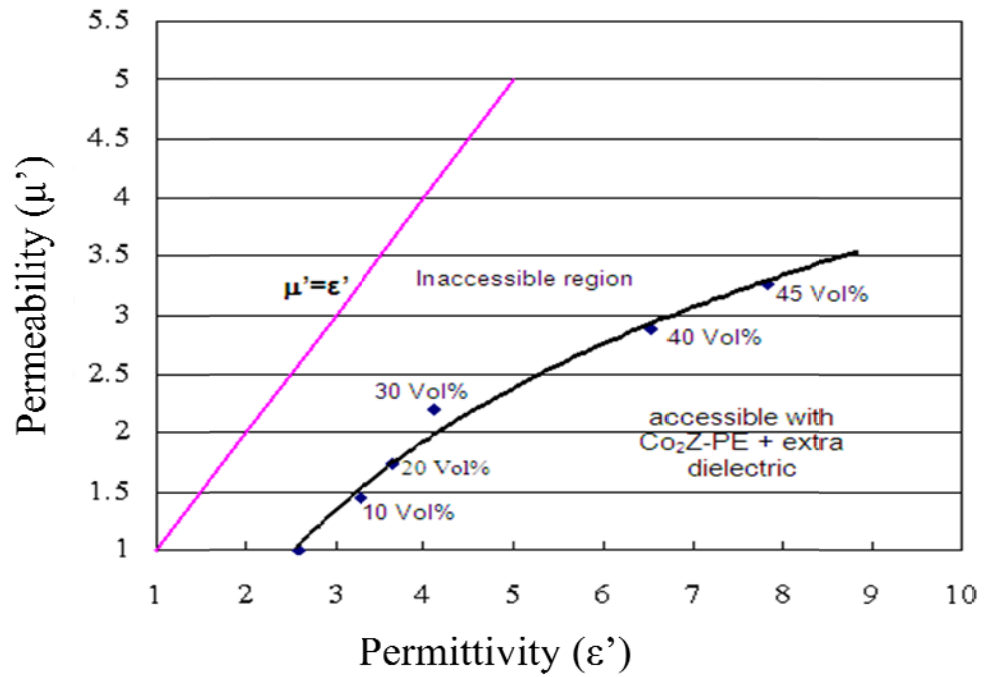
Fig. 6.14: The differentiation of permittivity and permeability values in comparison with those of the requirement
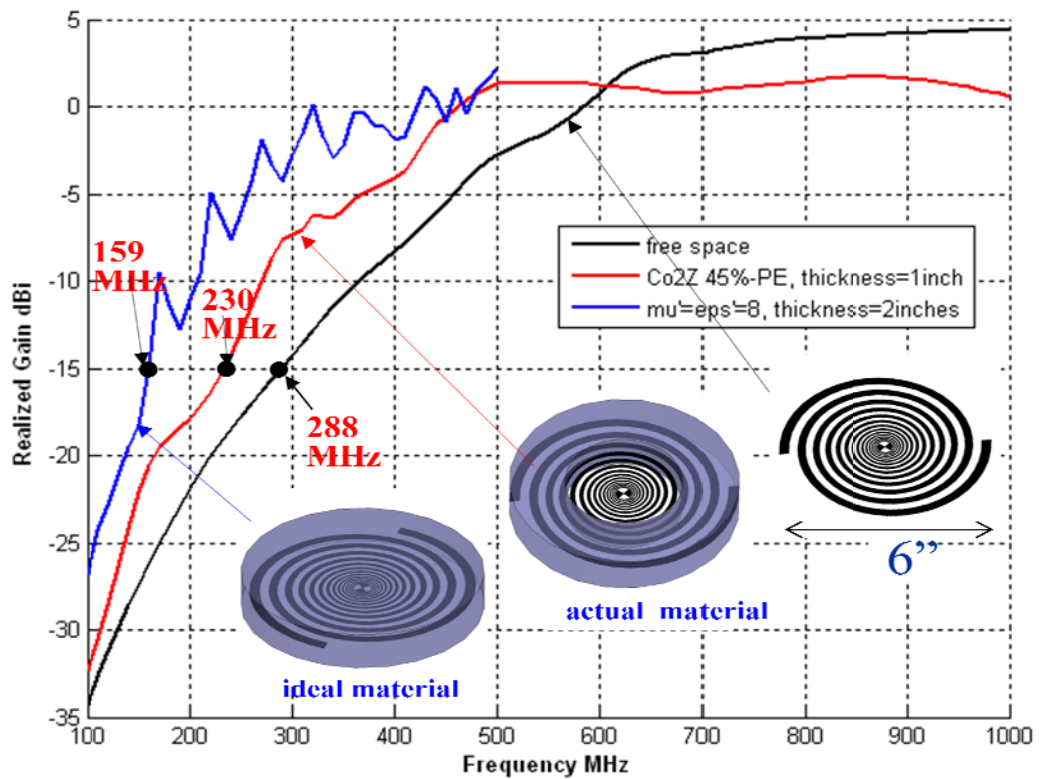
Fig. 6.15: The improvement of antenna using Co_2Z 45 vol% - PE.

References

1. J.S.Colburn, Y.R.Samii, *Patch Antennas on Externally Perforated High Dielectric Constant Substrates.* IEEE Transactions on Antennas and Propagation, 1999. **47**(12): p. 1784-1794.
2. H.M.Musal Jr., D.C.Smith, *Universal Design Chart for Specular Absorbers.* IEEE Transactions on Magnetics, 1990. **26**(5): p. 1462-1464.
3. D.W.Hahn, Y.H.Han, *Co2Z Type Hexagonal Ferrites Prepared by Sol-gel Method.* Materials Chemistry and Physics, 2006. **95**: p. 248-251.
4. H.I. Hsiang, H.H. Duh, *Effects of Glass Addition on Sintering and Magnetic Properties of 3BaO.0.5Sr0.5O2CoOFe2O3 for High Frequency Applications.* Journal of Materials Science, 2001. **36**: p. 6.
5. C.Jacquiod, D.Autissier, *Rare-earth Substitutions in Z-type Hexaferrites.* Journal of Magnetism and Magnetic Materials, 1992. **104-107**: p. 419-420.
6. Hongguo Zhang, Longtu Li, Ji Zhou, Zhenxing Yue, Pinggui Wu, Zhilun Gui, *Synthesis of Co2Z Hexagonal Ferrite with Planar Structure by gel Self-Propagating Method.* Materials Letters, 2000. **43**: p. 62-65.
7. H.C.Hillborg, *Loss and Recovery of Hydrophobicity of Polydimethylsiloxane After Exposure to Electrical Discharges*, in *Department of Polymer Technology*. 2001, Royal Institute of Technology: Stockholm. p. 77.
8. Hongguo Zhang, Longtu Li, Ji Zhou, Zhenxing Yue, Zhenwei Ma, Zhilun Gui, *Microstructure Characterization and Properties of Chemically Synthesized Co2Z hexaferrite.* Journal of European Ceramic Society, 2001. **21**: p. 149-153.
9. Z.N.Wing, *Fabrication and Characterizatioin of Efective Medium Meta-dielectrics*, in *Materials Science and Engineering*. 2005, University of Michigan: Ann Arbor. p. 200.
10. P. Dragan, J.W. Halloran, G.E. Hillmas, G.A. Brady, S. Somers, A. Barda, and G.Zywicki, *Process of Preparing Textured Ceramic Composites*, in *Engineering*, U. Patent, Editor. 1997, J.W. Halloran: USA. p. 54.
11. Neelakanta, Perambur S., *Electromagnetic Materials*. 1995: CRC press.
12. V., Jayasundere N. and Smith B., *Dielectric constant for binary piezoelectric 0-3 composites.* J. of Appl. Phys., 1993. **73**(5): p. 2462-2466.
13. D. Y. Kim, Y. C. Chung, T. W. Kang and H. C. Kim, *Dependence of Microwave Absorbing Property on Ferrite Volume Fraction in MnZn Ferrite-Rubber Composites.* IEEE Transactions on Magnetics, 1996. **32**(2): p. 555-558.
14. L. F. Chen, Y. P. Hong, X. J. Chen, Q. L. Wu, Q. J. Huang, X. T. Luo, *Preparation and properties of polymer matrix piezoelectric composites containing alighed BaTiO3 whiskers.* Journal of Materials Science, 2004 (39): p. 2997-3001.

15. D.D., Carpi F. and Rossi, *Improvement of Electromechanical Actuating Performances of a Silicone Dielectric Elastomer by Dispersion of Titanium Dioxide Powder.* IEEE Transactions on Dielectrics and Electrical Insulation, 2005. **12**(4): p. 835-841.

16. Anjana P.S., George S., Thomas S., Subodh G., Sebastian M.T. and Mohana P., *Effect of Filler on the Microwave Dielectric Properties of PTFE/Ceramic Composites.* Proceeding of the Int'l Conference on Advanced Materials and Composites, 2007: p. 807-812.

17. P.S. Anjana, S. George, S. Thomas, M.T. Sebastian and P.T. Mohana. *Effect of Filler on the Microwave Dielectric Properties of PTEE/Ceramic Composites.* in *International Conference on Advanced Materials and Composites.* 2007.

Chapter 7

Anisotropic Magnetodielectric – Polymer Composites

7.1. Introduction

Experimental data of isotropic composites indicated difficulties of meeting the demand of equivalent permittivity and permeability at 300MHz because at frequencies above 10 MHz, the permeability of the ferrite itself is always lower than its permittivity. This means that for all possible composites, the permittivity of the composite is always larger than its permeability. As stated in Chapters 4 and 5, the miniaturization of antenna is optimized when permittivity and permeability of the ceramics are equal. Given the knowledge that the magnetic and electric fields are perpendicular to each other, we came up with an idea to formulate ferrite-polymer composites in such a way so that their dielectric and magnetic magnitudes divided into a higher and a lower value. This arrangement may be achievable by forcing ceramic particles to align along one direction to form uniaxial texture, with which the isotropic permittivity and permeability values split into two components of parallel and perpendicular, corresponding to the alignment directions. The longitudinal component of both permittivity and permeability is higher than that of perpendicular component. Since the longitudinal components of both dielectric and magnetic

properties along the same direction as well as their perpendicular components, there is an opportunity that the permeability magnitude at the parallel direction (stronger one) will be equal to the permittivity magnitude at the perpendicular direction.

The formed materials are called anisotropic or uniaxial from their texture. By arranging these anisotropic magnetodielectric materials appropriately on top of metallic antenna platform, the electric field of the antenna will sense the low permittivity direction of the material while its magnetic field will sense the high permeability direction of the material. The equivalent permittivity and permeability materials can be achievable. Schematic illustration of this expression is depicted in Fig. 7.1.

In this chapter, we describe two methods of making anisotropic composites, in which the first is dielectrophoresis and the second is coextrusion. Dielectrophoresis uses an electric field to produce an electric force on dielectric particles to arrange them aligned along the electric field lines. The coextrusion method applies a mechanical force on one head of a heat-softened rod of materials inside a specific die and drives them out through a die's orifice in the shape of fiber or filament, depending on the diameter of die's opening. By multiplication of this step, ceramic particles are driven to align along the length of fiber that consequence into an anisotropically textured material.

Part 1: Dielectrophoresis Method

7.2. Introduction

Dielectrophoresis is a term used to describe the translational motion of neutral matter which is driven by nonuniform electric field [1-3]. This motion is the result of the internal polarization of neutral matter in the nonuniform electric field. Different from a charged body, neutral matter does not accumulate charges on its surface as conductive materials do, but forms a separation of negative and positive centers inside its body instead. For this reason, charged bodies move along the electrical field line from a weaker field point to a stronger field point as a consequence of a statically attractive electric force. This movement is not affected by the uniformity of the field. Meanwhile, neutral bodies can only move in the nonuniform electric field from the effect of field gradient.

There has been number of researchers applying the dielectrophoretic technique to form fiber-like composites from particulates to increase mechanical properties [4-6], as well as to form semiconducting nanocomposites [7-9]. Another use is in biotechnology to separate bacteria, cytoplast, yeast cell, DNA, protein [1, 10-15]. Recent emerged research was conducted on nanometer size objects so that many scientists have believed that this technique is more advantageous for the development of nanotechnology [16-19]. It has also been tried for the synthesis of nano device from its easiness in controlling the movement of objects in a dielectric medium [9].

There have been two ways to access to dielectrophoretic phenomena: experimental and simulation. The experimental method deals with empirical observations while the simulation method approaches with considerations of interactions between inclusion particles and between inclusions with matrix at molecular level.

As mentioned above, the dielectrophoresis occurs when the polarization of neutral particles appears under the external electric field. We will start from the introduction of polarization modes as a background to go into detail of required electric field and force placed on particles as well as experimental parameters affecting the result of dielectrophoresis.

7.2.1. Polarization of matter

Polarization is the phenomenon in which there is an uneven distribution of charges inside a body due to their blocked or restricted movements. Difference of distribution mode and difference of charge magnitude divide polarization into types of (i) electronic, (ii) atomic, (III) dipolar, (iv) nomadic and (v) interfacial [1] as being illustrated in Fig. 7.2 [20]. Amongst them, the first four are believed to occur at a molecular micro scale while the last one occurs at the macro scale [1, 21].

Electronic polarization is a term to describe the distortion of positive and negative centers when matter is imposed in an electric field. However, this type of polarization is negligible for being considered in dielectrophoretic experiments as the exposed field is much weaker than the internal field of a matter (10^{11} V/m) [1, 21].

Atomic polarization is attributed to the wide difference of electron affinity of elements in maters. The combination of a very strong electron affinitive atom like chlorine with a weak electron affinitive atom like sodium is an example. Positive and negative charge centers locate separately on Na and Cl atoms. This polarization mode is generally moderated in inorganic solids, but not in organic compounds where ionic groups are missing.

Dipolar polarization happens in small inorganic molecules like H_2O, HF and NO or organic macromolecules containing functional groups like –OH, -CN, etc. In these compounds, the polarization is always present from the dissimilarity of electric affinity of bonded elements, but is not as strong as in atomic polarization. Under the influence of the electric field, this dipolar orients along the field direction so that it is called by another name as orientation polarization. Raju described the nature of this polarization type in detail to show that the movement of this permanent polarization under the electric field is also as small as that of electric polarization, which is in the range of 10^{-5} times their bonding length [21]. Therefore, this polarization mode is not relevant in calculating the dielectrophoretic force either.

Nomadic polarization associates the response of thermally excited charges situated on long domains like in a polymer or crystal lattice. When exposed in the electric field, the movement of charges occurs in a distance of more than a molecular length or several lattice sites, which means a big dislocation. Matter consisting of this mode must have an appreciable number of thermally induced roving charges and have a suitably long domain [1, 21]. One example of this type of polarization is conjugated polymers in which delocalized orbital is forced to move along the molecular length.

Since the produced excited charges are large and movable in a wide range, the influence of this polarization is remarkable in the dielectrophoresis.

Interfacial polarization occurs as the consequence of charge accumulation at interfaces of phases or crystals, causing a different distribution of charges from the center to the boundary of domains. Since this electric dislocation happens in the whole volume of the material, the charge distortion is produced at macroscopic scale. Interfacial polarization occurs rather more often than other polarization categories described above. For dielectric ceramics, the interfacial polarization is dominant while electric, orientation and nomadic polarizations are not relevant from the nature of electron interations.

7.2.2. Influence of non-uniform field on dielectric particles

The imposition of electric field on dielectric particles generates polarizations inside matter or, by the other ways, turns objects into dipolar. These internally charged bodies interact with each other to induce their movements to form anisotropic textured materials. In this section, we will describe parameters attributed to this movement.

7.2.2.1. Dielectrophoretic force

When dispersing dielectric particles with permittivity ε_2 in a medium with permittivity ε_1 and exposing the whole mixture into a non-uniform electric field E_e,

there will be an interaction between field lines and particles [1, 22]. These lines are distorted at the interface of the medium and particle, as seen in Fig. 7.3 according to the relative relationship between ε_1 and and ε_2 [21]. If an inclusion's permittivity is larger than that of the medium, then the field lines are distorted by the way that lines go through particles, as seen in Fig. 7.3a. The out-of-particle distorted electric field lines, in turn, form a new and nonuniform field between the particles. The enhancement of the field's nonuniformity by particles themselves is named the "bunching effect" and chains of aligned particles are named "pearl chains". Meanwhile, these lines are distorted to go around dielectrics if their dielectric permittivity is equal or smaller than that of the medium as was depicted in Fig. 7.3b. The enhancement of the field's uniformity results in the formation of an attractive force amongst themselves that, under the presence of an external electric field, align particles along the field lines. The mathematical expression of these explanations is given in Eq. 7.5 below.

The net electric force (F_e) the field produces on a particle [1, 22]:

$$F_e = (p.\nabla)E_e \qquad \text{(Eq. 7.1)}$$

Where p is the dipole moment vector, ∇ is the del vector.

$$p = \alpha.V.E_e \qquad \text{(Eq. 7.2)}$$

Where α is the polarizability per unit volume in unit field and V is the volume of the body.

Then the net electric force is expressed as follows:

120

$$F_e = \frac{1}{2} \cdot V \cdot \alpha \cdot \nabla \cdot |E_e|^2 \qquad \text{(Eq. 7.3)}$$

On the other hand, polarization of a sphere in a uniform E-field:

$$\mu = 4\pi \cdot a^3 \cdot \varepsilon_1 \cdot \left(\frac{\varepsilon_2 - \varepsilon_1}{\varepsilon_2 + 2.\varepsilon_1}\right) \cdot E_e = \alpha \cdot \vartheta \cdot E_e \qquad \text{(Eq. 7.4)}$$

or:

$$\alpha \cdot \vartheta = 4 \cdot \pi \cdot a^3 \cdot \varepsilon_1 \cdot \left(\frac{\varepsilon_2 - \varepsilon_1}{\varepsilon_2 + 2.\varepsilon_1}\right)$$

Hence:

$$F_e = \frac{3}{2} \cdot V \cdot \varepsilon_1 \cdot \left(\frac{\varepsilon_2 - \varepsilon_1}{\varepsilon_2 + 2.\varepsilon_1}\right) \cdot \nabla \cdot |E_e|^2 \qquad \text{(Eq. 7.5)}$$

This equation of dielectrophoretic force was constructed based on the assumption that for all materials, F_e is only dependent upon the dielectric constants of fillers and the medium. Given this, it is apparent that the polarization of dielectrics and their accumulated charges at the filler-medium interface is cancelled when their dielectric permittivities are equal. It means that there is not any force present between particles [1, 21-23].

In an attempt to study how the dielectrophoretic force depends on dielectric permittivity, values of ε'_1 and ε'_2 were varied from small to large in comparison with each other. It is interesting that F_e is stronger affected by medium's permittivity than that of inclusions. It changed more apparently with the increase or decrease of ε'_2 than that of ε'_1 as being shown in Table 7.1.

7.2.2.2. Threshold electric field

In addition to the dielectrophoretic force, filler particles in a dielectric liquid medium are also driven by other forces and they will be manipulated by the most dominant one. Assuming that the movement of particle is steady, the sum of all forces is zero and can be expressed in a mathematical equation as follows:

$$F_e + F_j + F_{os} + F_\eta = 0 \qquad\qquad (Eq.\ 7.6)$$

Where F_η = -6π.a.η.v: Stoke's drag or viscous drag force

F_j = q.E : Coloumbic force

F_{os} = -kT/2a

In this equation, v is the movement speed of particle, a is the particle diameter, η is viscosity of medium, and q is the free charge of particle indicating a combination of electric field, dielectric permittivity and conductivity through the balancing of electric charge inside and outside of dielectric particles [1]:

$$q = \frac{3t.E_o(\varepsilon_2.\sigma_1 - \varepsilon_1.\sigma_2).cos\theta}{(\varepsilon_2 + 2.\varepsilon_1)} = q_o.cos\theta \qquad\qquad (Eq.\ 7.7)$$

where, θ is the angle between a vector from center of particle to a point on its surface and a vector of electric field.

Given the presence of external forces, it is necessary to have a strong enough electric field to overcome those external effects. The field at which alignment starts is named the threshold electric field. The magnitude of this field is expressed by an equation derived by Pohl [1]:

$$E_{crit} = \left(\frac{\varepsilon_2 + 2\varepsilon_1}{\varepsilon_2 - \varepsilon_1}\right)\left(\frac{kT}{2\pi\varepsilon_1 R^3}\right)^{\frac{1}{2}}\left[1 - \frac{1}{4}\left(\frac{\varepsilon_2 - \varepsilon_1}{\varepsilon_2 + 2\varepsilon_1}\right)\right]^{\frac{1}{2}} \qquad \text{(Eq. 7.8)}$$

If $\varepsilon_2 \leq 10\varepsilon_1$, this equation can be simplified as:

$$E_{crit} = \left(\frac{\varepsilon_2 + 2\varepsilon_1}{\varepsilon_2 - \varepsilon_1}\right)\left(\frac{kT}{2\pi\varepsilon_1 R^3}\right)^{\frac{1}{2}} \qquad \text{(Eq. 7.9)}$$

Pohl obtained this expression from the consideration of the total work necessary to attract two dielectric spheres approaching each other and their resistance to thermal vibration energy (kT/2a). This work includes the work to divide charged centers inside particle (polarization work) U', the work to form a dipole moment for each particle U_1 and the work to bring two particles next to each other U_2. Mathematical expression of these works is as below:

$$U = U_1 + U_2$$

$$U_1 = -\mu.E$$

$$U' = \frac{U_2}{2} = \frac{1}{2}\mu_2.E = \frac{1}{2}\alpha.E^2$$

In this research, we applied a modest electric field 3 kV/cm for the dielectrophoretic experiment. A comparison of the dielectrophoretic force with its complementary forces is given in Table 7.2 and Fig. 7.4, respectively. In this circumstance, the dielectrophoretic force was dominant over other forces on the whole range of ceramic particle size.

7.2.3. Dielectrophoretic experiments

7.2.3.1. Choose polymer

Polymers need to have a lower permittivity than that of Co_2Z ($\varepsilon'= 12$) and a low permittivity loss, in the range of 10^{-4} to provide the high performance efficiency of material when being applied on an antenna. Furthermore, they need to be in liquid form during the dielectrophoretic experiment and should easily be hardened by the time it finishes. Low Density Polyethylene, as used in Chapter 6, was not applicable in this case. It can be used to make a castable material, but not feasible to produce moldable material, which is flexible and able to assemble on site. Park and Robertson [4] executed the dielectrophoretic research using Urethane dimethacrylate (UDMA) and 1,6-hexanediol dimethacrylate (HDDMA) as matrix in which glass beads were immersed. These monomers reacted with each other and polymerized under the radiation of blue light. However, they were not applicable in this research because they contain functional groups which interfere with the high permittivity and loss of the dielectric material at microwave frequencies.

Silicone elastomers RTV 6166 from GE's silicone met all above mentioned criteria and were used as the distributing medium for Co_2Z in this research. RTV 6166 consists of two components which are named RTV 6166A and B, with A standing for elastomers and B standing for hardener. These were both present in the liquid form with properties given in Table 7.3. The abbreviation RTV stands for Room Temperature Vulcanization, meaning that silicone rubber canbe self solidified at room temperature. The two components A and B of silicone rubber have the same

main chain structures, but containing conjunctional functional groups so that when being mixed they react to prolong the main chain and harden the material. Though we did not know molecular structure of these two silicone components, its hardening is belonged to one of two following reaction mechanisms [24]:

Mechanism 1:

$$\equiv Si - OH + HO - Si \equiv \; \rightarrow \; \equiv Si - O - Si \equiv \; + H_2O$$

Mechanism 2:

$$\equiv Si - H + H_2C = CH - Si \equiv \; \rightarrow \; \equiv Si - CH_2 - CH_2 - Si \equiv$$
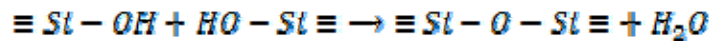
Since the cross linking reaction 2 requires a catalyst of Pt or other noble metals, then we presumed the cross linking reaction of silicone elastomers RTV 6166 belongs to mechanism 1. Given the high Si-O-Si angle (143°) and low torsion energy around the main chain (4 kJ/mol) in comparison to that of LDPE (15 kJ/mol), silicone elastomers consist of a unique flexibility. Similar to Polydimethyl siloxane (PDMS), hardened silicone elastomers have high dissociation energy (445 kJ/mol) and a partial polarization inside their molecules to make alkyl groups charged and stabilized under impact of heat and oxidative agents.

The role of RTV 6166 is partly illustrated in Fig. 7.5. It retained the liquid state long enough and was controllable under a right curing condition for Co_2Z ferrite particles to align along the electric field lines. After being hardened, though being soft and flexible, its structure was sufficient to sustain the alignment of ceramic particles.

7.2.3.2. Sample preparation

As discussed in the introduction chapter, Co_2Z has been found to be a promising candidate, which offers the most efficient miniaturization of microwave devices due to its high permittivity and permeability at microwave frequencies. After being ball milled and dried, Co_2Z ferrite was scaled and divided into two parts to mix with elastomers and hardeners so that the powder to liquid volume ratio was equivalent in both mixtures. The composition of samples was given in Table 7.3.

When preparing samples, it is important to minimize the entrapment of air or humidity inside the irregularly shaped solid particles. With permittivity and permeability equal to one, the air unpredictably entrapped in bulk material causes the variation of its properties [25-27]. Meanwhile, the possible adsorbed water results in the electrohydrodynamics [28], causing the particles being charged to move toward the electrodes. The assembly of inclusions in this case requires higher electric field strength as well as longer time and higher field frequency. It also means that the experiment would require more critical conditions to obtain the same alignment degree [25]. To prevent these phenomena, Co_2Z was dried at 100°C for 24 hrs before use. The adsorbed air was extracted by vacuum at a pressure of 10^{-3} Torr for half an hour. The RTV 6166 liquid was contained in a syringe connected to the mixing bag through a needle as shown in Fig. 7.6.

Liquid silicone elastomer components were injected into the bag to mix with the powder. Mixing was performed for at least half an hour before the formed slurry was pulled into a syringe. Two slurries from two syringes were gradually injected into a

static mixer. This static mixer is an equipment which consists of two tubes attached with other along their bodies and they share the same output orifice to connect to a mixing tube. Inside the mixing tube, there are many blades arranged statically in an order. When being driven out, two slurries met and mixed with each other with the help of these blades. Blades inside mixing tube do not move, so that the mixing is called static. The movement of slurries over specifically arranged mixing blades prevented the entrapment of air into slurry mixtures. After being dispersed into silicone elastomers, Co_2Z was randomly distributed in the whole volume, but would sediment by gravity if the slurry was retained too long before the dielectrophoretic experiment. Under the imposition of the electric field, ferrite particles were polarized and transported to align themselves along electric field lines. Their positions were sustained after the silicone solidified and electric field was released. Prior to evaluation, the experiment consisted of three stages, as depicted in Fig. 7.7, which were ingredient preparation, mixing stage 1 and mixing stage 2.

Silicone rubber consists of two components which are elastomers and hardeners. According to the manufacturer, the two components should mix at the ratio of 1:1 for fast hardening. In our primary tests, we measured the hardening time of silicone rubber to reveal that its solidification time was about 5 minutes at room temperature. This was too short for the alignment of dielectric particles under the electric field. When being tested at the ratio of one volume of elastomer to two volumes of hardener, the solidification time was prolonged up to 120 minutes and this was more than enough for the alignment process of Co_2Z ferrite particles. However, this time frame was too long and would allow the sedimentation of particles from gravity. Fortunately,

when occuring at 80°C, this curing time reduced to 30 minutes and was apparently suitable for our experiment [29]. Therefore, the ratio A:B was modified to 1:2.

7.2.3.3. Experiment

After samples were carefully prepared, they were injected gradually into a sample chamber in which two copper electrodes stayed parallel and 22 mm in distance from each other. The voltage was controlled through a Trek 610C high voltage transmitter and the signal was generated by an oscillator (Thulby Thander TG501). The dielectrophoresis was conducted at an electric field of 3 kV/cm and frequencies of 60 Hz and 1 kHz to compare the effect of frequency on the dielectrophoretic efficiency [30-32]. The sample chamber was immersed in an oil bath to control the temperature for elastomers solidification. Experimental equipments are shown in Fig.7.8.

After the dielectrophoretic experiment, the sample was cured at 100°C for 5 hours to finish the cross linking process of silicone elastomers. Pieces of samples were prepared for dielectric permittivity and magnetic permeability with dimensions described in Chapter 6. In this experiment, we measured these two parameters for both isotropic and anisotropic samples in which the latter case included all specimens whose Co$_2$Z particles aligned either parallel or perpendicular to the measuring field. The obtained data of isotropic samples were compared with calculated data using the Jayasundere-Smith equation, whilst the data of anisotropic samples were compared with ones calculated from parallel and transverse model [33]. We assumed that the experiment was successful to form a high degree of alignment so that strings of ferrite

particles were formed. We also assumed that these particles had strong connection with each other so that they behaved like continuous fibers [4, 25]. The formed composites, in consequence, contained properties following the simple mixing rule for anisotropic fiber composites. The equation for this prediction was given in Chapter 6, Eq. 6.1.

There was a challenge for the permittivity's measurement because of the softness and flexibility of specimens. The design of sample's clamp intended to avoid the gap between equipment and sample's surfaces generated a dramatic high pressure on the sample so that the actual thickness of samples varied with measuring time. Furthermore, this pressure would deflect the strings of filler particles, making their shape changed. The consequence was that the measured data were very much different from expected. Measurement data were unacceptable until the pressure from the sample's clamps was released and a supplementary tool was used to measure the thickness. The measurement was taken at different locations on specimen's surface and an average value was recorded. Samples after permeability and permittivity tests were subjected into microstructural investigation.

7.2.4. Results and discussions

7.2.4.1. Alignment efficiency

For the microstructure investigation, there were several methods usually applied, those were such as polarized transmission microscope (PTM) [34] and Scanning Electron Microscope (SEM) [4-5]. A. Knapp and J.W. Halloran used PTM to observe

the formation of clusters inside a mixture of polymers due to the immiscibility. In order to apply this technique, the sample must be thin and transparent enough for polarized light to go through. They cut small pieces of thermoplastic polymer from their final samples and melted them between glass slides to form thin films for PTM observation. Thermosetting polymers are not applicable to this technique as they are unable to melt under the heat treatment. This technique was not suitable to observe our samples because the formed composite was black from the black color of Co_2Z. Furthermore, the advantageous flexibility of silicone rubber made it difficult to cut samples into thin layers.

The samples in the research of Park and Robertson [4-5] were rigid solid from the polymerization of urethane dimethacrylate (UDMA) and 1,6-hexanediol dimethacrylate (HDDMA) under the initiation of blue light. The inclusions used in their experiments were homogeneous size transparent glass beads which did not introduce any color preventing them from observation. SEM was applicable in their research.

Microstructural observation of our samples' cross sections was given in Fig. 4.10a and b, corresponding to two surfaces perpendicular to each other but parallel to the electric field lines. Images of other samples of other compositions could not obtain because their structures were collapsed in the high vacuum chamber of SEM machine.

We could not see the alignment of inclusions in those two images, but rather a random distribution of particles. Being concerned with measuring data, it was apparent to us that the alignment happened at some degree. However, it did not show

up in these SEM images, even if we tried several times. We presumed that the alignment of particles was not straight along the electric field lines, i.e. perpendicular to two electrode surfaces so that a straight cut along alignment direction went across ferrite strings or columns to appear as an isotropic distribution. This phenomenon was observed by Randall C. A. et al. [35], Park and Robertson [6], Wilson S. A. et al. [25] without any explanation. Studies of Furedi and Valentine [1] on different material systems, different filler volume fractions, and under various frequency ranges showed that the deflected assembly phenomenon did not happen at very low filler volume fraction of 0.9 Vol% and at low frequency range of tens of Hz.

It may be possible to apply assumptions of Fricke and Cole et al. [36-37] which says that there are two torques induced on the filler particles. The first torque is resulted from polarization and the second one is caused by charging because all dielectrics are partly conductive. The polarization of materials is usually along the electric field lines so that it drives particles to move translationally to assemble along field lines. This torque does not bend the alignment of filler particles. Meanwhile, due to the fact that the material is not completely insulation, there is a charge on particle's surface. The presence of this charge forces particles to move perpendicularly to the direction of electric field so that the final position of the strings is deflected to the electric field lines.

Another reason may come from the non-optimistic design of experiment that would weaken the effect of applied frequency and voltage of the electric field. These impacts will be discussed in more details in a later section. Hase M. et al. [2] reported a longest alignment of 1 mm of equal size glass spheres in their experiments using

131

accelerated anisotropic electric field with a gap between two electrodes of 1.4 mm. The requirement to have large enough materials for measurement keeps the design a large sample cell with a distance of 22 mm between two electrodes. This disadvantage would be one reason for a low efficiency of alignment.

The observation of microstructure of specimens was hindered by the black background of matrix, which was attributed from the random distribution of sub micron filler particles. It means that there was a large amount of very small particles in the range of submicron size which were not strongly affected by the electro motive force (emf). As given in Table 7.2 and depicted in Fig. 7.4, the dielectrophoretic force is dominant over the whole range of particle sizes. However, if the dielectrophoretic force is strongest within a distance of 1mm from the electrode's surface and decreased at farther distances, it would be possible that the drag and thermal agitation forces controlled dielectric particles in sub micron size range. Research results given by Hase et al. [38] did not have any further explanation. More study is needed to clarify the variation of the dielectrophoretic force along the distance from the electrode's surface.

Apart from SEM, we tried of using a direct light microscope for low filler composition specimens during the dielectrophoresis [29] to observe the microstructure of the specimens. However, this technique did not depict correctly behaviors of ferrites particles under an electric field with high concentration from interaction amongst particles.

7.2.4.2. Permittivity and permeability of specimens

Results of the dielectric permittivities of samples which were conducted at frequencies of 60 Hz and 1 kHz were given in Fig.7.10 and Fig. 7.11, respectively. The magnetic permeability of samples those were prepared at the same experimental conditions were given in Fig. 7.12 and Fig. 7.13, correspondingly. Dielectromagnetic properties of composites were proportional to the increase of Co_2Z ferrite composition though this was not a linear relationship. It is apparent that the higher the ceramic composition, the stronger the interaction between ceramic particles so that the inclusive behavior of composites was reduced.

Evaluation of the influence of frequency on assembly's efficiency was given in Fig. 7.14 and Fig. 7.15; Fig. 7.16 and Fig. 7.17 for permittivity and permeability, correspondingly. The cartoon given in Fig. 7.14 illustrates that the high permittivity and high permeability values are along alignment direction as well as along the measuring electric and magnetic fields. Permittivity and permeability magnitudes in the parallel direction to the measuring electric field lines were compared to those in the perpendicular direction to the measuring electric field. The better the assembly effect, the larger the split values of these dielectromagnetic properties. The influence of field frequency on assembly at low filler volume fractions seemed to be more apparent than at high volume fractions so that they formed a maximum point at 20vol%. Considering that the electric field generated similar effect on all samples, there was a higher amount of fillers not aligned in high composition samples in comparison with those with low composition. Therefore, the variation of alignment efficiency amongst specimens is understandable. Dielectrophoresis at high frequency

133

accelerated the alignment of particles better than at low frequency. This was consistent with observations given by Wilson S.A. et al. [25], who elucidated three alignment degrees of ceramic particles on different electric field frequencies, strength and experimental time. Schematic illustration of these three was depicted in Fig. 7.18. The weakest alignment degree is characterized by short chains which consist of a few particles surrounded by a large number of randomly distributed particles. This type is formed at very low frequency ranges and low electric field strength. With the increase of frequency, particles build up longer chains with a reduced amount of randomly distributed ones to form type II. The application of both high frequency and high electric field would strongly promote the interaction between particles so that the alignment produces not strings or chains, but columns of particles. This is the strongest assembly they observed with their piezoelectric ceramic - epoxy systems. The difference of dielectric permittivity between piezoelectric ceramics and epoxy is in the range of thousands. Nevertheless, the permittivity and permeability difference in Co_2Z-silicone systems was within the range of tens, with which weak interaction between ferrite particles resulted into short chains consisting of small number of particles. We can see this difference from consideration of field generated amongst particles. According to Pohl [1] and Randall C. A. et al. [39-40], the induced field between fillers under the application of external electric field is given by equation:

$$E_{induced} = \frac{3.\varepsilon_2 E_0.cos\theta - 3\varepsilon_1 E_0.sin\theta}{\varepsilon_2 + 2\varepsilon_1} \qquad \text{(Eq. 7.10)}$$

Where, ε_1, ε_2 are permittivities of matrix and inclusions, correspondingly, θ is the angle made of a vector between two particles and electric field line, and E_0 is field strength of electric field.

Given the permittivity of piezoelectric was 1700 and of epoxy was 2.8; the induced field strength was $2.99E_o$. Given the permittivity of Co_2Z was 12 and of silicone elastomer was 2.8, the induced field strength was $2.04E_0$. All particles were assumed in line with field lines.

7.2.5. Factors influence the dielectrophoresis

7.2.5.1. Electric field (AC or DC)

In principle, either direct current (DC) or alternative current (AC) electric field is applicable to dielectrophoretic experiment [1, 41-44] because the dielectrophoretic force F_e is dependent mostly on the real part of the Clausius-Mossotti factor as given in Eq. 7.3. This factor does not change when material is exposed into either the DC or AC electric field. On the other hand, the E^2 term in F_e equation indicates that the AC electric field does not impact on the behavior of mateial exposed into it.

However, the efficiency of their applications is different with the application of DC field usually resulting in lower assembly yield than that of applying AC. Randall C. A et al. [31], Kim T. H. et al. [45], Hawkin B. G. [46] applied dielectrophoresis technique in their research, in which they compared using DC electric field to AC electric field to demonstrate that the application of DC electric field yielded low

alignment efficiency. In addition, DC field produced a charge layer on the surface of dielectrics. When electric field raises up to a critical value, particles move under the influence of an isostatic electric attractive force stronger than the Coulombic force amongst them [39]. Dielectric particles, under this attractive force, move to opposite charged electrodes that result in a disordered structure of composite. Some research reported the evidence of electrolysis on electrode surface in the case of using DC electric field [38, 46] with argument that this is attributed to the partial conductivity of the medium.

Kim T.H. et al [9] applied either DC or AC electric field for their research in aligning gallium nanowires. They applied voltage values of 1, 5, 15 and 20 for DC case and 1, 5, 10, 15, 20 for AC case. The use of AC field showed better alignment achievements (80%) than that of case using DC field (40%). They did not discuss this discrepancy; however, apart from its influence on electrolysis, the shape of nanowires also has a relevant contribution. As mentioned by Pethig R. [11-12] and Hui Liu [47], the polarization of non spherical particles usually occurs along their longer directions. The unavailability of frequency would make these particles not strongly attractive to the electric field and would weakly align along the field.

Hase M. et al. [2] argued that the application of the DC electric field will cause particles to have a large amount of free charge due to the triboelectric effect that, in turn causing the electrophoretic force. When particles are aligned between the two electrodes, the conduction occurs, leading to the electrolytic phenomenon.

7.2.5.2. Effect of frequency

Frequency of the external AC electric field plays an important role in regulating strength of the dielectrophoretic force. It also indicates that the particles will align along the strong or the weak electric field as well as the direction of alignment of particles. In the general expression of dielectrophoretic force, the frequency dependent term is Clausius-Mossotti factor α. In general circumstances, α is described by an expression of complex permittivity of both medium and fillers as follows:

$$\alpha = \left(\frac{\varepsilon_2^* - \varepsilon_1^*}{\varepsilon_2^* + 2.\varepsilon_1^*} \right) \qquad\qquad \varepsilon^* = \varepsilon' - \frac{i\sigma}{\omega}$$

Sigma (σ) is the conductivity and ω is the angular frequency of the applied electric field. As conductivity of most dielectric materials is much smaller than the magnitude of permittivity, it is negligible and, for the sake of simplicity, this parameter is usually ignored [48]. Thus, the expression of α becomes:

$$\alpha = \left(\frac{\varepsilon_2 - \varepsilon_1}{\varepsilon_2 + 2.\varepsilon_1} \right) \qquad\qquad\qquad (Eq. 7.11)$$

where ε_1 and ε_2 are real parts of permittivity of the medium and inclusions, respectively.

The presence of this term results in different behavior of inclusions along with frequency of the applied electric field. The real part of permittivity results into the dielectrophoresis, while the imaginary part results in the rotation of particles in the electric field. Hughes M.P [8] called them in one common name as *electrokinetics*.

The Clausius-Mossotti factor represents the polarization of material that changes under the impact of field frequency. Pethig and Markx [11] reported that the polarizations associated mostly with particle surface charge at frequencies below 1kHz, but switched at high frequency ranges due the permittivity loss (ε") and the electric resonance.

Havriliak and Negami [49] derived mathematical equations to quantitatively describe the dependence of permittivity in all forms to frequency of electric field:

$$\varepsilon^*(\omega) = \varepsilon_\infty + \frac{\Delta\varepsilon}{[1+(j\omega\tau_0)^{1-\alpha}]^\beta} - j\frac{\sigma_0}{\varepsilon_0}\omega^{-s} \qquad \text{(Eq. 7.12)}$$

$$\varepsilon'(\omega) = \varepsilon_\infty + \Delta\varepsilon\frac{\cos(\beta\varphi)}{[1+2(\omega\tau_0)^{1-\alpha}\sin(\frac{\alpha\pi}{2})+(\alpha\tau_0)^{2(1-\alpha)}]^{\beta/2}} \qquad \text{(Eq. 7.13)}$$

$$\varepsilon''(\omega) = \Delta\varepsilon\frac{\cos(\beta\varphi)}{\left[1+2(\omega\tau_0)^{1-\alpha}\sin(\frac{\alpha\pi}{2})+(\alpha\tau_0)^{2(1-\alpha)}\right]^{\frac{\beta}{2}}} + \frac{\sigma_0}{\varepsilon_0}\omega^{-s} \qquad \text{(Eq. 7.14)}$$

Where α, β are shape parameters; ω is angular frequency, ε_0 and ε_∞ are limit of permittivity at low and high frequency, and φ is expressed as:

$$\varphi = \arctan\left[\frac{(\omega\tau_0)^{1-\alpha}\sin(1/2\alpha\pi)}{[1+(\omega\tau_0)^{1-\alpha}\sin(\frac{\alpha\pi}{2})]}\right]$$

$\Delta\varepsilon$ is the dielectric relaxation strength, representing the contribution of the orientation polarization

$$\Delta\varepsilon = \varepsilon_s - \varepsilon_\infty = \frac{2}{\pi}\int_0^\infty \varepsilon''(\omega)d\ln\omega \qquad \text{(Eq.7.15)}$$

$$1 - \alpha = \frac{d\ln\varepsilon''}{d\ln f}\Big|_{\omega \ll 1/\tau_0}$$

$$(1 - \alpha)\beta = -\frac{d\ln\varepsilon''}{d\ln f}\Big|_{\omega \gg 1/\tau_0}$$

And τ_0, τ_{max} are relaxation times whose relationship is described mathematically as:

138

$$\tau_0 = 1/2\pi f_0$$

$$\tau_{max} = \tau_0 \left[\frac{\sin\left[(1-a)\beta \frac{\pi}{(2+2\beta)}\right]}{\sin\left[(1-a)\frac{\pi}{(2+2\beta)}\right]} \right]^{\frac{1}{1-\alpha}}$$

τ_{max} is the maximum relaxation time at which, the loss peak is at maximum value.

The combination of permittivity of all currently available electromagnetic materials results in values of the Clausius-Mossoti factor is in the range of +1 to -0.5 [11]. This value has a significant role in determining whether particles are aligned or spread under the influence of electric field. Positive values of alpha infer that filler particles will assemble because of the formation of induced attractive force amongst them. Negative values of alpha imply that repulsive forces are formed amongst filler particles [37, 50].

As both the real and imaginary permittivities vary with frequency, at a very high frequency range which is over the cutoff frequency, the electric field causes resonance so that real permittivity value of fillers decreased. Furthermore, the frequency affected on the alignment direction of particles in the case they are non-spherical. At low frequency, the polarization happens along the longitudinal direction of particles, and they align with this axis along the direction of electric field. As the frequency increases, the dipole along this axis reaches dispersion, but the dipole formed in the transversse direction does not. So, the particle will rotate 90° and align perpendicular to the field [47].

Jones described in more detailed the dependence of the dielectrophoretic force on the frequency [22]. He applied a simulation method named *effective moment method* to

express the forces and torques produced in the electric field. Considering particular dielectric particles consisting of two different layers of different materials in which internal layer is the isolative material while the outer layer is the conductive material, he introduced the generalized polarization coefficient $K^{(n)}$:

$$K^{(n)} = \frac{\varepsilon_2 - \varepsilon_1}{n.\varepsilon_2 + (n+1)\varepsilon_1}$$

This equation represents the polarization of multipolar moment in the reality consisting of an array of homogeneous spherical particles in the electric field. When n=1, this expression becomes the Clausius-Mossotti function applying for the dipole moment.

In our circumstances, as the permittivity of Co_2Z particles was stable up to the frequency of 1 GHz, the variation of the external electric field in the range of few tens kHz would not affect on neither the dielectrophoretic force nor attractive force among particles. However, as reported by Davis [36] and Bowen et al. [29], high frequency impacts the fluid to cause a turbulent flow in the suspension. This optimal frequency was not dependent on the filler composition of the suspension. There would be a reason for our experiments and more research has to be done for further information.

7.2.5.3. Relative dielectric permittivity of fillers and medium

The role of dielectric permittivity of fillers and medium on efficiency of dielectrophoretic experiment is expressed in Clausius-Mossotti equation (α).

Dielectrophoretic force is proportional to the difference of permittivity of fillers and liquid. If the permitticity of inclusions is higher than that of the medium, then dielectrophoretic force has a positive value and vice versa [51-52]. The higher the difference, the stronger the attractive force amongst particles and, in turn, the higher yield of assembly [1]. Pohl derived a simple equation to describe the influence of permittivity of fillers and medium on induced field between particles:

$$E_{induced} = \frac{3\varepsilon_1}{\varepsilon_1 + 2\varepsilon_2} \qquad \text{(Eq. 7.15)}$$

Bowen C. P. et al [29, 39] developed this equation into a more general form including the relative position of particles to the field lines as given in Eq. 7.10. Again, the calculation in the results section indicated how much influence dielectric permittivity of components has on dielectrophoresis efficiency. Davis [36] and Aubry [23, 37] agreed with this concept.

$$F = \frac{24.a^6.E^2}{R^4} \left[\frac{\varepsilon_2(\varepsilon_1 - \varepsilon_2)^2}{(\varepsilon_1 + 2\varepsilon_2)^2} \right] \qquad \text{(Eq. 7.16)}$$

Where, a is particle's average radius, R is distance between particles, E is applied field strength.

If we consider parameters of a, R and E similar to all cases so that the term before the parentheses is a constant (k), then the attractive force in our case ($\varepsilon'_2 = 12$, $\varepsilon'_1 = 2.8$) is 0.91k. For materials having a large difference between two permittivity values, for instance 1700 and 5, this is 5.03k. The attractive force in this case was 5 times stronger than that of Co_2Z –silicone elastomer system and the assembly efficiency would be very much better.

7.2.5.4. Particle size and shape of fillers

As mentioned above, the impact of other forces apart from the dielectrophoretic force would result in low yield of alignment or separation. All these matters come by from the particle size of objects used in the experiment. According to the calculation of Pohl [1], the dielectrophoretic force applied on particle with diameter of 1μm is bigger than other side effects to manipulate. Research of Park and Robertson [4-5] on the alignment of glass beads by an AC electric field reported that the dielectrophoresis is not applicable for particles to have diameter larger than 25 μm. Randall and his colleagues [31] indicated that particles with the diameter larger than 100nm can be used in dielectrophoresis research. However, efficiency of the assembly also depends on the viscosity of medium. A general trend is that, for a specific liquid medium, the larger particle size, the stronger the viscous drag force will be to alter the alignment of particles.

The role of particle shape having on the efficiency of dielectrophoresis was considered. Liu [47, 53] and Winter [19] conducted their research, applying theoretical mathematical simulations on irregular particle shapes of ellipsoidal, cylindrical. They had the same conclusions on the variation of polarization inside particle under different particle's shapes. Spherical particles are isotropic to all directions so that the polarization at any direction is consistent. Meanwhile, ellipsoids polarize along their longitudinal direction. In addition, the physical dimensions of ellipsoid would impose particles into different electric field strength, either to electrodes or neighbor particles.

7.2.5.5. Design of experimental cell

The experimental cell is the cell in which the sample slurry was retained and exposed into an electric field. The alignment of dielectric particles and solidification of liquid also occurs in this cell. Therefore, the design of this cell is important for the assembly efficiency of particles.

For most of cases, the cell consists of two parallel electrodes which are tightened or embedded into two parallel surfaces of a container, where slurry stays. Park and Robertson [4] designed their cells in which two aluminum electrodes were embedded parallel into a cuvette. The distance between these two electrodes was 0.7 cm, which was widest amongst those reported so far. Others [23, 29, 33, 39, 54-55] designed their experimental cells with electrode distance was less than 2 mm. This short gap between the two electrodes allowed them to control the electric field as high as 7.5 kV/mm without going beyond the capacity of the high voltage transducer. In our research, since we want to investigate both permittivity and permeability of specimens at directions either parallel or perpendicular to the electric field lines, the gap between electrodes should be wide enough to provide samples with corresponding dimensions for the measurement. With 22 mm in distance, the electric field could not set too high so that it might not strong enough to produce a high assembly yield [1, 22].

All above mentioned researchers reported the application of flat electrodes with the assumption that the induced secondary electric field between particles would be a dominant factor to assemble particles in line. They have not indicated any difficulty

in aligning dielectrics with high permittivity and for most of their research; they worked with high permittivity materials. For those circumstances consisting of low permittivity difference between fillers and medium, there will be a weak induced field between particles so that the assembly efficiency would be eliminated. A strong anisotropic electric field would more beneficial to achieve high assembly yield. A novel method introduced by Hase M. et al [38] would be very effective to meet this demand as it formed a matrix of micro pillars on the electrode's surface. Authors used laser light to locally melt the copper electrode surface to introduce holes with a diameter of 28 μm. The melted copper piled up on the edge of holes with a height of 40 μm, where electric charge is accumulated which, in turn, generates higher electric field than that of their surroundings.

7.2.5.6. Mixing process

There have been several studies reporting the mixing process of ceramics with polymer by hand and aided by vacuum [27]. This technique is very simple and easy. However, mixing manually in the opened container would cause air to be stirred in and captured inside structure. The vacuuming stage was to withdraw air bubbles out of the liquid silicone before it solidifies. The presence of air bubbles made silicone rubber look like foam full of holes and open pores that again show the presence of porosity.

In our research, we used two different plastic containers containing fine Co_2Z powder and one silicone component. Air and humidity were removed by vacuuming. The

144

vacuuming of dry powder was easier than that of the slurry. Liquid silicone was stored in a cylinder which was connected to the plastic bag of ceramic powder, but isolated by a thin layer of polyfloroethylene.

7.2.6. Applicability of dielectrophoresis in forming anisotropic composites

Fig. 7.19 depicts the relationship between permittivity and permeability of anisotropic Co_2Z-elastomer composites to that of isotropic Co_2Z-LDPE. The contour of anisotropic curve moved further toward the equivalent permittivity-permeability region. It implies that there is an opportunity for anisotropic Co_2Z-silicone elastomers to achieve equivalence status.

The comparison of permittivity-permeability relationship between anisotropic Co_2Z-silicone elastomers and isotropic Co_2Z-elastomer is also given in Fig. 7.20. A similar tendency is observed in this case with better approach of the permeability magnitude to the permittivity magnitude. Even though, there is still a big gap between experimental results and the expectation.

There have been many research succeeded in aligning dielectric ceramic particles along an electric field. The difference between their materials and the material used in this research was the magnitude of material's permittivity. While their materials' permittivities are more than a 100 and some cases more than a 1000, Co_2Z's permittivity is 12. It is apparent that this property of Co_2Z is not very much higher than that of the polymer and elastomers matrices. However, it does not mean that it is impossible to align Co_2Z particles by using electric field.

There are many parameters of the dielectrophoretic experiment can be modified to improve the alignment efficiency such as (i) electric field, (ii) frequency of the electric field, (iii) sample chamber design, and (iv) electrode.

The magnitude of the applied electric field should vary depending upon the magnitude of permittivity of the dielectric material. For those materials to have a high permittivity in the range of few hundreds to more than a thousand, the electric field can use at a moderate magnitude. For those materials to have a low permittivity in the range of ten or few tens, the electric field should be strong to generate enough the polarization inside the dielectric particles. This should be applied in our circumstance.

The usage of a high electric field would be hindered by the large sample chamber, in which the gap between two electrodes is big. As mentioned in Section 7.2.5.5 above, this large sample chamber design aimed to collect large enough material for all measurements of permittivity and permeability along parallel and perpendicular directions to the alignment direction. However, these measurements are to compare with the theoretical model only, which was established in this research stage. Therefore, it does not need to conduct all the measurements, but some of them to show the compliance of experiment to the theoretical calculations and to show the efficiency of alignment. With this simplification, the sample chamber can be redesigned to narrow the gap between electrodes.

The redesign of the sample chamber also brings more opportunity for the electrode's modification to generate a stronger non-uniformity of electric field as described in the Section 7.2.5.5.

As described in Chapter 8, the equivalent permittivity-permeability composites of Co$_2$Z-elastomers by using the dielectrophoresis technique are theoretically attainable. This depends on the alignment of Co$_2$Z particles along the electric field lines. The low permittivity magnitude of Co$_2$Z is a challenge, but there are still a lot of opportunities to improve and make the dielectrophoresis applicable in this case.

Part 2: Co-extrusion

The dielectrophoresis method did not provide a long string of aligned ceramic particles to form anisotropic composites. As being mentioned above, the most optimal structure of unidirectional composite would be in the column form. Meanwhile, the co-extrusion technique invented by D. Popovich, J.W.Halloran et al.[56] has been recognized as a novel technique to manufacture fine composite textures [57-59]. Fiber composites with fiber diameter as thin as 60 μm can be formulated. It is a possibility that this method could be applicable in forming unidirectional Co_2Z-polymer composites in which Co_2Z particles align uniaxially. Therefore, this technique was applied in an alternative attempt to synthesize unidirectional fiber composites by the mechanical force, in which fibers were isotropic particulate composites embedded in another polymer. In order to differentiate to the dielectrophoresis, we called this structure as the core-shell structure.

7.3. Introduction

The co-extrusion method can be understood as the derivation of extrusion technique in which two or more than two components are enforced through the same die to manufacture a green body of uniform cross section area [60]. This method has advantage in reducing cost with a very much easier tactic and in reduced processing

steps in producing complicated structures like multilayer ceramics, tubes and some types of materials those are challenge to fabricate by the use of other methods like monolithic ceramics fibers [59, 61-63], Macrochannelled-Hydroxyapatite Bioceramics [64], Mircro-fabrication of fine textured ceramics [58, 65].

The principle of coextrusion methods is simple. At first, core-shell feed rods need to be formed. Ceramics powders and polymers were mixed inside a hot shear mixer so that powders are evenly distributed into the polymer matrix. Core rods of ceramic-polymer mixtures were made by the pressing die as described in Part 1, Chapter 2, Section 2.1.2. There have been several ways to produce rod's covering materials, in which drilling and machining [57] and extrusion technique [66] are some of them. In the drilling method, the block of covering material is drilled to a diameter of rod material so that it can fit in. The core rod and covering sleeves were bonded with each other by the heat treatment. In the extrusion technique, cover materials are usually made up by a different step, using the extrusion method. Cover materials are hot mixed and extruded through a rectangular orifice to form a flat ribbon. Under a moderate heat treatment and a medium static press, this flat ribbon has the shape of a half circle which fits with a half of the feedrod circumference.

The co-extrusion is executed in the same way with extrusion, in which fibers of core-shell structure were driven out of the die orifice. Reduced-size core-shell structures will be rebundled and coextruded several times so that the number of fibers included in one filament is excessively increased while their diameters is dramatically decreased. The reduction of fiber diameter is usually in the range from 25 to 40 times

to its initial diameter [57]. The smallest fiber diameter of 65 μm was reported [60, 67]. The schematic illustration of this process is depicted in Fig. 7.18.

This strong ability of coextrusion method provided us a hope to tailor a fine texture of the core-shell structure in which the core is columns of Co_2Z particles aligned uniaxially. The target of formulating flexible anisotropic Co_2Z-PE would be achieved.

However, there are some challenges to make this technique unfeasible in synthesizing anisotropic dielectromagnetic Co_2Z-PE composites. Ceramic powders are always mixed with a thermoplastic polymer to form an isotropic material for extrusion process and there is a composition limit in the range 45 to 75 Vol%, depending nature of ceramics [60, 66, 68]. In our circumstance, this value is below 50 vol%. Coextrusion with a different material will further dilute ceramics compositions, which in turn, further separate their dielectric permittivity and magnetic permeability.

Another challenge of the coextrusion technique to our research is its ability to work on core-shell structure with the shell layer is a polymer. There will be a big difference of viscosity among core and shell layers, which would cause a mismatch or distortion in shape due to their different flow rates.

Therefore, experimental study the feasibility of coextrusion method in producing the Co_2Z-PE core-shell structure was conducted simultaneously with theoretical calculations to predicting the compatibility of dielectric permittivity and magnetic permeability of producing materials. The theoretical calculations will be described in Chapter 8 together with other calculations on different ferrites for the purpose of this research.

7.3.2. Experiment

7.3.2.1. Formation of feedrods

Low-density Polyethylene (LDPE) is used as the distributing medium for Co_2Z ceramics to produce the core material. Heavy mineral oil was used as lubricant to facilitate the dispersion of Co_2Z powder [69]. Polymer was firstly melted in the Plasti-Corder hot mixer. Ceramic powder and lubricant are gradually added while mixing was still in process until the torque value reaches to a stable value. In order to meet the intended Co_2Z composition, Co_2Z was used at highest amount in the core. Samples compositions were given in Table 4.5. Co_2Z consists of high density of 5.37 g/cm^3 and high viscosity of LDPE (96400 Pa.s) obstructed the formation of high filler composition samples with empirical value less than 50 vol%.

High-density Polyethylene (HDPE) was used as the covering material. In the preliminary experiments, we followed the extrusion technique with which, ribbons of HDPE were formed through extrusion. HDPE was melted at 130^oC inside the die in a high vacuum condition before being enforced through a rectangular orifice with dimension of 1×25.3 mm at speed 2 mm/min and a force of 17 kPa. The intended low extrusion speed was aimed to provide enough time for liquid HDPE quenched and solidified after going out of the die's opening. However, ribbons of HDPE were not able to form with the reasons from the complication of rheology of HDPE. As cooling rate at the edge of the ribbons faster than that in their internals, the material in the middle of ribbons was still flowable to form wavy shape while the material at the edges were solidified. Another factor was that, the shear rate at two small ends of the

151

die's opening was higher than that at two big edges [70] so that the material at those two end points formed with convexo-concave appearance. The different cooling rate would also contribute into this process. Other faster extrusion speeds resulted in necking and elongation of liquid HDPE at the opening, which in turn, did not provide enough material to form half circle covering sleeves.

A consistent method to make sleeves for core-shell structure was invented. HDPE was melted directly on reservoir of the female ram of the die which is used to form the concave shape of core's shell at $130^{o}C$ and a high vacuum condition. The amount of HDPE needed to make a complete circle core's shell was calculated and evenly sprinkled along the length of the die so that, when being statically pressed, an even thickness sleeve was formed. The die was opened and the material was released after it was quenched. The formed half a circle shell had both smooth surfaces and even thickness. Two half a circle shells were contacted with the core material from heat treatment to produce a complete core-shell feedrod.

7.3.2.2. Coextrusion and testing sample formation

The core-shell structure has a cylinder shape and the coextrusion was conducted through a die whose one end was heated to $130^{o}C$, the temperature at which PE was melted. The coextrusion would be in several steps with the first reduced-size rod diameter was 2.5 mm. Those reduced-size rods were rebundled for the second coextrusion to form multiple aligned elements fibers with diameter of 1mm. The number of fibers at this step was twenty five. A finer structure with a larger number

of filaments inside a fiber and a smaller fiber diameter could be achieved with a third coextrusion. We intended to conduct the coextrusion experiment triple to obtain 1 mm diameter assembly with the diameter of a singular filament would roughly about 40 μm. Co_2Z particles distribute along filament's length, which dependent upon the composition, can be considered as a dense or loose alignment.

The assembly with 1 mm diameter would be used to make testing sample. It was reheated to its melting temperature of PE and was wound around an axis to form disks of circles of fine structure assemblies. Flat surfaces of testing samples were made by pressing samples against two parallel flat surfaces at melting status of PE.

The permittivity and permeability measurements would also be similar to those conducted on the flexible moldable Co_2Z-PE samples. The predicting values of these two properties were obtained from calculation using the Jayasundere-Smith equation as described in chapter 3 of the second research topic:

$$\varepsilon_{eff} = \frac{\varepsilon_1 . \vartheta_1 + \varepsilon_2 . \vartheta_2 \left[\left(\frac{3.\varepsilon_2}{\varepsilon_1 + 2.\varepsilon_2} \right) \left(1 + 3.\vartheta_2 . \frac{\varepsilon_2 - \varepsilon_1}{\varepsilon_2 + 2.\varepsilon_1} \right) \right]}{\varepsilon_2 + \varepsilon_1 . \left[\left(\frac{3.\varepsilon_2}{\varepsilon_1 + 2.\varepsilon_2} \right) \left(1 + 3.\vartheta_2 . \frac{\vartheta_2 . \vartheta_1}{\varepsilon_2 + 2.\varepsilon_1} \right) \right]}$$

<div align="center">Jayasundere-Smith equation</div>

7.3.3. Results and Discussion

In order to succeed in producing core-shell structures with ceramic-polymer mixtures were used in both the core and the shell have to meet a critical condition in viscosity [68, 71]. In our research, we have discovered that, the coextrusion of a ceramics-

polymer and polymer core-shell system requires more critical conditions on rheological behavior, strength and immiscibility of two materials. The co-extrusion experiments conducted in this project faced a very critical challenge. The strength and viscosity of the core and shell materials were not comparable to each other. Images of extruded fibers were given in Fig. 7.19. An even diameter of core-shell structure was not achievable as well as the isolation between the core and shell materials.

For a number of researches to formulate the fibrous monolithic or core-shell structure composites, both the core and the shell materials were ceramics by the end of the process. Brady et al.[59], Popovich et al.[56], Baskaran et al. [63, 72-73] reported a variety of fibrous monolithic composites of oxides and non-oxides ceramics systems such as Al_2O_3/Ni-Cr alloy, Al_2O_3/C, Si_3N_4/BN, SiC/BN, and ZrO_2/Al_2O_3/NiO mono/multifilament fibers. Kaya et al. [60] and Miyazaki et al. [67] reported the formulation of ZrO_2/Al_2O_3 composites in which Kaya made them in a multilayer fibrous form whilst Miyazaki made them in an alternative structural fibers. Their research met the requirement of comparable viscosity of both materials. They mixed ceramic powders with a thermoplastic polymer, lubricants and dispersant agents so that they could control the viscosity of both materials. Polymers, by the end, were burned off to leave ceramics powders in a designed texture. The heat treatments afterward accompanied with high pressure produced dense materials without the miscibility of composite's components. The addition of ceramic powders into the polymer increased its strength and viscosity [70, 74-75] to a degree so that it minimized the shear stress on interfaces between materials and between material and die's wall to impact on the attachment of materials [76].

The coextrusion for a materials system in which one or both of them is/are polymers required a stricter conditions on strength and immiscibility, apart from others. The reason is that the melted polymer has lower viscosity and weaker. It is prone to be affected by shear stress more than ceramics-polymer systems. J. Dooley and L. Schkopau [77] conducted a research on coextrusion of several types of PE with different melting indexes, ranging from 0.5 to 8.0 g/10 min. They arranged materials in different orders: similar viscosity of PE and higher viscosity PE in the core. Their research results showed in Fig. 7.20 indicate the significance of equivalent viscosities to keep their interfaces not deformed. Their data shown in Fig. 7.21 show the lower viscosity polymer on the shell resulted in a bad interface deformation. This phenomenon was very similar to our case, where the low viscosity HDPE was used as the shell material while the high viscosity Co_2Z-LDPE was used as the core material. In addition, those images also indicate the effect of die's geometry on the interface deformation of two coextruded polymers.

According to Dooley and Schkopau, there presents viscous and elastic flows corresponding to viscous and elastic forces occurred during coextrusion. The viscous force and viscous flow appear in radial symmetric geometry die's opening, due to the difference of viscosities, which in turn, results in the encapsulation phenomenon as seen in Fig. 7.21a. This phenomenon happens in the case a lower viscosity fluid is a cap for higher viscosity fluid. This also relates to the comparative strengths of two fluids. They observed the interface deformation in the case using square die's opening and argued that that was caused from the elastic flow when they flow through a nonradially symmetric geometry. This elastic flow generated a local circular

155

movement inside polymer's body to make the deformation more critical. The research of Dooley and Schkopau was similar to that of Jones and colleagues [71].

Perez and Collier [70], and Gildengorn [78] investigated the influence of fluid's strength on their shape deformations at the outlet opening. Assuming the flow of two different strength fluids inside the die is steady, the extrusion is through a cone die, and their deformations are plastic, they applied the finite element method to simulate the shear stress distribution at the cone die. Consider the situation in which the fluid in the core has a higher strength than the sleeve fluid does, the weaker material tends to deform first under the pressure to move toward the die outlet. The stronger fluid tends to prevent this movement by applying stress on the weaker to make it deformed. In return, the deformation of the weaker fluid generates a stress on the harder fluid along their interface, forcing it to deform. Authors believed that there is a critical strength ratio between two fluids which in any case the strength ratio stays beyond this value will cause the uncontrollable flow of materials. The harder material goes out first with a very thin layer or a softer material covering its surface. The accumulation of the softer material, after meeting enough stress, will burst a force against the harder one, resulting the thinning of the harder material, even separating its flow. The accumulation also breaks the steady movement of material to form fibers in varying thickness and shape [79-80].

We found this argument suitable to explain our empirical results as shown in Fig. 7.19. The fiber has a varied diameter with an odd shape: straight at some segments, but wavy in some other segments. Due to the accumulation of HDPE and due to the miscibility of PEs in the core and in the shell, they mixed with each other in a way

that the core and shell's isolation was not detectable. This phenomenon did not happen in research of Brady et al.[59], Popovich et al. [68], Baskaran et al. [63, 72-73], or Kaya et al. [60] and Miyazaki et al. [67] because the material in the core and in the shell were all mixtures of ceramic powders and a polymer. Their strengths were comparable or at least lower than the critical strength ratio. In order to obtain a better core-shell structure, the viscosity of HDPE in the shell must be improved or its strength must be enhanced.

There are several options to modify viscosity of PE which are included (i) supplementation of high viscosity polymer or fillers [75] and (ii) keeping the working temperature close to glass point of polymer [81]. Jana and Nando added Polydimethylesilosane Rubber (PDMS) whose viscosity is 300 Pa.s into LDPE whose viscosity is 100 Pa.s at the same temperature $160^{o}C$ and shear rate of 631.2 cm^{-1} to observe a slower flow of LDPE. This concept is theoretically applicable if two components can mix to form a miscible mixture. In their research, they needed to add a compatibilizer, named Ethyl Methacrylate (EMA) to mitigate the difference of molecular structures between PDMS and LDPE. EMA improved the compatibility of PDMS to LDPE [82]. Given the polarization and high dielectric permittivity ($\varepsilon' = 6.0$) of EMA, the application of PDMS is not realistic in our material system because EMA would increase dielectric permittivity of the whole system, a matter that we had tried to avoid.

After being melted, viscosity of polymers decreases exponentially with the increment of temperature, according to Arrhenius law:

$$\eta = A.e^{E/RT}$$

Where A is the pre-exponential factor, E is the activation energy; R and T are molar gas constant and absolute temperature, correspondingly.

The rheological behaviors of PE were depicted in paper of Dobrescu and Radovici [81] show that PE at temperature slightly contains high viscosity and it rapidly decreased at higher temperatures. It was shown in their reports that this property of LDPE was more apparent than that of HDPE.

In the mean time, lowering down the applied pressure reduces shear rate of melted polymer, which in turn, increases its viscosity [83]. These techniques required the combination of temperature and co-extrusion speed adjustments to balance the viscosity of both materials in the shell and in the core. To some extent, they worked in our experiments to reduce the diameter variation of the formed rods. However, due to the low thermal conductivity of PE, the material going out of the die still retains its liquid state. As a consequence, material is stretched and thinned under the gravity. This phenomenon is serious because it does not allow producing a long and even core-shell structure. The slow quenching of material after going out of the die, together with its accumulated weight along with the extrusion time consequence in distortion of fiber as being depicted in Fig. 7.22. According to Timothy and White [84], this extrudate distortion was caused by the instability of melted polymers. Melted PE has been found as a non Newtonian fluid whose viscosity strongly dependent upon the normal stress difference measured in shear.

When processing temperature was set closer to melting point of polyethylene, viscosity of ceramic-LDPE mixtures increased so that their difference would not change. Furthermore, working at this temperature range made melted PE harder to move and required higher force load to be pushed out of the die. Shear stress applied on material's system and shear rate of material extruded out of the die were all increased. Under high pressure, the ceramic composition at layers close to die wall varies unexpectedly and unpredictably. However, from capillary rheological investigation, they discovered the change of movement velocity of polymer going out of the die, not linearly dependent upon the applied pressure with the presence of this wall shear stress. They investigated materials inside the die to find that they isolated themselves in three layers and each layer moves with a different mechanism. The movement of closest and third layers to the wall follows the exponential mechanism, while that of the second layer is linearly correlated with applied stress [85]. It is apparent that when materials in this research moved from isotropic diameter die to conical collector, a detachable part to reduce diameter of fiber, the slip flow induced to make fractured shape of material.

There would be another methodology to match the viscosity and strength of two materials, e.g. adding lubricants into Co_2Z-LDPE mixtures to lower its viscosity or adding silica powder into HDPE to increase its viscosity. However, data from theoretical calculation showed that the equivalent permittivity and permeability Co_2Z-LDPE/HDPE core-shell structure is not attainable as described in Chapter 5. Therefore, we stopped research on applying the coextrusion technique for the purpose of this study.

7.3.4. Remarks on coextrusion method

The coextrusion of a core-shell structure in which the core material was a mixture of Co_2Z-LDPE and the shell material was a pure HDPE polymer faced challenges of viscosity mismatch, too high core/shell strength ratio and miscibility of polymers used in the core and the shell. These challenges caused the flow of the whole system was not stable due to the accumulation of stress inside the shell HDPE body, which in turn, caused a shape variation of extruded material. Under a high stress, together with miscibility property, a majority of HDPE in the shell mixed with the mixture of Co_2Z-LDPE. A part of it covered and formed a smooth and transparent surface on Co_2Z-PE fiber while the rest stayed separately.

A number of modification techniques were applied, such as adding mineral oil into HDPE, lowering the processing temperature, lowering the pressure with the aim to improve the viscosity and strength of HDPE. However, none of them really worked. There would be other tactics of lowering the viscosity of core material by the addition of a lubricant inside core material. There would also another tactic to increase the viscosity of HDPE by an addition of ceramic powder into HDPE. Those chemicals must have similar dielectric properties to those of PE. However, due to the limit of Co_2Z compositions and its natural dielectric and magnetic properties, the equivalent permittivity and permeability Co_2Z-PE core-shell structures were not theoretically attainable.

Though coextrusion method is a convenient and controllable technique for the formation of uniaxial aligned Co_2Z particles, it was postponed to look for a high permeability ceramic material.
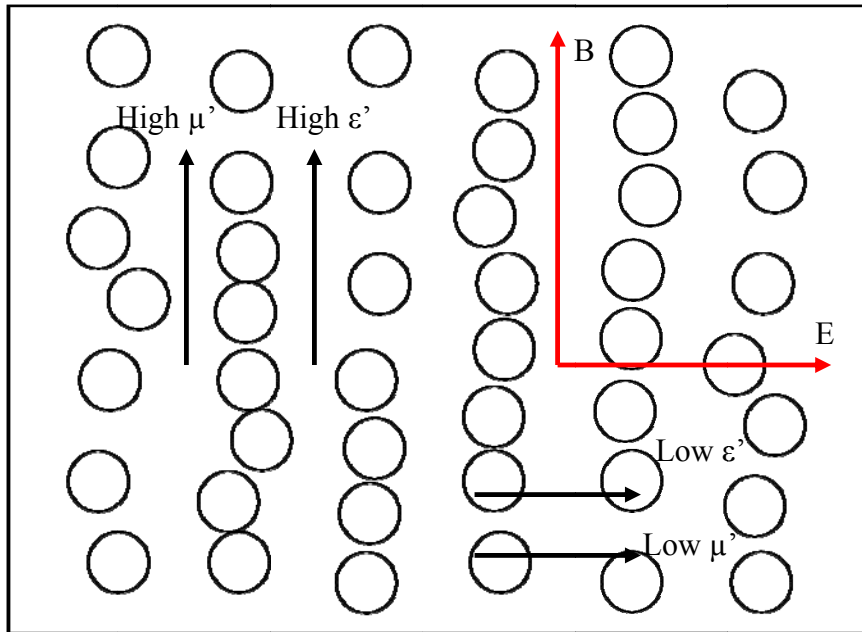
Fig. 7.1: Schematic illustration of the arrangement so that the magnetic field generated from the antenna senses high μ' direction and the electric field generated from the antenna sense low ε' direction.
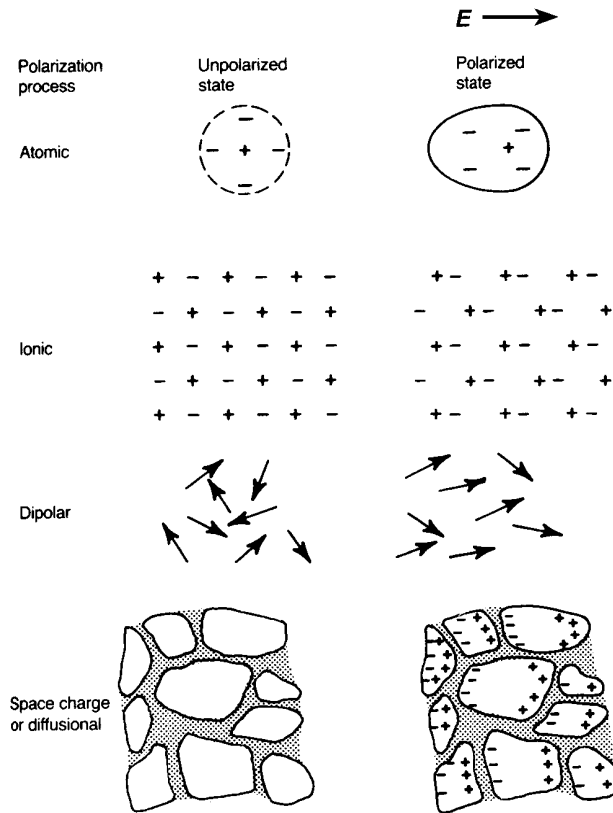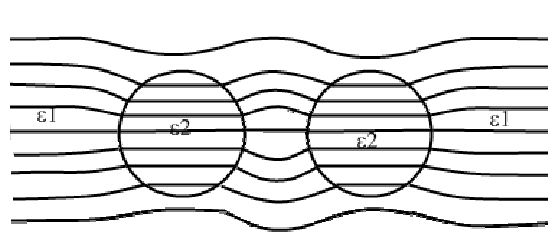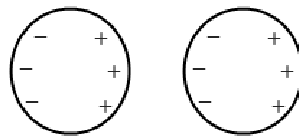

Fig. 7.2: Schematic illustration the polarization regimes

Table 7.1: The dielectrophoretic force for various combinations of dielectric permittivity with the assumption that volume and electric field are kept unchanged

Inclusions permittivity	Medium permittivity	$K_1[(K_2-K_1)/(K_2+2K_1)]$
2	1	0.25
4000	1	0.99
4000	2	2.00
20	15	1.50
2	20	-8.57
80	20	10
160	40	80

(a)

(b)

Fig. 7.3: The deflection of electric field lines at the interface of medium and inclusions and the formation of induced attractive force between particles (a). Under the influence of the electric field, polarization occurred inside particles (b)

Table 7.2: Calculations of forces impact on dielectric particles with the presence of an electric field (E = 3kV/cm, η = 750 cPs, T = 353 K)

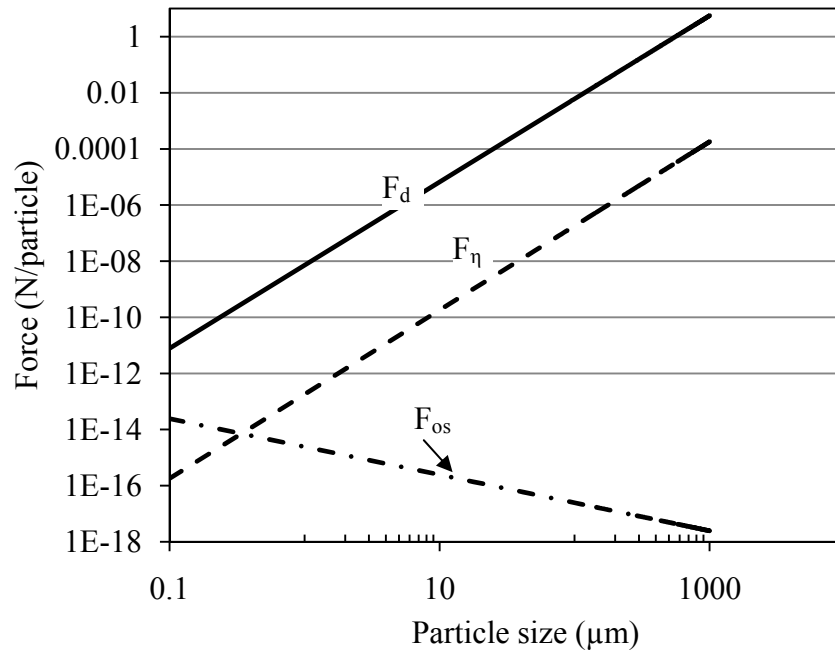| Particle size (μm)	F_d (N/particle)	F_{os} (N/particle)	F_η (N/particle)
0.1	5.03E-12	2.44E-14	1.80E-16
0.5	6.29E-10	4.87E-15	2.25E-14
1	5.03E-09	2.44E-15	1.79E-13
2	4.02E-07	1.22E-15	1.44E-12
5	6.28E-07	4.87E-16	2.25E-11
10	5.03E-06	2.44E-16	1.79E-10
100	5.03E-03	2.44E-17	1.79E-07
1000	5.03E+00	2.44E-18	1.79E-04

Fig. 7.4: Comparison of forces interacted with dielectric particles in the presence of an electric field. The dielectrophoretic force was dominant to others.
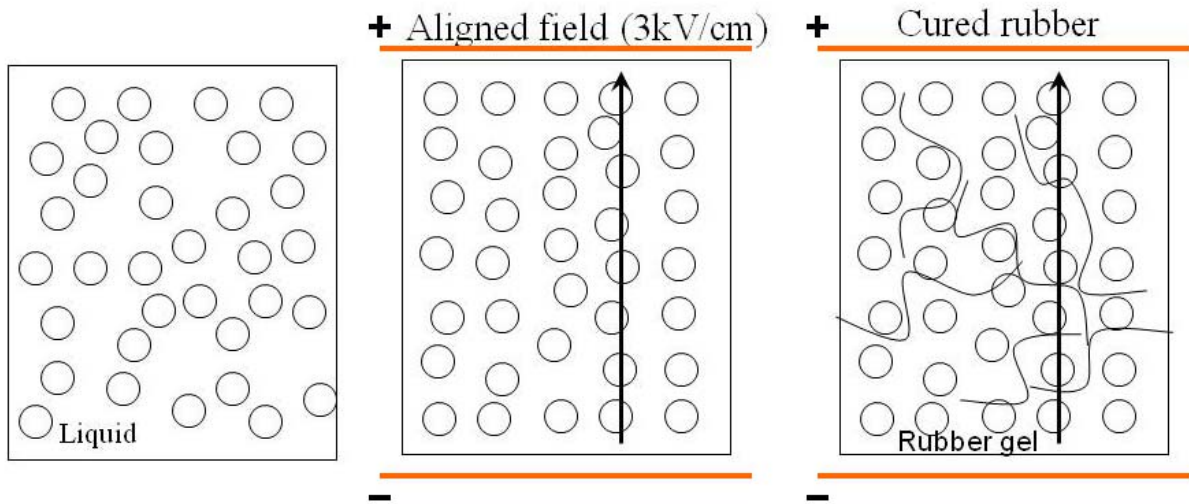
Fig. 7.5: Microstructural illustration of stages of dielectrophoresis. Before being solidified, particles distribute randomly in the whole volume. Under the electric field, they align along the field lines and retain their positions after polymers harden

Table 7.3: Properties of uncured silicone rubber as catalyzed 1:1 by weight

	Look	Viscosity	Specific gravity	Useful T^oF	Reflective index	Dielectric constant (1kHz)	delta (1kHz)	R (Ohm)
RTV 6166	Clear, colorless	750 cps	0.98 g/cm^3	-50 to 204	1.41	2.8	10^{-3}	10^{15}

Table 7.4: Compositions of samples for dielectrophoretic experiments

	Sample 1	Sample 2	Sample 3	Sample 4	Sample 5
Co$_2$Z (Vol%)	10	20	30	40	45
RTV6166 (Vol%)	85	75	65	55	50
Mineral oil (Vol%)	5	5	5	5	5

Fig. 7.6: Mixing bag. The ferrites were mixed with RTV 6166 A and B in two different bags after being vacuumed to vacuum degree of 10^{-3} tor
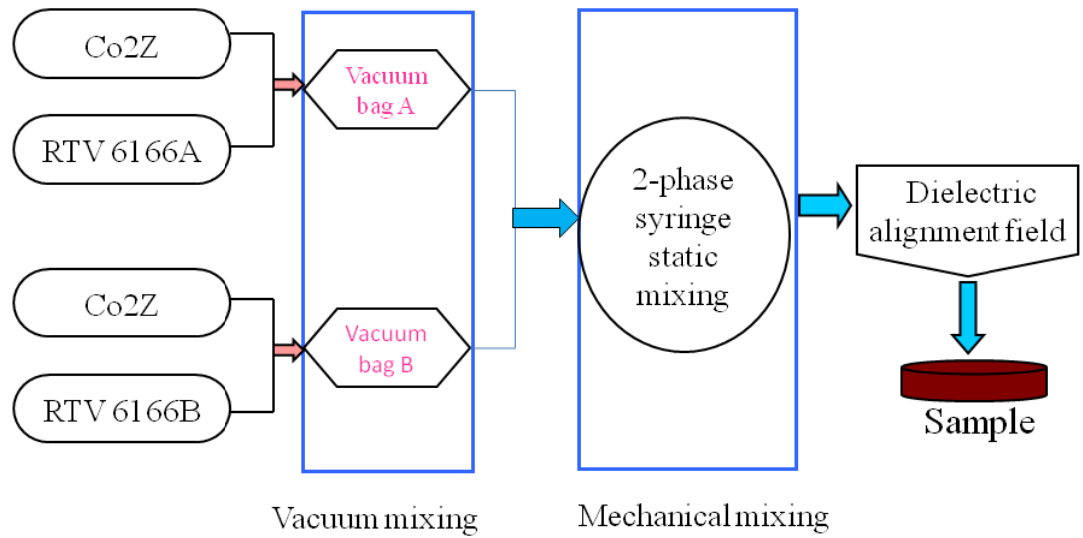

Fig. 7.7: Schematic of experimental procedure using dielectrophoresis technique

Sample chamber inside curing bath

Transformers to produce high voltage

Thermocouple with moniter

Alternative electric field: 3kV/cm under two different frequencies 60 Hz and 1 kHz
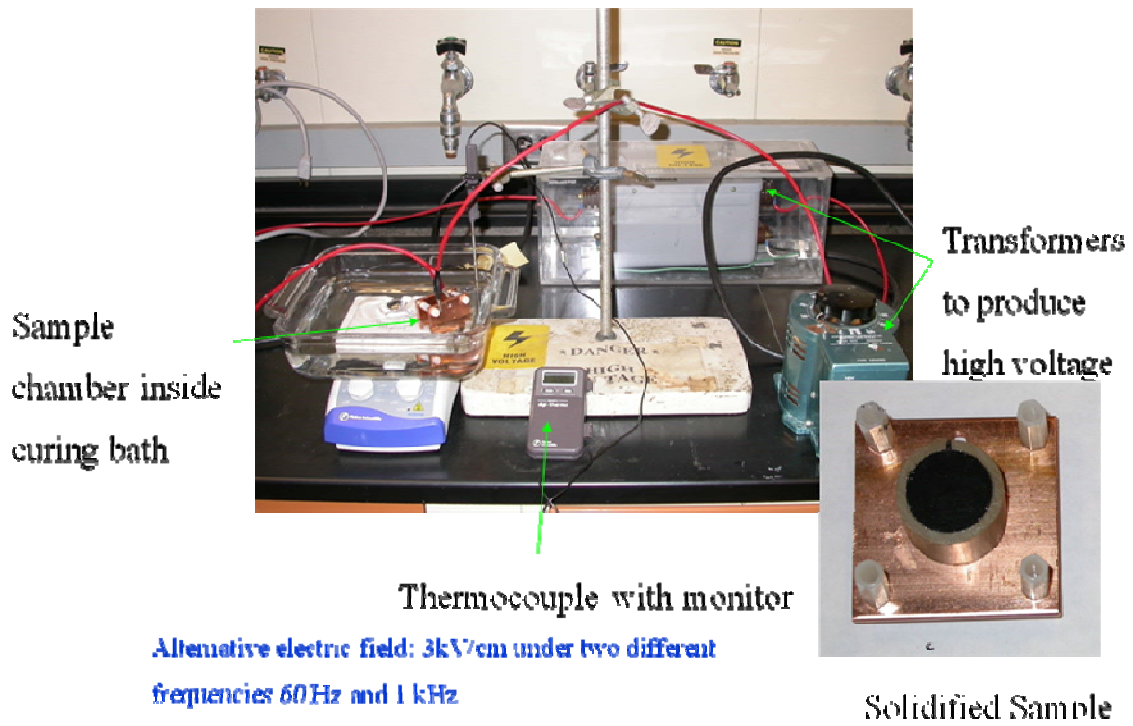
Solidified Sample

Fig. 7.8: Experimental equipments and sample in sample holder after being solidified.

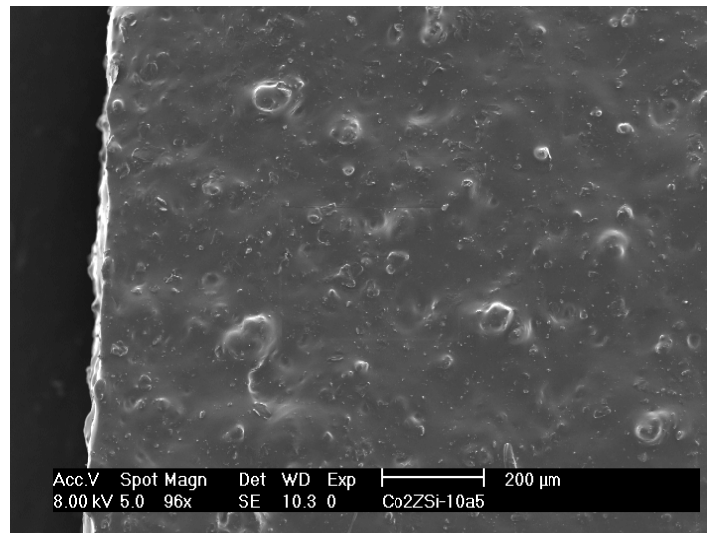| Acc.V | Spot | Magn | Det | WD | Exp | ⊢——— 200 µm |
| 8.00 kV | 5.0 | 96x | SE | 10.3 | 0 | Co2ZSi-10a5 |

Fig. 7.9a: Microstructure of 10 vol% Co_2Z-Silicone composite at its cross section after dielectrophoretic experiment showing the even distribution of inclusions
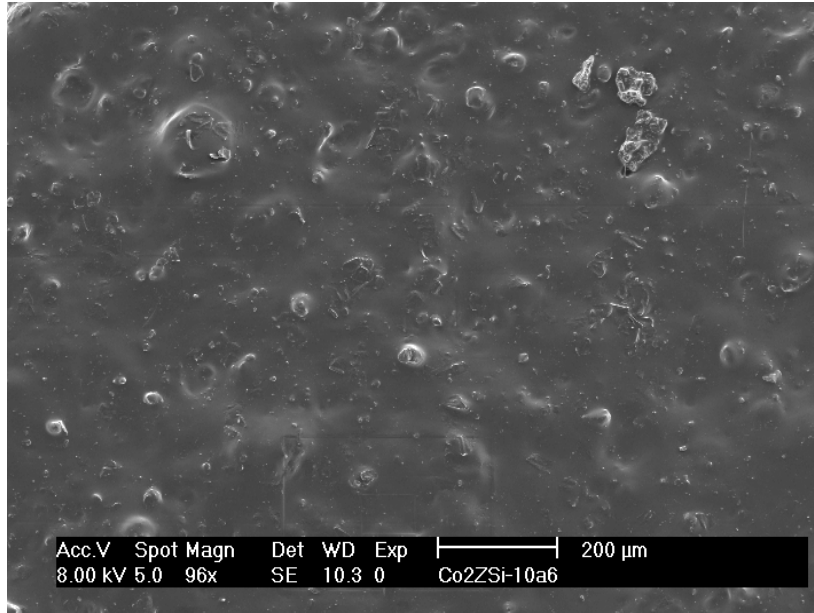
167

Fig. 7.9b: Microstructure of 10 Vol% Co2Z-Silicone composite at its cross section after dielectrophoretic experiment.
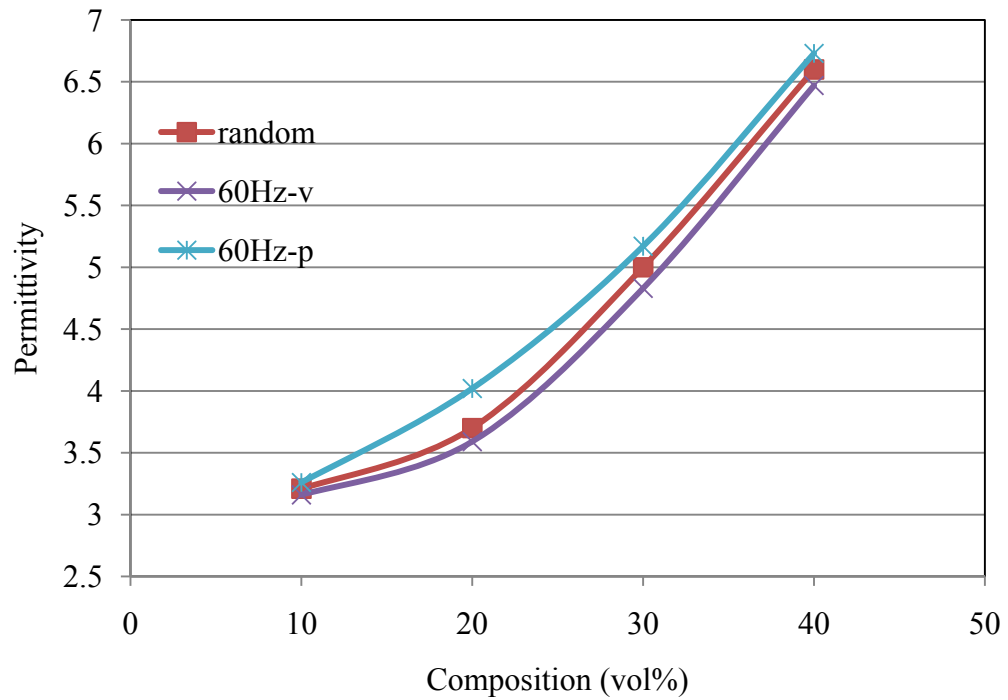
Fig. 7.10: Permittivity of samples annealed at field strength of 3kV/m, 60 Hz

Fig. 7.11: Permittivity of samples annealed at field strength of 3kV/m, 1 kHz

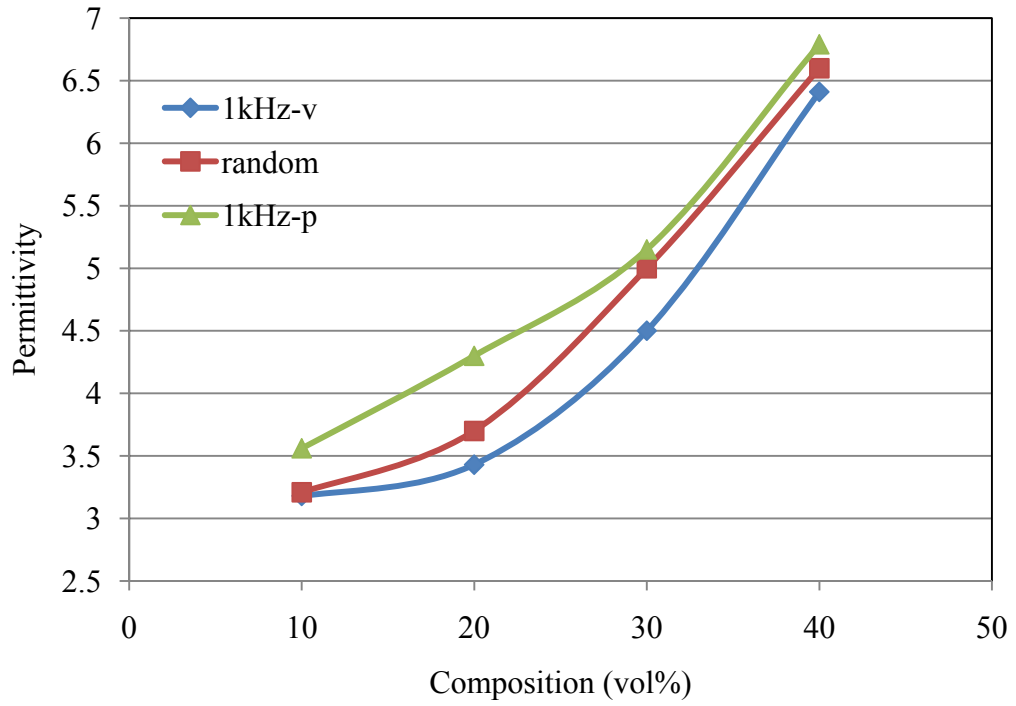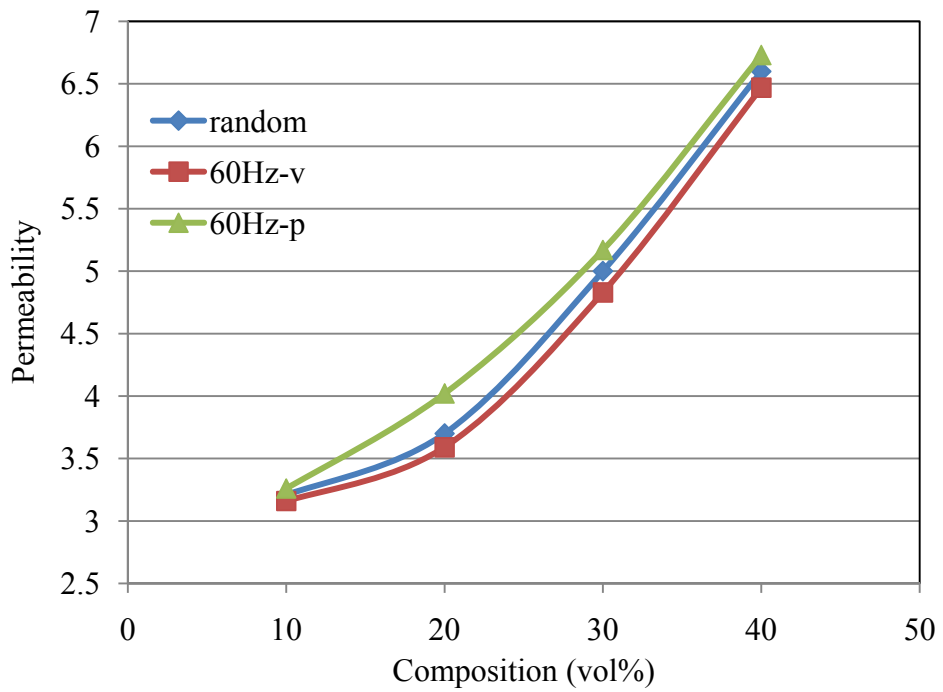**Fig. 7.12:** Permeability of samples annealed at field strength of 3kV/m, 60 Hz
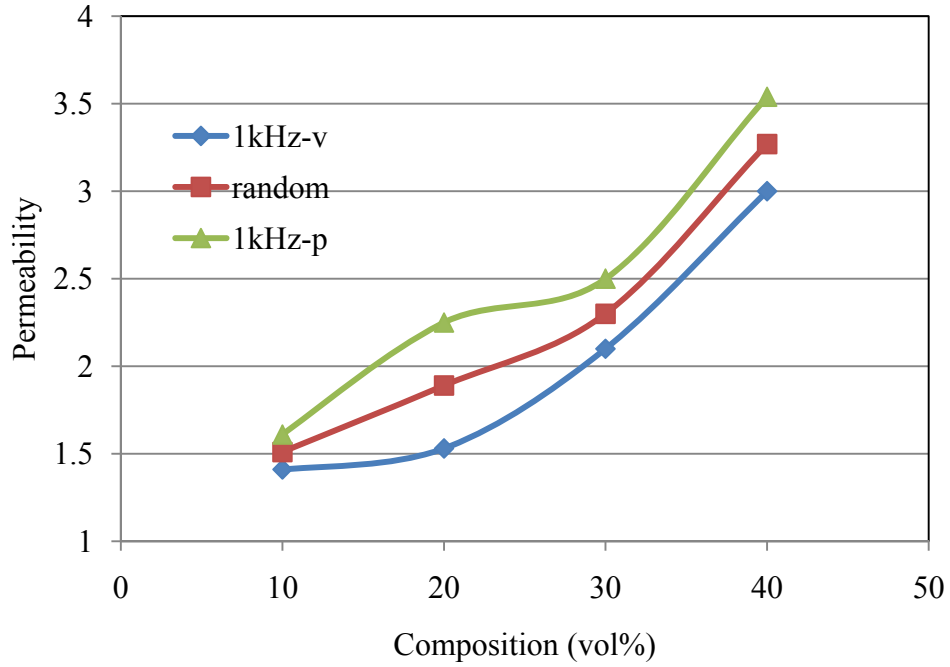
Fig. 7.13: Permeability of samples annealed at field strength of 3kV/m, 1 kHz

Parallel permittivity: ε_p
Vertical permittivity:
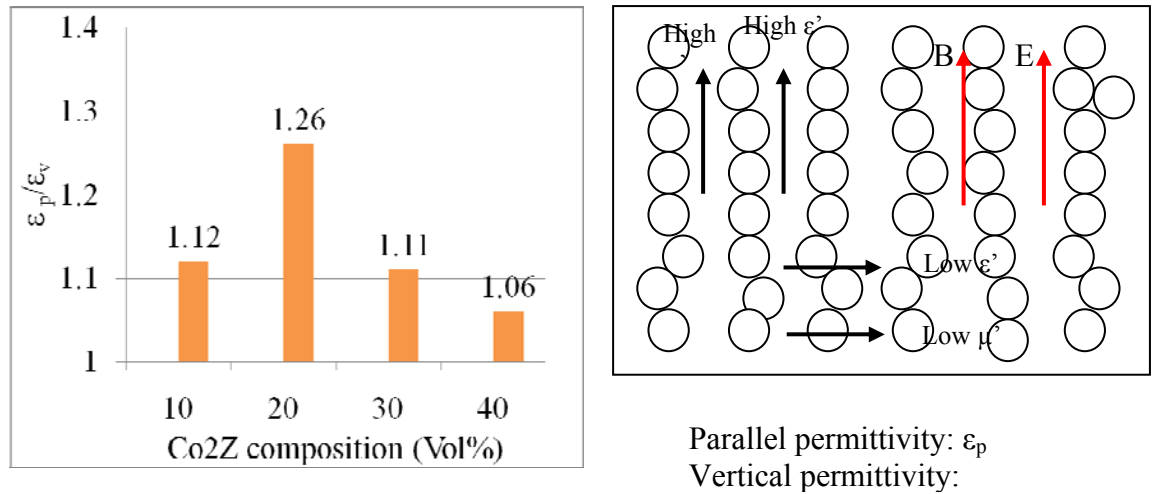
Fig. 7.14: The ratio between dielectric permittivity parallel to the electric field and that perpendicular to the electric field. B and E represent for the measurement magnetic and electric fields.
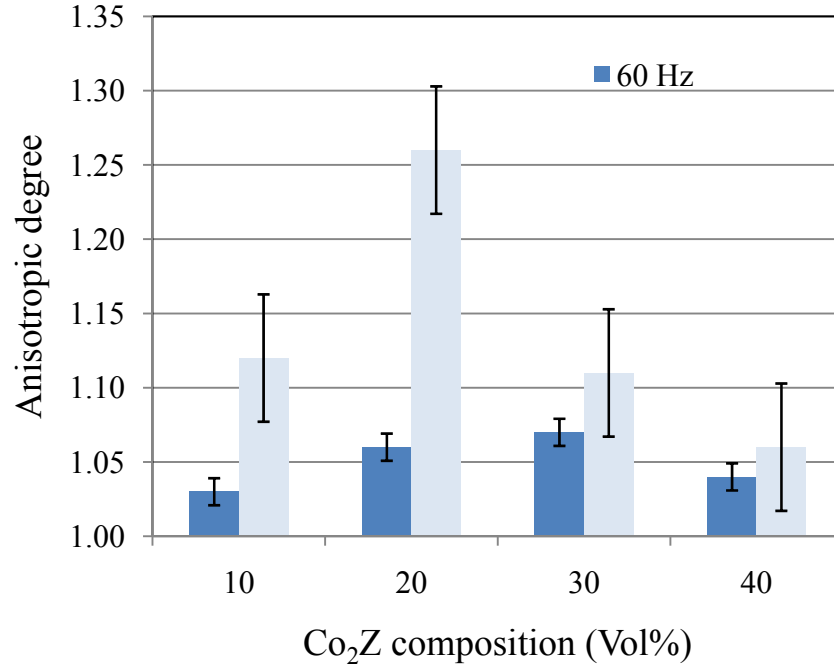
Fig. 7.15: The ratio of dielectric permittivity between parallel and perpendicular directions to the electric field, E=3kV/cm, f_1 = 1 kHz (red columns) and f_2=60 Hz (black columns), t= 80°C
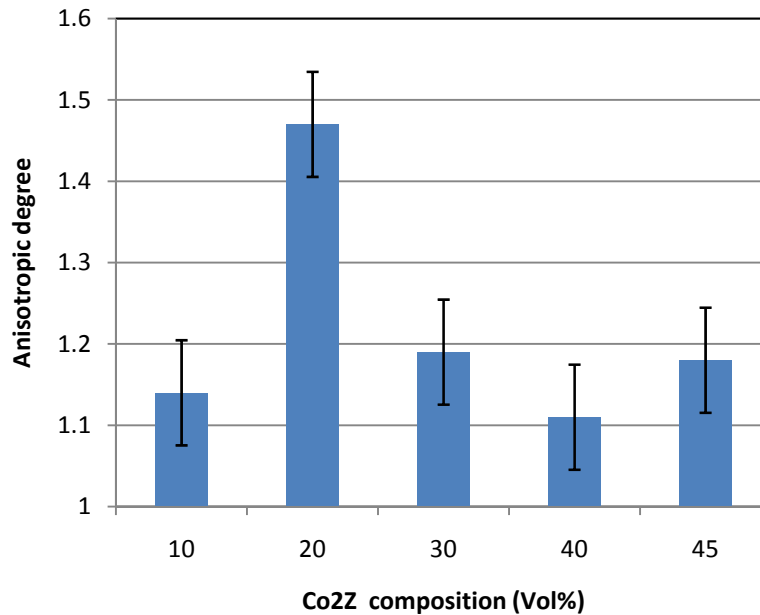
Fig. 7.16: The ratio of magnetic permeability between parallel and perpendicular directions to electric field, E=3kV/cm, f = 1 kHz, t= 80°C
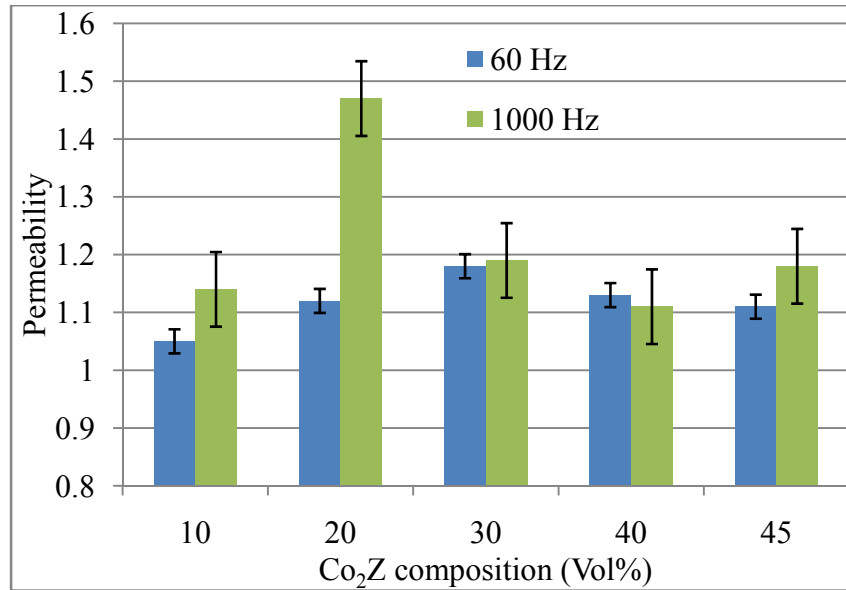
Fig. 7.17: The ratio of magnetic permeability between parallel and perpendicular directions to the electric field, E=3kV/cm, f_1 = 1 kHz (green columns) and f_2=60 Hz (yellow columns) , t= 80°C

Type I) Weak interaction of polarized particles

Type II) Randomly located 'pearl chains'

Type III) Chains aggregate into 'columns'
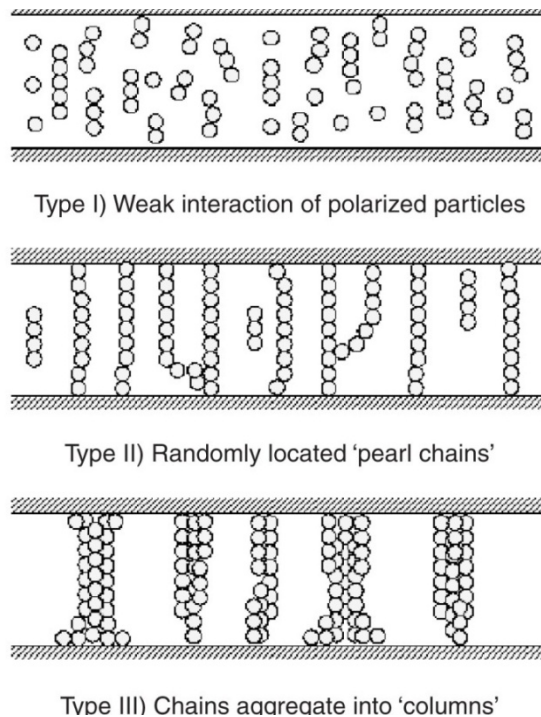
Fig. 7.18: Three observed types of alignment of piezoelectric ceramic particles under the effect of electric field [25]

172
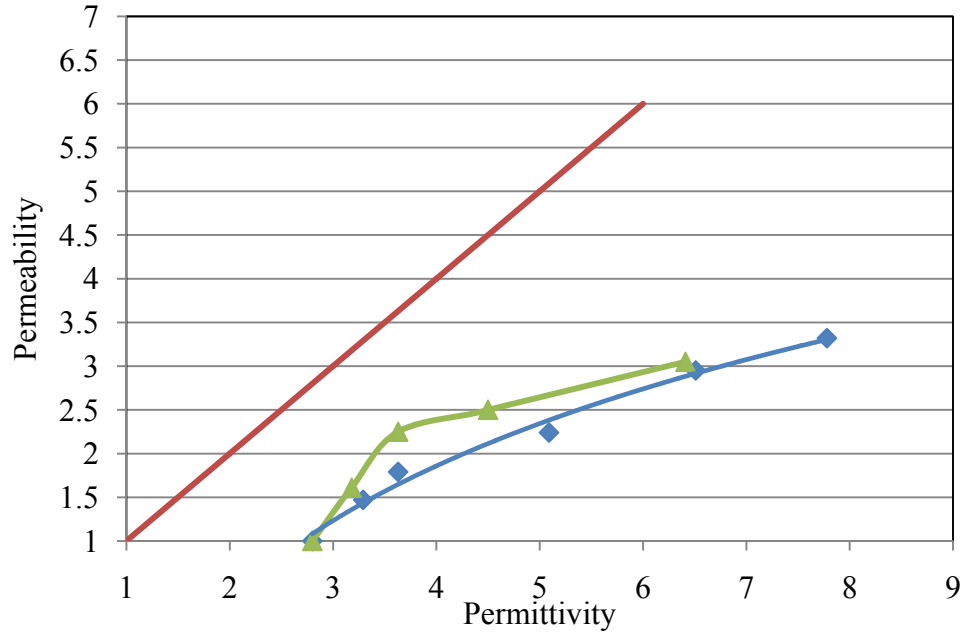
Fig. 7.19: Improved permittivity and permeability relationship by dielectrophoresis alignment method in comparison with that of the isotropic Co_2Z-LDPE
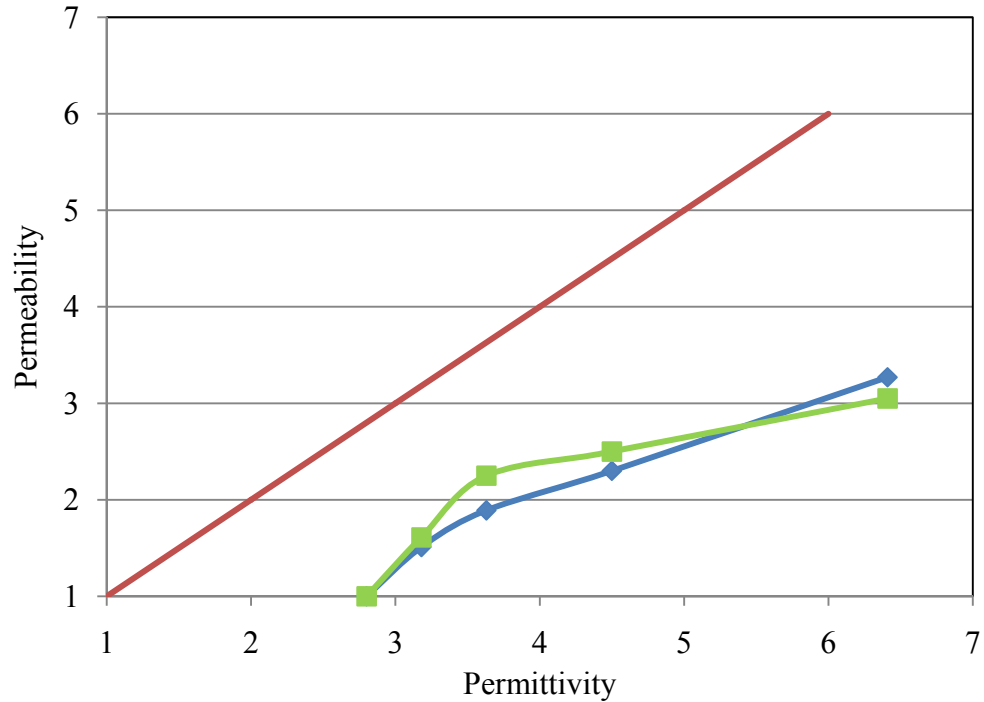
Fig. 7.20: Improved permittivity and permeability relationship by dielectrophoresis alignment method in comparison with that of the isotropic Co_2Z-Silicone elastomer
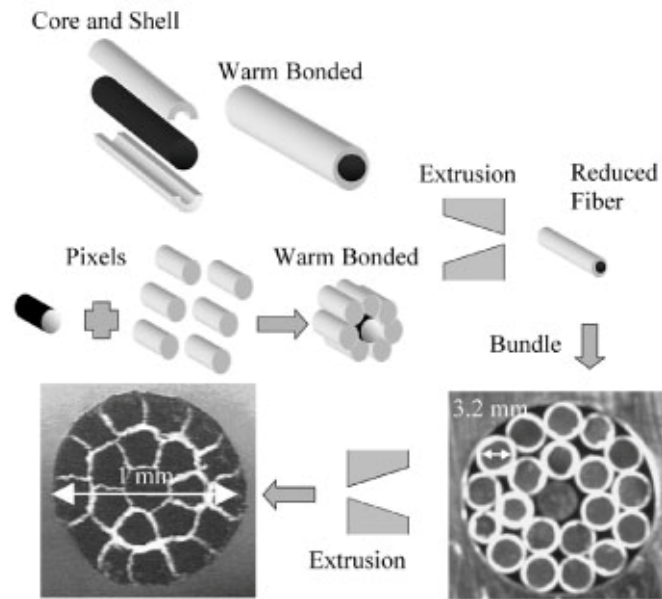
Fig. 7.21: Schematic illustration of coextrusion techniques with details of steps [57]

Table 7.5: Intended and used composition of the core material

Intended vol%	10	20	30	40	45
Used Co$_2$Z vol%	11.92	24.49	37.06	49.63	55.91
Used LDPE vol%	83.08	70.51	57.94	45.37	39.09
Mineral oil	5	5	5	5	5

Fig. 7.22: Co$_2$Z-LDPE/HDPE fibers after coextrusion to show a distorted shape due to the unsteady movement of materials inside the die

(a)

(b)
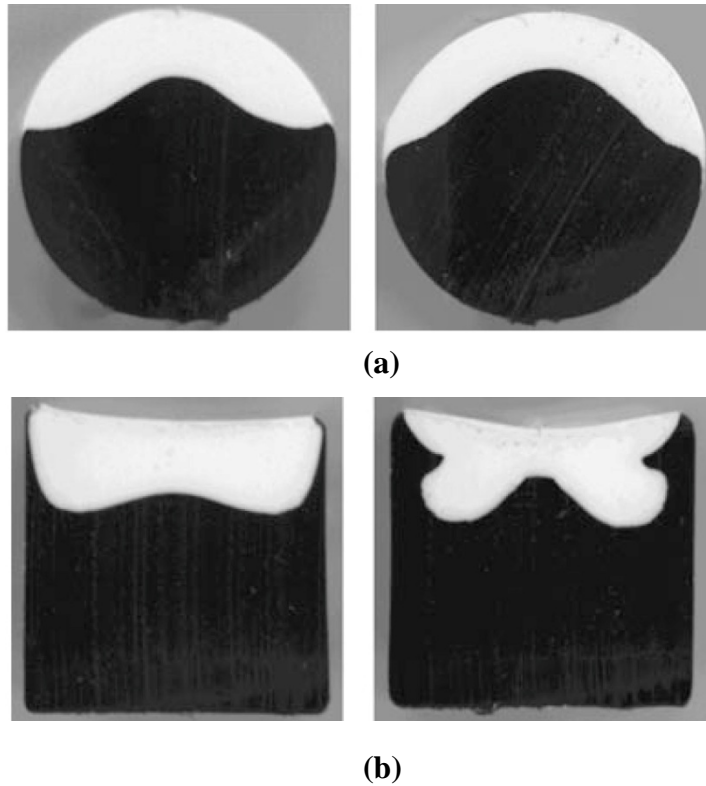
Fig. 7.23: The distortion of PE's interface of PEs having similar viscosity in different die geometries: (a) less distortion through a circular channel, (b) severe distortion through a square channel [77]
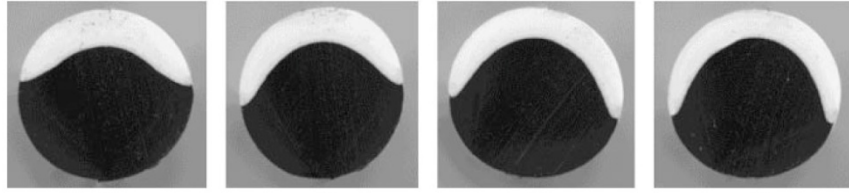
(a)
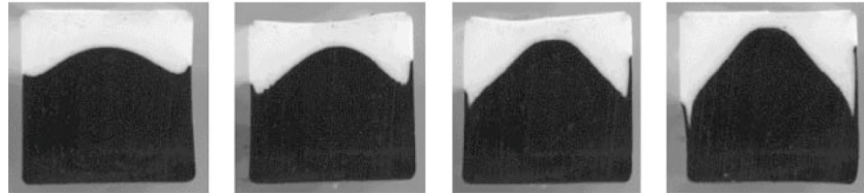
(b)

Fig. 7.24: The distortion of PE's interface of PEs having different viscosities in different die geometries: (a) severe distortion through a circular channel, (b) severe distortion through a square channel [77]

References

1.	H.A.Pohl, ed. *Dielectrophoresis: Behavior of Neutral Matter in Nonuniform Electric Fields*. 1978, Cambridge University Press.

2.	M. Hase, M. Egashira, and N. Shinya, *Development of Novel Method to Create Three-Dimentional Arrangements of Partcles using Dielectrophoresis in Artificially Nonuniform Electric Field*. Journal of Intelligent Materials System and Structures, 1999. **10**(July): p. 5.

3.	H.C. Pant, M.K. Patra, A. Verma, S.R. Vadera, N. Kumar, *Study of the Dielectric Properties of Barium Titanate-Polymer Composite*. Acta Materialia, 2006. **54**: p. 6.

4.	C. Park, and R. Robertson, *Alignment of Particles by An Electric Field*. Materials Science and Engineering, 1998. **A 257**: p. 295-301.

5.	C. Park, and R. Robertson, *Aligned Microstructure of Some Particulate Polymer Composites Obtained with an Electric Field*. Journal of Materials Science, 1998. **33**: p. 3541-3553.

6.	C. Park, R. Robertson, *Mechanical Properties of Resin Composites with Filler Particles Aligned by and Electric Field* Dental Materials, 1998. **14**(November): p. 385-397.

7.	L. Dong, J. Bush, V. Chirayo, R. Solanki, J. Jiao, Y. Ono, J.F. Conley Jr., and B.D. Ulrich, *Dielectrophoretically Controlled Fabrication of Single-Crystal Nickel Silicide Nanowire Interconnects*. Nano Letters, 2005. **5**(10): p. 3.

8.	M.P.Hughes, *AC Electrokinetics: Applications for Nanotechnology*. Nanotechnology, 2000. **11**: p. 124-132.

9.	T.H.Kim, S.Y.Lee, N.K.Cho, H.K.Seong, H.J.Choi, S.W.Jung, S.K.Lee, *Dielectrophoretic Alignment of Gallium Nitride Nanowires (GaN NWs) for Use in Devicce Applications*. Nanotechnology, 2006. **17**: p. 3394-3399.

10.	H.Fudouzi, M.Kobayashi, N. Shinya, *Assembling 100nm Scale Paricles by an Electrostatic Potential Field*. Jour of Nanoparticle Research, 2001. **3**: p. 193-200.

11.	R. Pethig, G.H. Markx, *Applications of Dielectrophoresis in Biotechnology*. TIB Technology, 1997. **15**(October): p. 6.

12.	R.Pethig, *Dielectrophoresis: Using Inhomogeneous AC Electrical Fields to Separate and Manipulate Cells*. Critical Reviews in Biotechnology, 1996. **16**(4): p. 331-348.

13.	J. Kadaksham, P. Singh, N. Aubry, *Dielectrophoresis Induced Clustering Regimes of Viable Yeast Cells*. Electrophoresis, 2005. **26**: p. 3738-3744.

14.	Y.Huang, X.B.Wang, J.A.Tame, R.Pethig, *Electrokinetic Behaviour of Colloidal Particles in Travelling Electric Fields: Studies Using Yeast Cells*. Journal of Physics D: Applied Physics, 1993. **26**: p. 1528-1535.

15.	Y.Kang, L.Dong, S.A.Kalam, J.E.Eid, *DC-Dielectrophoretic Separation of Biological Cells by Size*. Biomed Microdevices, 2008. **10**: p. 243-249.

16.	A.T.J.Kadaksham, P. Singh, N. Aubry, *Dielectrophoresis of Nanoparticles*. Electrophoresis, 2004. **25**: p. 3625-3632.

17. T.Miloh, *Dipolophoresis of Nanoparticles.* Physics of Fluids, 2008. **20**: p. 063303.

18. V.N.Shilov, *Dielectrophoresis of Nanosized Particle.* Colloid Journal, 2007. **70**(4): p. 515-528.

19. W.T.Winter, M.E.Welland, *Dielectrophoresis of Non-spherical Particles.* Journal of Physics D: Applied Physics, 2009. **42**: p. 045501.

20. Wing, Zach, *Fabrication and Characterization of Effective Medium Meta-Dielectrics*, in *Materials Science and Engineering*. 2005, University of Michigan: Ann Arbor. p. 204.

21. Goru, R., ed. *Dielectrics in Electric Fields*. 2006, Elsevier.

22. T.B.Jones, ed. *Electromechanics of Particles*. 1995, Cambridge University Press. 16-28, 139-177, 1217-1228.

23. N. Aubry, P. Singh, *Control of Electrostatic Particle-Particle Interactions in Dielectrophoresis.* Europhysics Letters, 2006. **74**(4): p. 623-629.

24. H.C.Hillborg, *Loss and Recovery of Hydrophobicity of Polydimethylsiloxane After Exposure to Electrical Discharges*, in *Department of Polymer Technology*. 2001, Royal Institute of Technology: Stockholm. p. 77.

25. S.A. Wilson, G.M. Maistros, and R.W. Whatmore, *Structure Modification of 0-3 Piezoelectric Ceramic/Polymer Composites through Dielectrohporesis.* Journal of Physics D: Applied Physics, 2005. **38**: p. 7.

26. S.D. Cho, S.Y. Lee, J.G. Huyn, and K.W. Paik, *Comparison of Theoretical Predictions and Experimental Values of the Dielectric Constant of Epoxy/BaTiO3 Composite Embeded Capacitor Films.* Journal of Materials Science: Materials in Electrionics, 2005. **16**: p. 7.

27. S. Kholouridis, G. Kiziltas, Y. Zhow, D. J. Hansford, and J.L. Volakis, *Polymer-Ceramic Composites for Microwave Applications: Fabrication and Performance Assessment.* IEEE Transactions on Microwave Theory and Techniques, 2006: p. 7.

28. S.C.Nudurupati, N.Aubry, D.Papageorgiou, P.Petropoulos, *Monodisperse Drop Formation in Square Microchannels.* Physical Review Letters, 2006. **96**: p. 144501.

29. C.P.Bowen, A.S. Bhalla, R.E.Newnham, C.A.Randall, *An Investigaion of the Assembly Conditions of Dielectrics Particles in Uncured Thermoset Polymers.* Journal of Materials Research, 1994. **9**(3): p. 781-788.

30. U.Mario, S.Elisabeth, *Multiple Frequenc Dielectrophoresis.* Electrophoresis, 2007. **28**: p. 3145-3155.

31. C.A.Randall, J.Van Tassel, M.Matsko, C.P.Bowen. *Electric Field Processing of Ferroelectric Particulate Ceramics and Composites*. in *The Tenth IEEE International Symposium on Applications of Ferroelectrics*. 1996.

32. M.Dimaki, P.Boggild, *Frequency Dependence of the Structure and Electrical Behaviour of Carbon Nanotube Networks Assembled by Dielectrophoresis.* Nanotechnology, 2005. **16**: p. 759-763.

33. C.A.Randall, S.Miyazaki, K.L.More, A.S.Bhalla, R.E.Newnham, *Structural-property Relationships in Dielectrophoretically Assembled BaTiO3 Nanocomposites.* Materials Letters, 1992. **15**: p. 26-30

34. A. Knapp, J.W. Halloran, *Characterization of Thermoplastic Blends as Binder for Ceramics.* Journal of American Ceramic Society, 2006. **89**(10): p. 3010-3018.

35. C.A.Randall, D.V.Miller, J.H.Adair, A.S.Bhalla, *Processing of Electroceramic-Polymer Composites using the Electrorheological Effect.* Journal of Materials Research, 1992. **8**(4): p. 899-904.

36. L.C.Davis, *Finite-Element Analysis of Particle-Particle Forces in Electrorheological Fluids.* Applied Physical Letters, 1992. **60**(3): p. 319-321.

37. N. Aubry, P. Singh, *Influence of Particle-Particle Interactions and Particles Rotational Motion in Traveling Wave Dielectrophoresis.* Electrophoresis, 2006. **27**: p. 703-715.

38. M.Hase, M.Egashira, N.Shinya, *Development of Novel Method to Create Three-Dimensional Arrangements of Particles Using Dielectrophoresis in Artificially Nonuniform Electric Field.* Journal of Intelligent Material Systems and Structures, 1999. **10**: p. 508-515.

39. C.P.Bowen, R.E.Newnham, C.A.Randall. *The Effect of Dielectric Constant on Particle-Particle Dielectrophoretic Attraction in Dielectric Fluids.* in *The Tenth IEEE International Symposium on Applications of Ferroelectrics.* 1996. East Brunswick, NJ, USA.

40. C.A.Randall, C.A.Bowen, C.P.Shrout, T.R.Newnham, *Smart Processing of Composite Materials by Electric Fields.* Ceramic Transactions, 1995. **54**: p. 185-198.

41. L.Dong, J.Bush, V.Chirayos, R.Solanki, J.Jiao, *Dielectrophoretically Controlled Fabrication of Single-Crystal Nickel Silicide Nanowire Interconnects.* Nano Letters, 2005. **5**(10): p. 2112-2115.

42. L.Dong, J.P.Huang, K.W.Yu, *Theory of Dielectrophoresis in Colloidal Suspensions.* Journal of Applied Physics, 2004. **95**(12): p. 8321-8327.

43. L.Benguigui, I.J.Lin, *The dielectrophoresis force.* American Journal of Physics, 1986. **54**(5): p. 447-451.

44. L.Benguigui, I.J.Lin, *More of the Dielectrophoretic force.* Journal of Applied Physics, 1982. **53**(2): p. 1141-1144.

45. T.H. Kim, S.Y. Lee, N.K. Cho, H.K. Seong, H. J. Choi, S. W. Jung, and S.K. Lee, *Dielectrophoretic Alignment of Gallium Nitride Nanowires (GaN NWs) for Use in Device Applications.* Nanotechnology, 2006. **17**: p. 5.

46. B.G. Hawkins, A. E. Smith, Y. A. Syed, and B. J. Kirby, *Continuous-flow Particle Separation by 3-D Insulative Dielectrophoresis Using Coherently Shaped, DC-Biased, AC Electric Fields.* Analytical Chemistry, 2007. **79**: p. 7291-7299.

47. H.Liu, H.H.Bau, *Dielectrophoresis of Cylindrical and Spherical Particles Submerged in Shells and in Semi-infinite Media.* Physics of Fluids, 2004. **16**(5): p. 1217-1229.

48. P.Tathireddy, Y.H.Choi, M.Skliar, *Particle AC Electrokinetics in Planar Interdigitated Microelectrode Geometry.* Journal of Electrostatics, 2008. **66**: p. 609-619.

49. V.Tomer, C.A. Randall, G.Polizos, J.Kostelnick, E.Manias, *High-and Low-field Dielectric Characteristics of Dielectrophoretically Aligned*

Ceramic/Polymer Nanocomposites. Journal of Applied Physics, 2008. **103**: p. 034115.

50.   K.H.Kang, Y.Kang, X.Xuan, D.Li, *Continuous Separation of Microparticles by Size with Direct Current-Dielectrophoresis.* Electrophoresis, 2006. **27**: p. 694-702.

51.   J.Kadaksham, P.Singh, N. Aubry, *Manipulation of Particles Using Dielectrophoresis.* Mechanics Research Communications, 2006. **33**: p. 108-122.

52.   R.D.Stoy, *Solution Procedure for the Laplace Equation in Bispherical Coordinates for Two Spheres in a Uniform External Field: Parallel Orientation.* Journal of Applied Physics, 1988. **65**(7): p. 2611-2616.

53.   T.K.H.Starke, C.Johnson, S.Hill, P.Dobson, P.S.Grant, *The Effect of Inhomogeneities in Particle Distribution on the Dielectric Properties of Composite Films.* Journal of Physics D: Applied Physics, 2006. **39**: p. 1305-1311.

54.   M.Urdaneta, E.Smela, *Multiple Frequency Dielectrophoresis.* Electrophoresis, 2007. **28**: p. 3145-3155.

55.   N.V. Jayasundere, B. Smith, *Dielectric constant for binary piezoelectric 0-3 composites.* Journal of Applied Physics, 1993. **73**(5): p. 5.

56.   D.Popovich, J.W.Halloran, G.E.Hilmas, G.A.Brady, S.Somers, A.Barda, and G.Zywicki, *Process of Preparing Textured Ceramic Composites*, in *Engineering*, U. Patent, Editor. 1997, 5645781: USA. p. 54.

57.   B.J. Cannon, D. Brei, *Feasibility Study of Microfabrication by Coextrusion (MFCX) Hollow Fibers for Active Composites.* Journal of Intelligent Materials System and Structures, 2000. **11**(September): p. 659-670.

58.   C.V. Hoy, A. Barda, M. Griffith, J.W. Halloran, *Microfabrication of Ceramics by Co-extrusion.* Journal of American Ceramic Society, 1998. **81**(1): p. 7.

59.   G.A. Brady, G.E. Hilmas, J.W. Halloran, *Forming Textured Ceramics by Multiple Coextrusion.* Ceramic Processing Science and Technology, 1995. **51**: p. 297-301.

60.   C.Kaya, E.G.Butler, M.H.Lewis, *Co-extrusion of Al2O3/ZrO2 Bi-phase High Temperatur Ceramics with Fine Scale Aligned Microstructure.* Journal of European Ceramic Society, 2003. **23**: p. 935-942.

61.   G.Hai, H. Young, W. Chang-an, *Preparation and properties of fibrous monolithic ceramics by in-situ synthesizing.* Journal of Materials Science, 1999. **34**: p. 2455-2459.

62.   K.C. Goretta, T.A. Cruse, D. Singh, J.L. Routbort, A.R. de Arellano-Lopez, T.S. Orlova, B.I. Smirnov, *Ceramic fibrous monolithic structures.* Composite Structures, 2004. **66**: p. 7.

63.   S.Baskaran, S.D.Nunn, D.Popovich, J.W. Halloran, *Fibrous Monolithic Ceramics: II, Fabrication, Microstructure, and Indentation Behavior.* Journal of American Ceramic Society, 1995. **76**(9): p. 2209-2216.

64.   Y.H. Koh, H.W.Kim, H.E. Kim, *Fabrication of Macrochannelled-Hydroxyapatite Bioceramic by a Coextrusion Process.* Journal of American Ceramic Society, 2002. **85**(10): p. 2578-2580.

65. P.W.Alexander, D.Brei, J.W.Halloran, *DEPP functionally graded piezoceramics via micro-fabrication by co-extrusion.* Journal of Materials Science, 2007. **42**: p. 5805-5814.

66. Z.N.Wing, *Fabrication and Characterizatioin of Efective Medium Meta-dielectrics*, in *Materials Science and Engineering*. 2005, University of Michigan: Ann Arbor. p. 200.

67. H.Miyazaki, Y.Yoshizawa, K.Hirao, *Preparation and Mechanical Properties of 10 vol% Zirconia/Alumina Composite with Fine-Scale Fibrous Microstructure by Co-extrusion Process.* Materials Letters, 2004. **58**: p. 1410-1414.

68. D.Popovich, J.W. Halloran, G.E. Hilmas, G.A. Brady, S. Somers, A. Barda, and G.Zywicki, *Process of Preparing Textured Ceramic Composites*, in *Engineering*, U. Patent, Editor. 1997, 5645781: USA. p. 54.

69. T.Hanemann, R.Heldele, J.Haubelt, *Structure-property Relationship of Dispersants used in Ceramic Feedstock Development.* Internal discussion.

70. M.A.Perez, *Melt Transformation Coextrusion. II: Flow Analysis.* Polymer Engineering and Science, 1989. **29**(5): p. 1010-1018.

71. R.S.Jones, O.D.J.Thomas, *The coextrusion of two Incompressible Elastico-Viscous Fluids Through a Rectangular Channel.* Journal of Applied Mathematics and Physics, 1989. **40**(May): p. 425-439.

72. S. Baskaran, J.W.Halloran, *Fibrous Monolithic Ceramics: III, Mechanical Properties and Oxidation Behavior of the Silicon Carbide/Boron Nitride System.* Journal of American Ceramics Society, 1994. **77**(5): p. 1249-1255.

73. S.Baskaran, S.D.Bunn, D. Popovich, J.W.Halloran, *Fibrous Monolithic Ceramics: I, Fabrication, Microstructure, and Indentation Behavior.* Journal of American Ceramics Society, 1993. **76**(9): p. 2209-2216.

74. J.Z.Liang, *Effects of Particle Size and Shear Rate on Melt Flow Properties During Capillary Extrusion of Glass Bead-Filled LDPE Composites.* Journal of ASTM, 2006. **3**(8): p. 1-7.

75. R.N.Jana, G.B.Nando, *Rheological Behavior of Low-density Polyethylene (LDPE) - Polydimethylsiloxane Rubber (PDMS) Blends.* Journal of Elastomers and Plastics, 2005. **37**: p. 149-170.

76. J.Zhang, T.P.Lodge, C.W.Macosko, *Interfacial slip reduces polymer-polymer adhesion during coextrusion.* Journal of Rheology, 2006. **50**(1): p. 41-57.

77. J.Dooley, L.Schkopau, *Viscous and Elastic Effects in Polymer Coextrusion.* Journal of Plastic Film and Sheeting, 2003. **19**(2): p. 111-122.

78. M.S.Gildengorn, *Theory and Practice of Co-extrusion of Unequal Strength Materials.* Advanced Performance Materials, 1995. **2**: p. 79-87.

79. L.L.Blyler Jr., A.C.Hart Jr., *Capillary Flow Instability of Ethylene Polymer Melts.* Polymer Engineering and Science, 1970. **10**(4): p. 193-203.

80. A.Lawal, D.M.Kalyon, *Viscous Heating in Nonisothermal Die Flows of Viscoplastic Fluids with Wall Slip.* Chemical Engineering Science, 1997. **52**(8): p. 1323-1337.

81. V.E.Dobrescu, C.Radovici, *Temperature Dependence of Melt Visscosity of Polymers.* Polymer Bulletin, 1983. **10**: p. 134-140.

82. A.M.C.Souza, N.R.Demarquette, *Influence of Coalescence and Interfacial Tension on the Morphology of PP/HDPE compatibilized Blends.* Polymer Engineering and Science, 2002. **43**: p. 3959-3967.

83. A.Abraham, K.E.George, and D.J.Francis, *Flow Behavior of LDPE and Its Blends with LLDPE I and II: A Comparative Study.* Journal of Applied Polymers Science, 1996. **62**(1): p. 59-65.

84. F.B. Timothy, J.L.White, *An Experimental Study of Flow Patterns in Polymer Fluids in the Reservoir of a Capillary Rheometer.* Chemical Engineering Science, 1970. **25**: p. 1191-1195.

85. S.G.Hatziriakos, J.M.Dealy, *Wall Slip of Molten High Density Polyethylenes. II. Capillary Rheometer Studies.* Journal of Rheology, 1992. **46**(4): p. 703-742.

Chapter 8

Feasibility of Composites with Equivalent Permittivity and

Permeability

8.1. Introduction

Composites with equal permittivity and permeability for applications at microwave frequency, in this case 300 MHz, are not achievable by applying dielectrophoresis and coextrusion techniques. It seems that this is not attributed to the deficiencies of methods, but might come from the availability of materials. Therefore, in this chapter, we describe theoretical investigation of the feasibility of this type of materials at different frequencies ranges and textures.

The dielectrophoresis method could tailor material anisotropically and produce flexible materials due to the flexible nature of silicone elastomers. However, it may not be eligible to form a structure in which the permittivity and permeability are equal to each other as described in Chapter 7. The coextrusion technique also did not succeed in producing a core-shell structure with PE shell and Co_2Z-PE core, because the dissimilarity of viscosity of PE and Co_2Z-PE mixture disrupted the coextrusion process. Given the theoretical calculation model expressed below, we calculated the

183

relative permittivity and permeability of different composite geometries like laminate or unidirectional fiber at 300MHz and of those geometries at a frequency of 5 MHz. Co_2Z was considered for different geometrical structures while other dielectromagnetic ceramics, magnesium calcium titanate (CMT) and magnesium alumina ferrite ($Mg(AlFe)_2O_4$), were considered as precursors for the simulations at low frequency ranges.

8.2. Prediction method

In this part, we will describe calculation methods to predict the permittivity and permeability of core-shell structures along parallel and transverse directions corresponding to measuring electric field lines. These predicted values are used to compare with computations of isotropically distributed materials.

For parallel direction:
$$\varepsilon'_{eff} = \varepsilon'_1 \vartheta_1 + \varepsilon'_2 \vartheta_2$$

For transverse direction:
$$\frac{1}{\varepsilon'_{eff}} = \frac{\vartheta_1}{\varepsilon'_1} + \frac{\vartheta_2}{\varepsilon'_2}$$

Where ε'_{eff} is the real permittivity of composite, ε'_1, ε'_2, v_1, and v_2 are real permittivities and volume fractions of inclusions and matrix, correspondingly.

These two equations are firstly applied to calculate the mechanical properties of laminate composites [1]. However, Randall et al. [2] considered that these equations are eligible to predict the permittivity and permeability of aligned composite materials.

The calculations followed two steps in which the first calculation applied the Jayasundere-Smith model for isotropic particulate composites and the second applied the model for anisotropic fiber composite. The effective permittivity and permeability constants obtained from the first calculation served as the initial values to calculate those of core-shell structures. The permittivity and permeability of the core-shell structure can be predicted using the rule of mixture with equations given as following. The predicted data are plotted in fig. 8.2.

5.3. Results and discussions

The first simulation was for laminate composites at frequency 300 MHz. We assumed layers of sintered dense Co_2Z were intercalated by layers of PE as depicted in Fig. 8.1a. This arrangement resulted in two alignment directions, one which was parallel and the other was perpendicular to field lines of measuring electric field. Fig. 8.1b shows the variation of both dielectric permittivity and magnetic permeability along with the Co_2Z volume fraction.

The difference of magnitude of these two parameters narrowed down with the increase of core volume fraction to 40 vol%. From this composition up to 60 vol%, permittivity and permeability were matched with each other. Beyond this value, permittivity is dominant to that of permeability. It means that we can use Co_2Z to produce equivalent permittivity-permeability composite theoretically. However, these theoretical calculations do not necessarily mean that Co_2Z will work in experiments,

since it is a very complicated material as described in Chapter 5. Its properties are only preserved when it is produced in the form of a particulate or laminate. Nevertheless, lamina of Co_2Z ceramics is solid and unflexible, but we were looking for a practical solution for a flexible material. The formation of flexible composite meeting the demand of equivalent permittivity and permeability might be able with the use of Co_2Z fibers. However, the manufacturing of Co_2Z fibers would be a big challenge because of its fragile nature.

The predicted values of permittivity and permeability of samples along the parallel and transverse directions are given in Fig. 8.2. The increase of permeability at parallel direction and the decrease of permittivity at transverse direction would pull them closer together, but not matching at any point in the range up to 100 vol%. The mixing of Co_2Z with LDPE to form core materials would substantially decrease the contribution of its small permeability.

Considering the mixture of high permeability and low permittivity powdered ceramics for the application of the co-extrusion technique, it is expected that the high permeability would compensate the loss of magnetic property so that equal permittivity-permeability will be obtained. In this case, we considered using calcium magnesium titanate (CMT), a material having high and variable permittivity and low permeability ($\mu'=1$) and magnesium ferrite (TT1-414), which has high permeability ($\mu'=80$) at 5 MHz and low permittivity ($\varepsilon'=10$). The magnetodielectric properties of TT1-414 are given in Fig. 8.3. We simulated specimens containing CMT with various permittivity values of 25, 40, 70, and 150 to mix with TT1-414 at different volume

ratios. Amounts of each component stimulated for the calculation are given in Table 8.1 and 8.2. The permittivity and permeability of these mixtures served as initial data for calculations of core-shell structures. Results are depicted in Fig. 8.4, 8.5, 8.6 and 8.7 for samples using CMT-150, Fig. 8.8, 8.9, and 8.10 for samples using CMT- 70, Fig. 8.11 to 8.13 for calculations using CMT-40, and Fig. 8.14 to 8.17 for calculations with CMT-25.

The calculations were conducted for all compositions, but they are not fully shown here because the evolution of both permittivity and permeability split in the way that their low permittivity meets their high permeability at very high ceramic volume fractions, which is close to 100 vol%. While the solid fraction in composites was not able to be higher than 45 Vol% empirically, the discussion of those calculations is not necessary.

The combination of two ceramics with which, one consists of high dielectric permittivity and the other contains high magnetic permeability, certainly overcame the dilution effect on permeability which strongly decreased the contribution of magnetic constant into that of composite. The higher the composition of magnesium ferrite (TT1-414), the higher the magnetic permeability of composite was as being depicted in all graphs. The split of calculated values are bigger in comparison with those textured by dielectrophoresis method to show an ability of improving the experiment setup to obtain higher alignment efficiency. Dielectric and magnetic constants increased their magnitudes along with the increment of solid volume percent together with wider split from the value of isotropic samples. This split

brought permeability of sample at parallel direction closer to its permittivity at perpendicular direction to the alignment direction of inclusions. They met each other and as being seen from graphs, meeting points were below 50 Vol%, compositions which are affordable by mixing method.

Given the combination of a dielectric with a ferrite, equal permittivity-permeability core-shell structures can be achievable through the co-extrusion technique. This is comparable to previous research about the matching impedance at low frequency ranges. Even, at this low frequency range, it is not necessary to apply an advanced technique, but conventional mixing and processing is able to create equivalent permittivity-permeability composites as seen in Fig. 8.3. The application of single ferrite TT1-414 could form a composite with permittivity equal to permeability at 45 ceramic vol%.


8.4. Remarks

Theoretical calculations combining predictions of Jayasundere - Smith model and the mixing rule show the ability of forming this type of material at low frequency range with the use of radio wave magnetodielectric ceramics powders. The application of Co_2Z with silicone elastomers RTV 6166 to form unidirectional equal permittivity-permeability composites is theoretically attainable. Further research is needed to optimize the dielectrophoretic experimental conditions, so that to maximize the alignment efficiency of Co_2Z particles.

Table 8.1: Compositions of core material calculated at designed core's diameter and thickness

Intended vol%	10	20	30	40	45
Used Co_2Z vol%	11.92	24.49	37.06	49.63	55.91
Used LDPE vol%	83.08	70.51	57.94	45.37	39.09
Mineral oil	5	5	5	5	5

Table 8.2: Predicted values of permittivity and permeability of core Co_2Z-LDPE materials

Intended vol%	10	20	30	40	45
Used Co_2Z vol%	11.92	24.49	37.06	49.63	55.91
Used LDPE vol%	83.08	70.51	57.94	45.37	39.09
Predicted permittivity	3.57	4.75	6.27	8.00	8.91
Predicted permeability	1.36	1.95	2.78	3.81	4.38

(a)
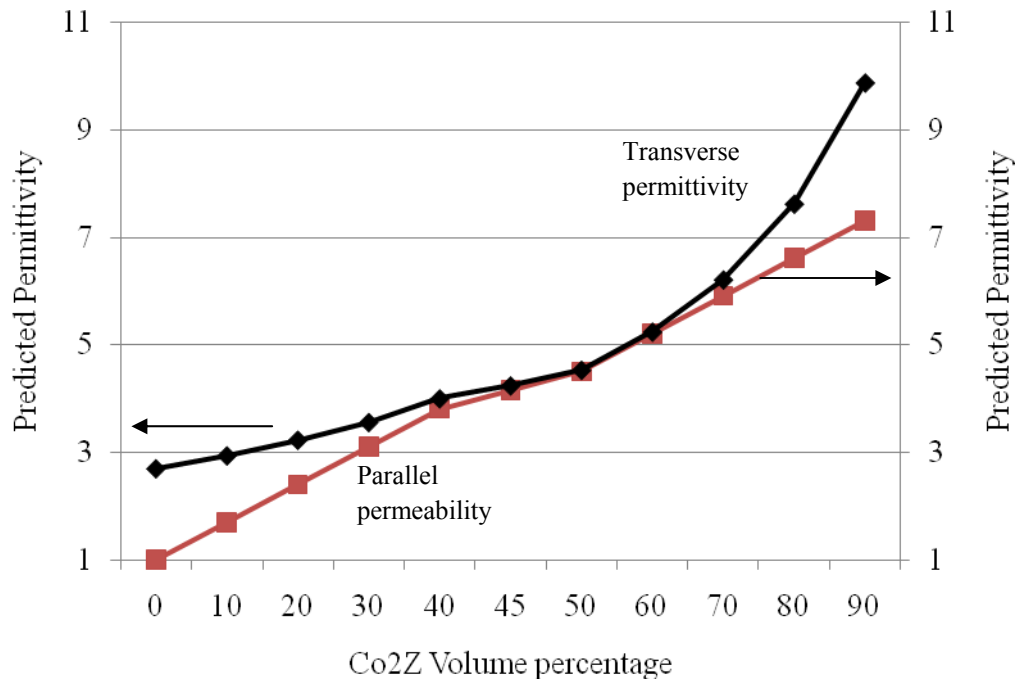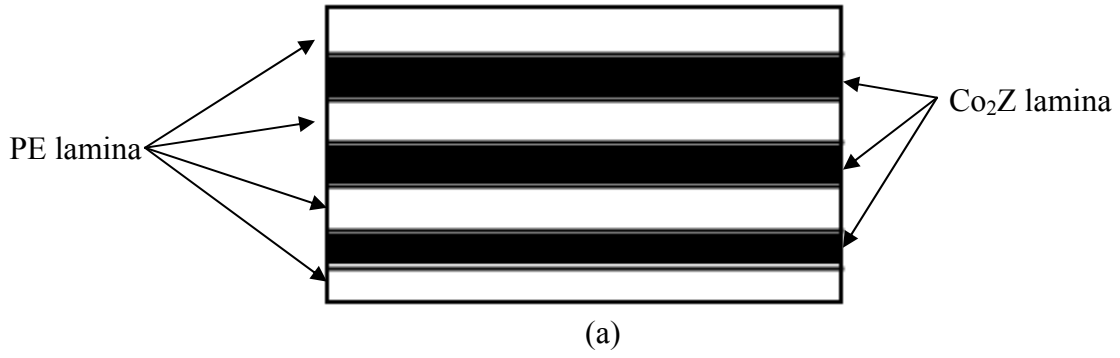
(b)

Fig. 8.1: Schematic of Co2Z-PE laminate composite (a) and its predicted permittivity and permeability values (b) at transverse and parallel directions, correspondingly to the field lines of measuring fields
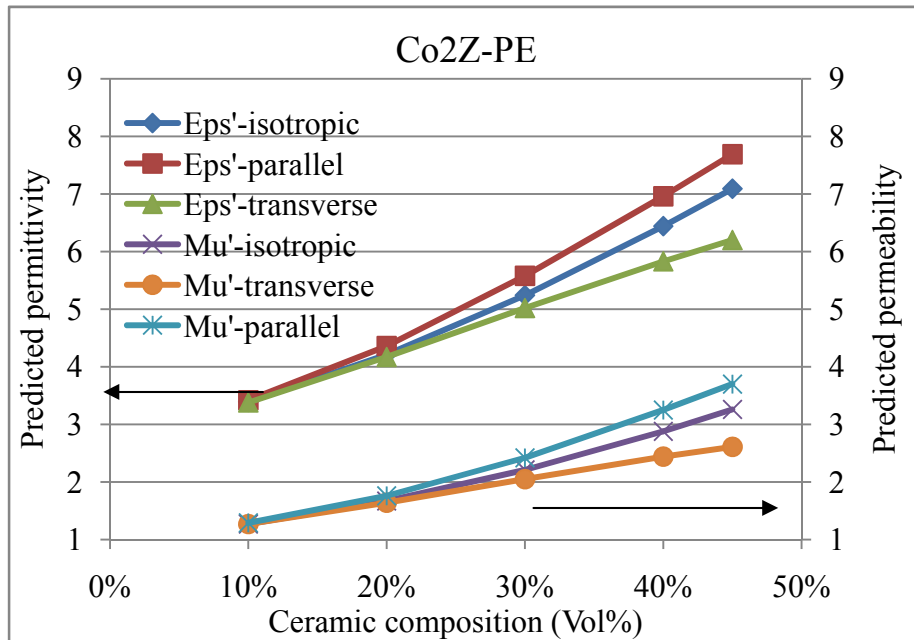
Fig. 8.2: Predicted permittivity and permeability of core-shell structure using 100% Co$_2$Z composite at 5 MHz
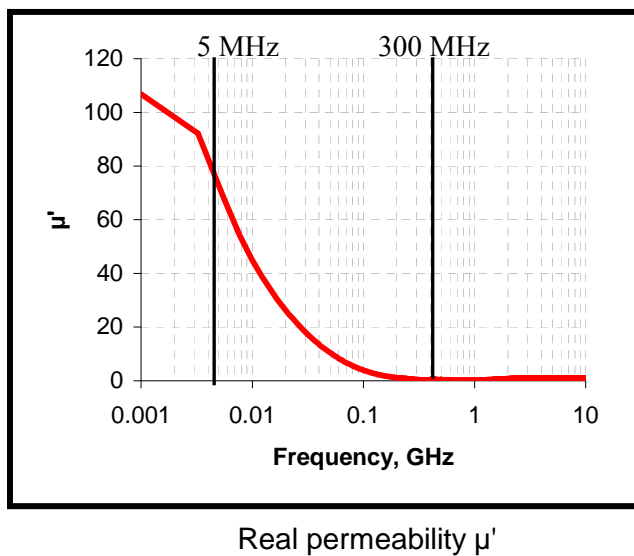

Real permeability μ'

Fig. 8.3: Magnetic permeability of magnesium alumina ferrite (Mg(Al,Fe)$_2$O$_4$) provided by Trans-Tech Inc. This value rapidly decreases along with frequency down to 1 at 200 MHz
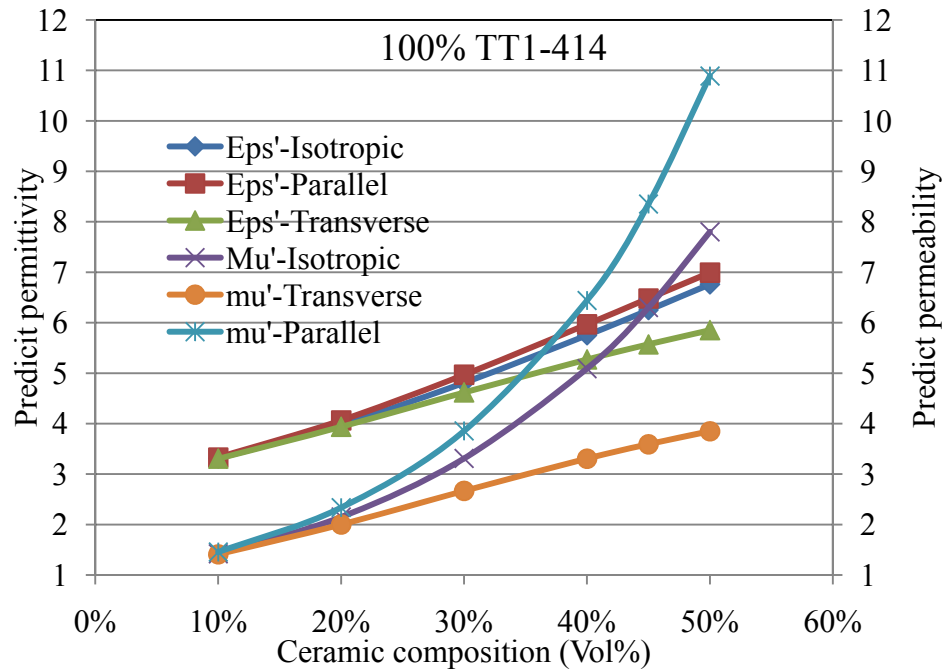
Fig. 8.4: Predicted permittivity and permeability of core-shell structure using 100% magnesium ferrite (TT1-414) composite at 5 MHz
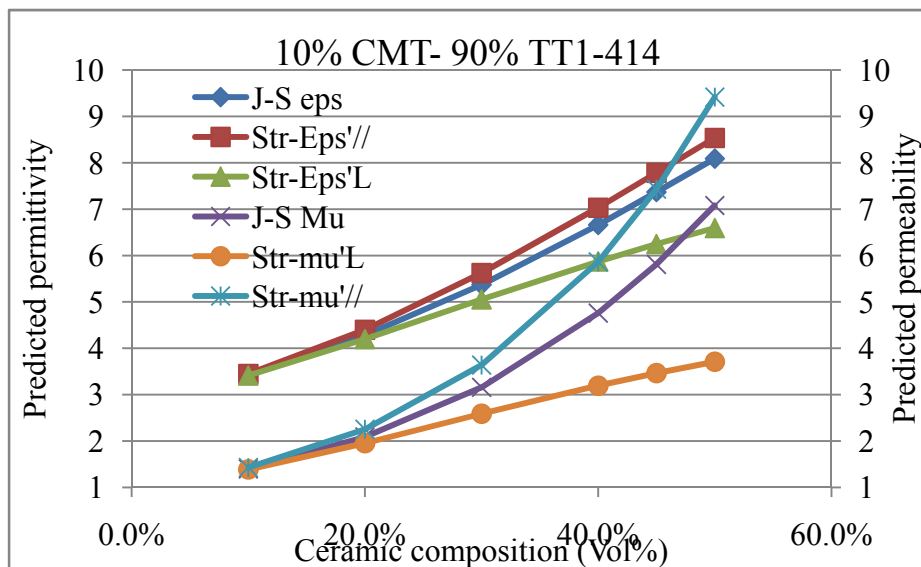

Fig. 8.5: Predicted permittivity and permeability of core-shell structure using mixture of 10 vol% Calcium Magnesium Titanate (CMT-150) and 90 vol% magnesium ferrite (TT1-414) as filler in composite at 5 MHz
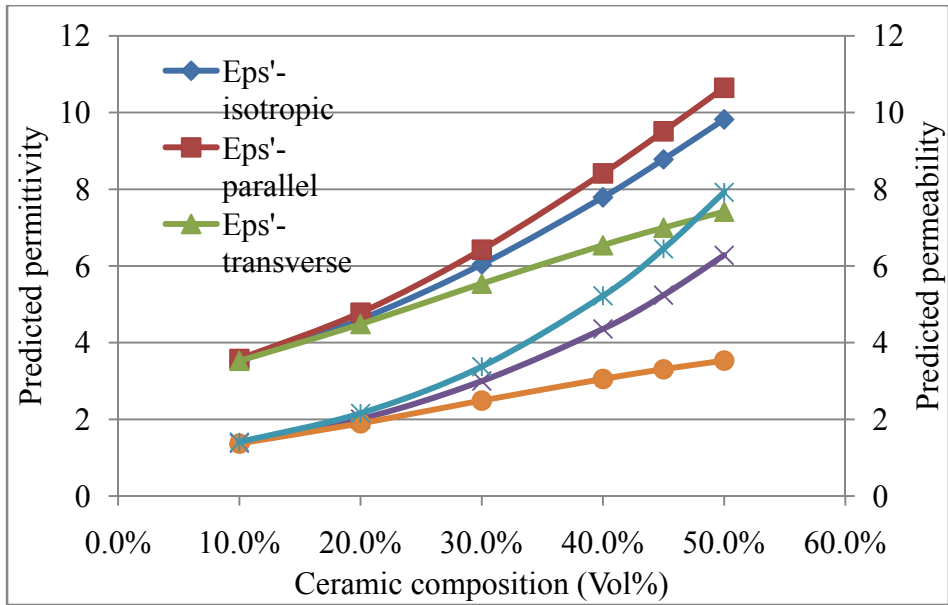
Fig. 8.6: Predicted permittivity and permeability of core-shell structure using mixture of 20 vol% Calcium Magnesium Titanate (CMT-150) and 80 vol% magnesium ferrite (TT1-414) as filler in composite at 5 MHz
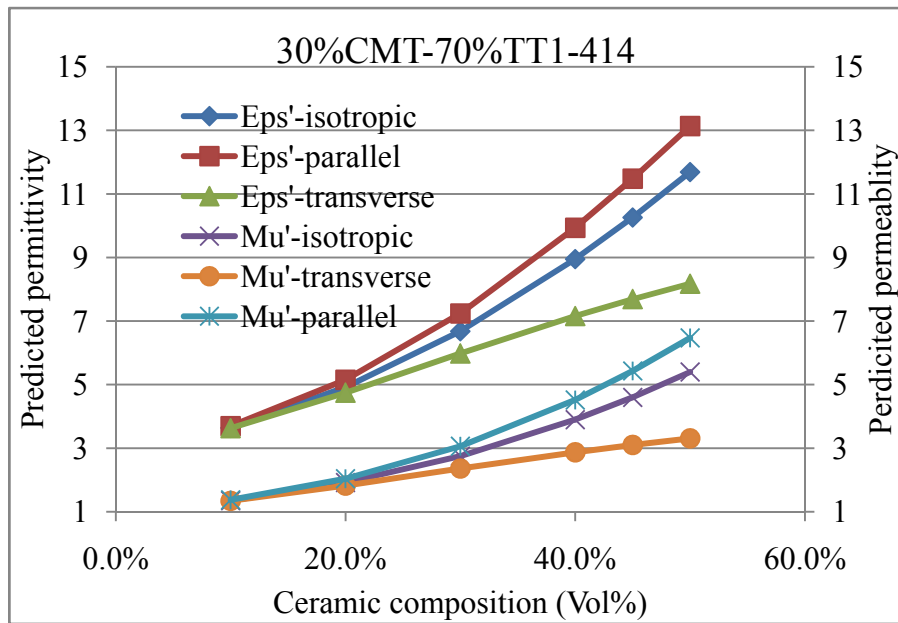

Fig. 8.7: Predicted permittivity and permeability of core-shell structure using mixture of 30 vol% Calcium Magnesium Titanate (CMT-150) and 70 vol% magnesium ferrite (TT1-414) as filler in composite at 5 MHz

Fig. 8.8: Predicted permittivity and permeability of core-shell structure using mixture of 40 vol% Calcium Magnesium Titanate (CMT-150) and 60 vol% magnesium ferrite (TT1-414) as filler in composite at 5 MHz

Fig. 8.9: Predicted permittivity and permeability of core-shell structure using mixture of 10 vol% Calcium Magnesium Titanate (CMT-70) and 90 vol% magnesium ferrite (TT1-414) as filler in composite at 5 MHz
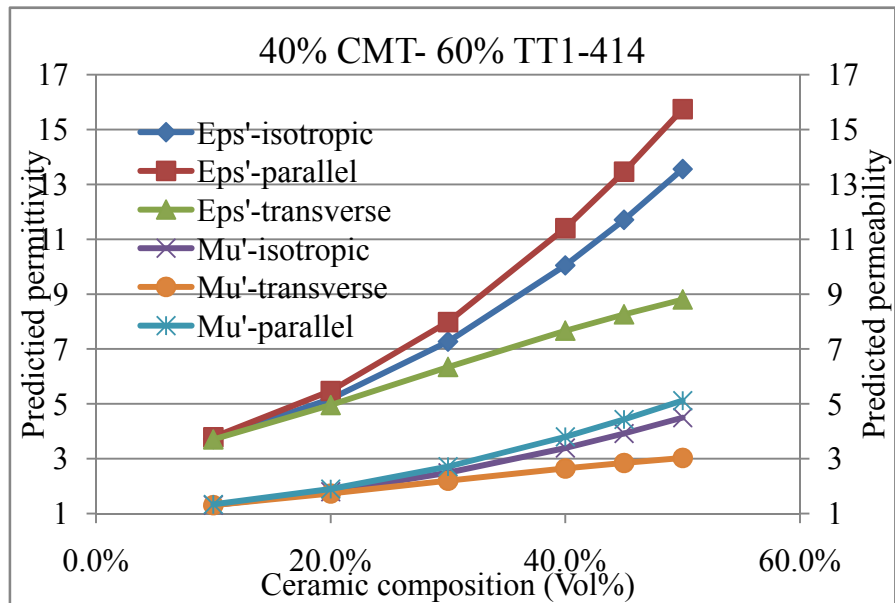
Fig. 8.10: Predicted permittivity and permeability of core-shell structure using mixture of 20 vol% Calcium Magnesium Titanate (CMT-70) and 80 vol% magnesium ferrite (TT1-414) as filler in composite at 5 MHz
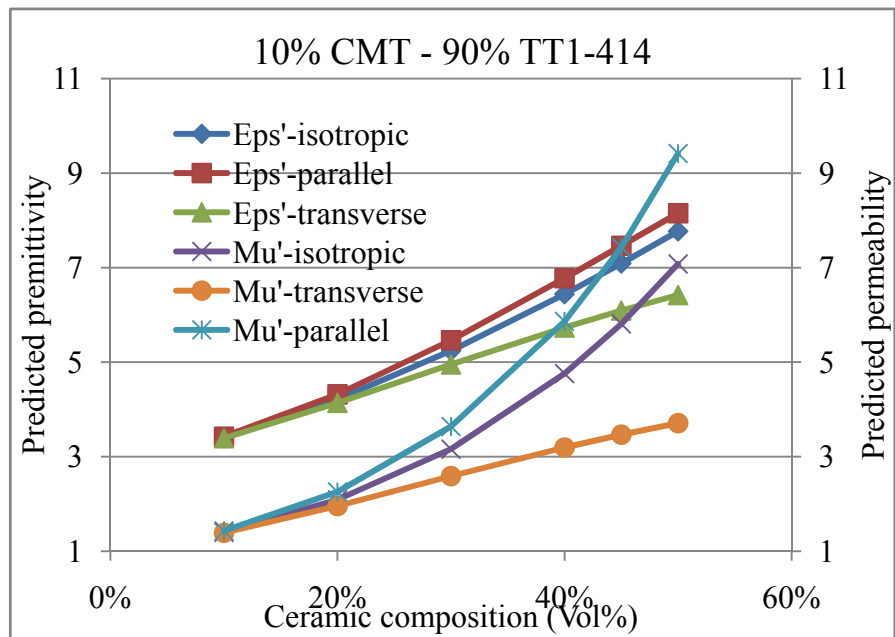

Fig. 8.11: Predicted permittivity and permeability of core-shell structure using mixture of 30 vol% Calcium Magnesium Titanate (CMT-70) and 70 vol% magnesium ferrite (TT1-414) as filler in composite at 5 MHz

Fig. 8.12: Predicted permittivity and permeability of core-shell structure using mixture of 10 vol% Calcium Magnesium Titanate (CMT-40) and 90 vol% magnesium ferrite (TT1-414) as filler in composite at 5 MHz
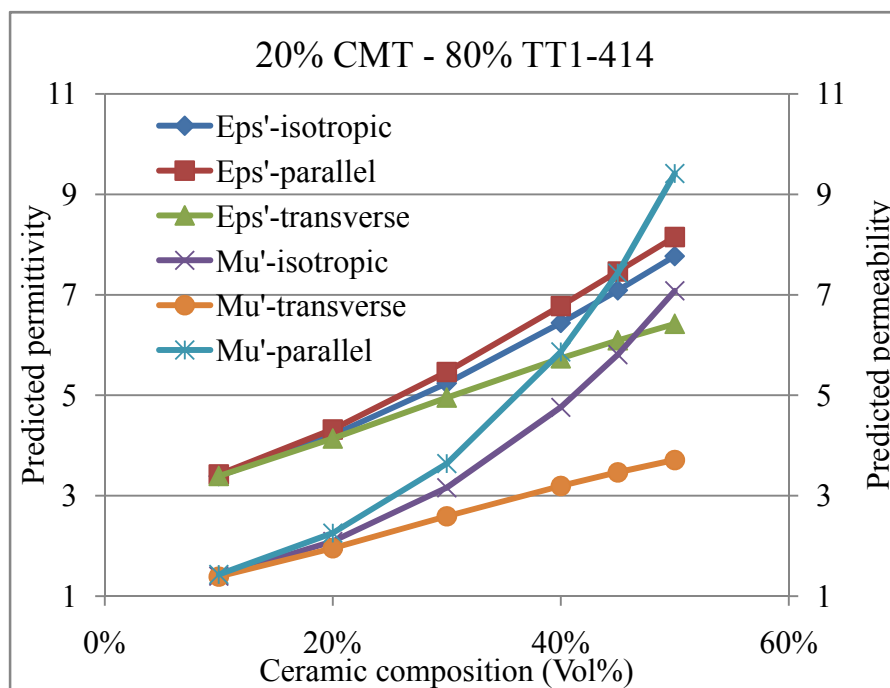

Fig. 8.13: Predicted permittivity and permeability of core-shell structure using mixture of 20 vol% Calcium Magnesium Titanate (CMT-40) and 80 vol% magnesium ferrite (TT1-414) as filler in composite at 5 MHz
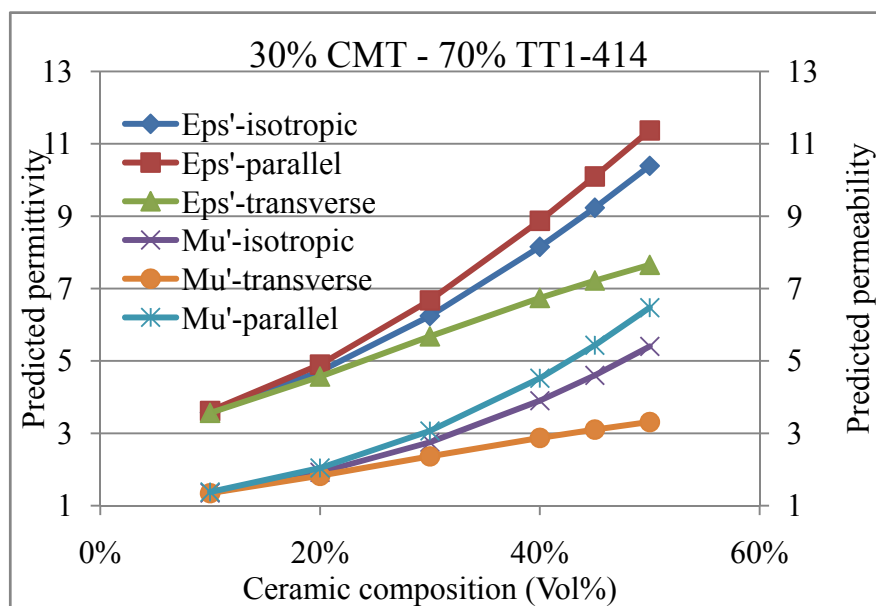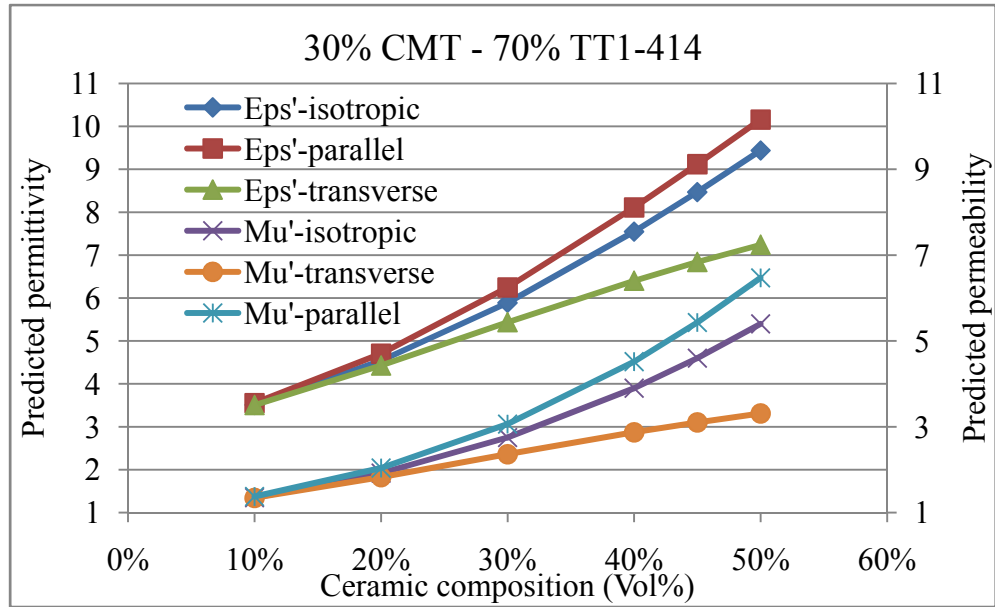
Fig. 8.14: Predicted permittivity and permeability of core-shell structure using mixture of 30 vol% Calcium Magnesium Titanate (CMT-40) and 70 vol% magnesium ferrite (TT1-414) as filler in composite at 5 MHz
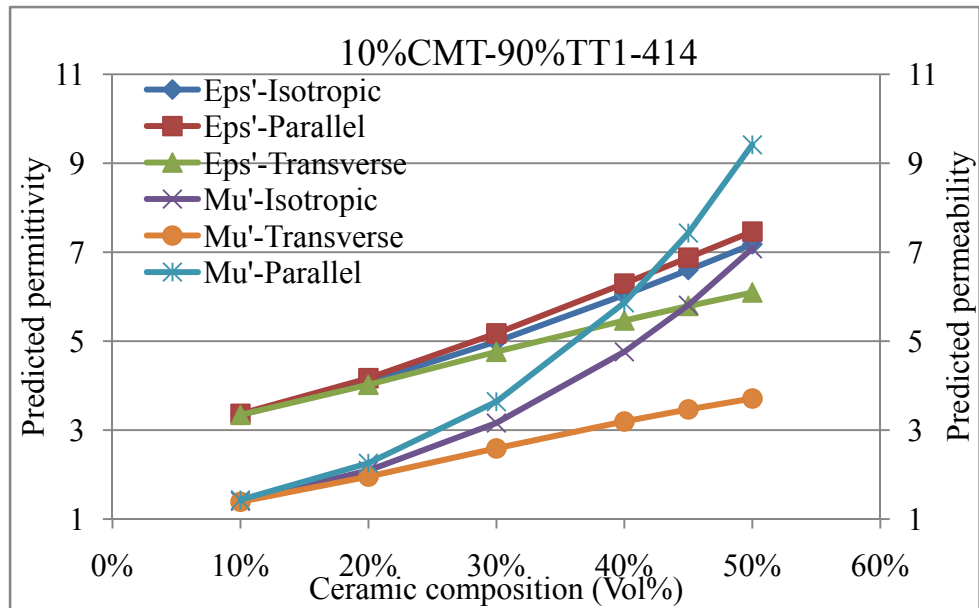
Fig. 8.15: Predicted permittivity and permeability of core-shell structure using mixture of 10 vol% Calcium Magnesium Titanate (CMT-25) and 90 vol% magnesium ferrite (TT1-414) as filler in composite at 5 MHz
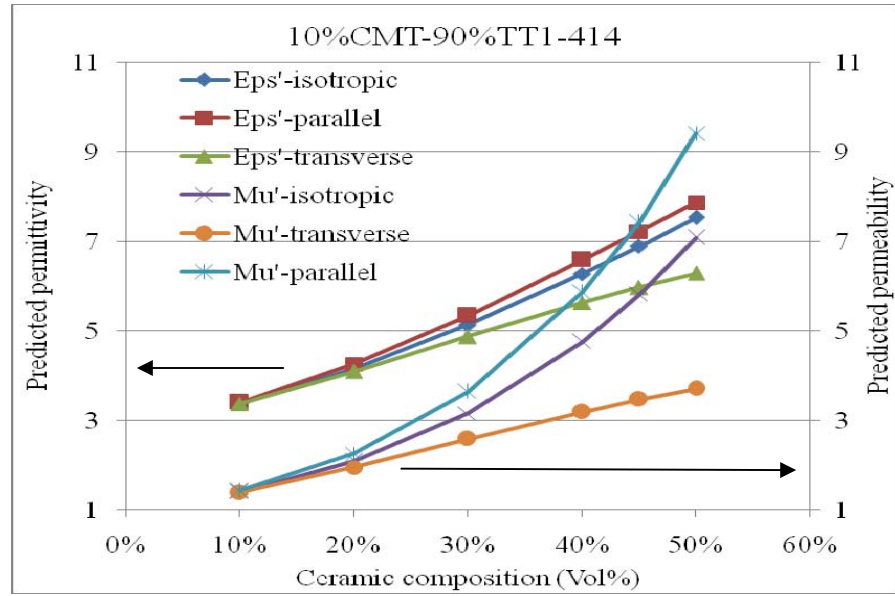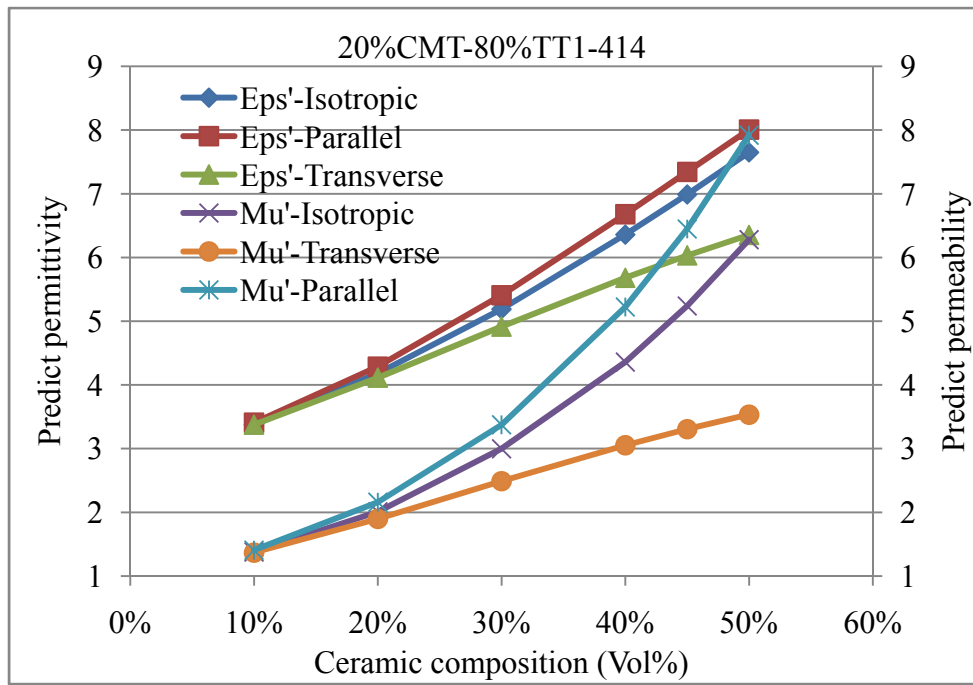
Fig. 8.16: Predicted permittivity and permeability of core-shell structure using mixture of 20 vol% Calcium Magnesium Titanate (CMT-25) and 80 vol% magnesium ferrite (TT1-414) as filler in composite at 5 MHz
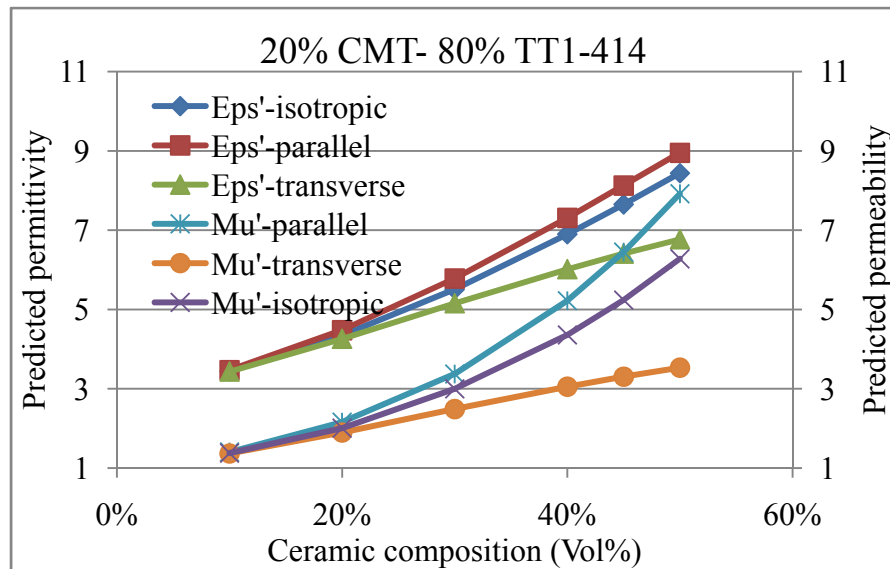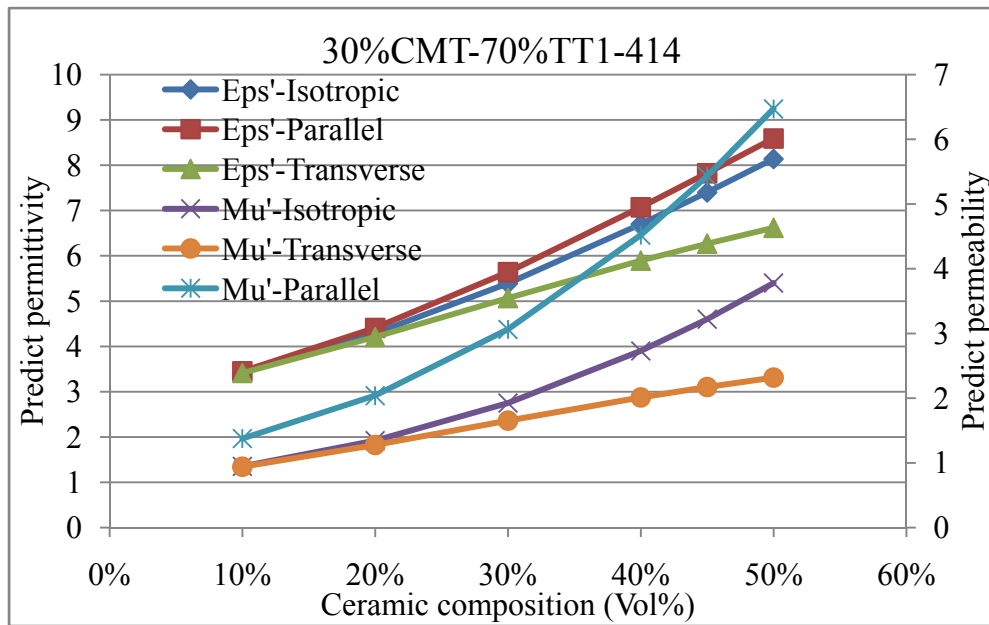

Fig. 8.17: Predicted permittivity and permeability of core-shell structure using mixture of 30 vol% Calcium Magnesium Titanate (CMT-25) and 70 vol% magnesium ferrite (TT1-414) as filler in composite at 5 MHz

References

1.   L.F.Mathews, D.R.Rawlings, ed. *Composite Materials: Engineering and Science*. 2002, Woodhead Publishing Ltd. 251-264.

2.   C.A.Randall, S.Miyazaki, K.L.More, A.S.Bhalla, R.E.Newnham, *Structural-property Relationships in Dielectrophoretically Assembled BaTiO3 Nanocomposites*. Materials Letters, 1992. **15**: p. 26-30

Chapter 9

Conclusions

9.1. Summaries for research topic on Boron Nitride (BN)

Hot pressed BN samples containing 2 and 6 weight percent of Al_2O_3 and Y_2O_3, correspondingly, and 0, 2, and 6 weight percent of amorphous SiO_2 were prepared by the hot mixing, extrusion, and followed by hot pressing at 1740^oC under a pressure of 25 MPa.

The influence of sintering aids Al_2O_3, Y_2O_3 and SiO_2 on the microstructure, mechanical properties and oxidation behavior of BN was investigated. There was a significant growth of BN grain when it was hot pressed with Al_2O_3 and Y_2O_3 with BN platelet diameter increased from 0.5 µm to 14 µm with relatively little increase in grain thickness. This grain growth was suppressed by the addition of amorphous silica. The BN grain growth in this case was only from 0.5 µm to ~2.0 µm, though BN thickness increased relatively higher than that of those samples not using SiO_2.

The dramatic grain growth with Al_2O_3 and Y_2O_3 caused BN platelets not being able to stack in a high order so that they contained high porosity up to 11 %. The addition of

SiO$_2$ reduced the grain growth of BN, which in turn, increased the density so that hot pressed BN samples contained only ~ 1% porosity. The porosity of these samples directly affected to the mechanical properties of sintered BN. The flexural strength of samples containing Al$_2$O$_3$ and Y$_2$O$_3$ was 40 MPa, while those containing 2 and 6 wt% SiO$_2$ increased their strengths to 140 and 155 MPa, correspondingly. Similar behavior was observed with the elastic modulus of BN samples with an increase from 37 GPa to 158 and 166 GPa. Strength and modulus of BN samples were compatible with their density. The improvement with the addition of SiO$_2$ can be attributed to a lower residual porosity.

The oxidation experiments conducted in the conventional tube furnace made oxidized BN samples exposed to moisture in the air so that the hydration reaction of borate occurred, causing a formation of artifact in the oxide microstructure. New oxidation equipment and new experimental procedure were invented to protect oxidized BN samples exposed into the humid air. Microstructure of features formed from the oxidation became reliable and consistent.

Oxidized BN samples containing Al$_2$O$_3$ and Y$_2$O$_3$ consisted of glass droplets. This glassy phase was a movable liquid at high temperature to cover the BN surface. When being quenched, it shrank and separated into droplets as the result of poor wet of B2O3 on BN. The size distribution of these glass droplets increased in a stepwise fashion consistent with the growth and coalescence of water droplets. The time evolution of their maximum droplet size can all be described analogously by the breath figure pattern.

As B$_2$O$_3$ can both react with sintering aid oxides and evaporate, a high Al, Y glassy phase was found present inside the borate glass droplets as spherical substructures. The

formation of these substructures was caused by the liquid-liquid phase separation. For all samples oxidized up to 30 hours, the Al, Y compositions were stable at about 5 at% Al, 7 at% Y, and 30 at% B, which formed an approximate composition $Y_{1.35}AlB_{5.54}O_{11.84}$.

Oxidized BN samples containing Al_2O_3, Y_2O_3, and SiO_2 behaved somehow different with the appearance of a glass layer on BN surface before the appearance of glass droplets. This behavior was believed caused by the dominant reaction of SiO_2 with B_2O_3. The formation of glass droplets also occurred, but hindered from the appearance by the presence of the glass layer. The evolution of the glass droplets in this circumstance was also described by the breath figure pattern. Similar to the case of not using SiO2, spherical substructures were observed inside the glass droplets with the same hypothesis of the liquid-liquid phase separation. These substructures wee also richer in Al and Y, but contained less Si. The atomic ratio of Al to Y was approximately 5 to 7 in all samples at different oxidation times, which is consistent with that observed in oxidized BN samples containing only Al_2O_3 and Y_2O_3. Meanwhile, the glassy matrix in the droplets contained relatively little Al and Y, but rich in Si.

During the oxidation, Al_2O_3 and Y_2O_3 absorbed B_2O_3 in the case not using SiO_2; B_2O_3 and SiO_2 in the case using SiO_2 and released these oxides for the evaporation of B_2O_3. It is assumed that Al_2O_3 and Y_2O_3 are two dominant sintering aid oxides affect the oxidation behavior of BN.

9.2. Summaries for research topic on magnetodielectric composite

Several techniques were applied for the formulation of flexible isotropic Co_2Z-PE, flexible anisotropic Co_2Z-Silicone elastomer, and Co_2Z-PE composites with Co2Z

composition was from 10 vol% to 45 vol%. In all circumstances, permittivity and permeability of sample increased with the increase of Co_2Z volume percentage.

The flexible isotropic Co_2Z-PE composites were formed from hot mixing. Their permittivity varied from 3 to 8, permeability varied from 1 to 5. These experimental data was found better described by the Jayasundere-Smith equation than the Bruggeman's model. The permeability values of all Co_2Z-PE samples containing from 10 vol% to 45 vol% were always equal to about a half of that of their permittivity. The equivalent permittivity and permeability composites were not able to be achieved by using an isotropic Co_2Z-PE material. Nevertheless, the appearance of the magnetic property of Co_2Z was advantageous to improve the performance of antenna. Composite containing 45 vol% Co_2Z used as an antenna substrate improved the antenna's gain at the microwave frequency. It decreased the frequency for the antenna to attain -15 dB gains from 288 MHz of bare spiral metallic antenna down to 230 MHz.

Dielectrophoresis experiments were conducted to produce anisotropic Co_2Z-silicone materials by the alignment of Co_2Z particles along electric field lines. The experiments were pursued at a moderate electric field of 3 kV/cm and two frequencies of 60 Hz and 1000 Hz. The alignment was caused by a nonuniformly induced electric field generated between dielectric particles. The alignment of Co_2Z particles was elucidated by the separation of permittivity and permeability along parallel and perpendicular directions and its efficiency varied with the applied frequency. Alignment at 1 kHz produced non isotropy higher than the alignment at 60 Hz. The ratio of permittivity along parallel direction to perpendicular direction attained the maximum value of 1.26 at 20 vol% Co_2Z composition with the applied frequency 1 kHz. The ratio of permeability along these two

directions also attained the maximum value of 1.46 at 20 vol% Co_2Z composition with the same experimental conditions.

By the application of the dielectrophoresis technique, the permeability of Co_2Z-Silicone composites was brought closer to the magnitude of their permittivity, moving toward the equivalence status of these two properties. However, more improvement is needed. The separation of permittivity and permeability values in the Co_2Z-silisone systems was eliminated due to the low permittivity value of Co_2Z. The small gap between its permittivity to that of the medium resulted in a weak attractive force between particles.

Coextrusion technique was an attempt to form anisotropic Co_2Z-PE composites by a mechanical route. Co_2Z-LDPE mixtures at various Co_2Z compositions were used as the core and HDPE resin was used as the shell to form core-shell structures for the coextrusion. The movement and isolation between core and shell were maintained until it reached to the conical outlet opening. Due to a wide difference of viscosity, strength of the core and the shell materials, the shell was deformed and accumulated at this end and intervened the flow of the whole material structure. The flow of material was not steady so that out-going fibers were distorted to form either wavy or uneven diameter shapes. The miscibility of PEs used resulted in unclear isolation between the core and the shell in the core-shell structure. Theoretical calculations applying Jayasundere – Smith equation revealed that comparable permittivity and permeability cannot be achieved in the Co_2Z-LDPE/HDPE core-shell structure. Meanwhile, it is easily achieved in the $MgFe_2O_4$, CMT (calcium magnesium titanate), and silicone systems at the frequency of 5 MHz.

9.3. Future works for research topic on Boron Nitride (BN)

The influence of sintering aids Al_2O_3, Y_2O_3 and SiO_2 on microstructure of sintered BN was apparent with the grain growth of BN. Evidence of the reaction of these oxides with residual B_2O_3 in BN was depicted on SEM images. However, the composition of these phases had not been studied.

The influence of added oxides on the oxidation behavior of BN could be qualitatively and semi-quantitatively explained. Chemical compositions of the phases formed from the oxidation of BN were analyzed and depicted on phase diagrams. However, as these phases were formed at tiny amounts, their detection was very limited. Furthermore, chemical compositions of the gas phase generated from the BN oxidation were not analyzed.

Therefore, in order to better understand the influence of sintering aids on both microstructure and oxidation of BN, further research should be done on chemical compositions and phases formed during sintering and oxidation of BN.

9.4. Future works for research topic on magnetodielectric composite

It is apparent that the dielectrophoresis technique was the most efficient to formulate uniaxially aligned Co_2Z-silicone elastomer composites to match its permeability with its permittivity. There is still a lot of room for the improvement of this research to find an optimal condition for the Co_2Z particles alignment. The frequency of AC electric field was too low to affect the real and imaginary values of both permittivity and permeability.

However, its impact on the medium and the movement of particles needs more investigation.

The applied AC electric field was at a moderate level, but might be still too weak for dielectrophoresis experiments on the Co_2Z-silicone elastomer system because the dielectric permittivities of Co_2Z and Silicone elastomer are close to each other. Experiments at higher electric fields are required.